全球气候状况报告 (2023)
State of Global Climate (2023)

Co-prepared by
CMA National Climate Centre
CMA National Satellite Meteorological Centre
CMA National Meteorological Information Centre

China Meteorological Administration

Brief Introduction

The National Climate Centre of China Meteorological Administration (CMA), along with the National Satellite Meteorological Centre and the National Meteorological Information Centre, organized their experts to prepare the *State of the Global Climate 2023* report. The report aims to better understand the global climate and reflect China's progress in monitoring global temperature and precipitation, atmospheric circulation systems, SSTs, snow cover, and sea ice. It is composed of five chapters that provide up-to-date monitoring and analysis of the global climate, covering aspects of an overview of global climate, global atmospheric circulations, global oceans, snow cover and sea ice, as well as global major meteorological disasters and significant weather and climate events. Such information provides technological support for governments at all levels to formulate climate-related policies, and serves as a foundational resource for conducting scientific research, technology exchange, and climate education and outreach at both domestic and international levels.

This report is available for decision-makers at all levels, as well as research and teaching personnel in the fields of climate, environment, agriculture, forestry, water resources and energy for their reference. It is also available for readers interested in climate science.

Editorial Committee for *State of the Global Climate 2023*

Advisor　Ding Yihui

Editor-in-Chief　Chao Qingchen

Associate Editors-in-Chief　Jia Xiaolong, Mao Dongyan, Zhou Zijiang, Zhang Peiqun

Executive Editor-in-Chief　Ke Zongjian

Executive Associate Editors-in-Chief　Li Duo, Ding Ting, Han Rongqing, Guo Zengyuan, Liu Yanju, Li Ying, Chen Lin, Cao Lijuan

Editorial Team (in alphabetical order)

Cao Guangzhen, Cao Lijuan, Chen Lifan, Chen Zhiheng, Dai Tanlong, Ding Ting, Guo Zengyuan, Han Rongqing, Li Duo, Liao Jie, Liu Yuan, Lv Zhuozhuo, Sun Yuan, Wang Sujuan, Xu Bin, Xu Wenhui, Yang Mingzhu,Yang Su, Zhai Xiaochun, Zhan Yunjian, Zhang Miao, Zhang Tao, Zhang Wanchun, Zheng Zhaojun

Preface

Climate is a crucial natural resource for human survival and sustainable economic and social development. At present, global warming is accelerating, and key indicators of climate change, such as greenhouse gas concentrations, sea-level rise and glacier melt, are setting new records. These changes have led to increased instability in the climate system, resulting in frequent, widespread, intense, and concurrent extreme weather and climate events globally. Furthermore, the severity and intensity of compound meteorological disasters have increased, posing significant challenges to natural ecosystems, global economic development, and human social stability. Understanding the global weather and climate features in the context of climate change, and pursuing strategies to adapt to, utilize, and protect the climate for a harmonious coexistence between humanity and nature, has become a widely accepted consensus.

In 2023, the global average temperature reached a record high. This was accompanied by frequent extreme weather and climate events such as high temperature, heatwaves, droughts, torrential rains, floods and snowstorms. In line with the spirit of the 20th National Congress of the Communist Party of China and the important instructions from General Secretary Xi Jinping on meteorology, to fully implement the *Guidance on Fostering the High-quality Development of Meteorology (2022-2035)*, efforts have been accelerated to modernize meteorological scientific and technical capabilities as well as to modernize services to society. The goal is to continuously improve China's meteorological support capabilities in terms of "Global Monitoring, Global Forecasting and Global Services." Under this initiative, CMA has undertaken the preparation of the *State of the Global Climate 2023* to keep the public timely informed of the latest global climate conditions and to offer scientific backing for the government in crafting climate-relevant policies.

中国气象局局长

Contents

Abstract

In 2023, land temperatures in most parts of the world were above normal. Specifically, western Asia, Central Asia, parts of East Asia, eastern and western Europe, northern North America, and most of Greenland experienced an increase of more than 1 ℃ above their long-term averages. The global annual mean land temperature was 2.09 ℃ above the 1850-1900 average, marking the highest record since 1850. The global annual mean precipitation was generally below normal, though it varied significantly across different regions; for example, parts of East Asia, eastern and western West Asia, and northeastern Africa received more than 50% above their long-term averages, whereas northwestern Africa and western Australia received more than 50% below average.

In 2023, sea surface temperatures in most of the world's oceans were near or above normal. Notably, temperatures were 2.0 ℃ higher than the long-term average in the central North Pacific and also above average in the equatorial central and eastern Pacific. The La Niña event concluded in January 2023, and by May, El Niño conditions emerged in the equatorial central and eastern Pacific, escalating to meet the criteria for an El Niño event by October. Snow cover in the Northern Hemisphere and Eurasia exceeded long-term averages, while in China, it matched the level recorded in 2022. Both Arctic and Antarctic sea ice extents were below the norm.

In 2023, Greece, southern Bulgaria, parts of Iceland and the North Island of New Zealand experienced heavy rainfall and flooding. At the same time, severe droughts plagued northwestern Africa, parts of the Iberian Peninsula, sections of Central and Southwest Asia, Central America, and northern South America. Record-breaking high temperatures and heatwaves were observed in Southern Europe, North America, East Asia, and South Asia. Europe and North America also faced cold spells and blizzards. Throughout the year, severe convective weather occurred frequently across the world, and there was a high frequency of tropical cyclone activity globally.

Chapter I Overview of Global Climate

In 2023, land temperatures in most parts of the world were higher than in normal years. Western Asia, Central Asia, parts of East Asia, eastern and western Europe, northern North America, and most of Greenland experienced temperatures more than 1 ℃ higher than normal. Conversely, parts of western North America saw temperatures 1-2 ℃ lower than normal. The global annual average land temperature was 2.09 ℃ higher than the average from 1850 to 1900, marking the highest since 1850. Additionally, there was a decrease in global average annual precipitation compared to normal years, with notable variations in spatial distribution. Precipitation increased by over 50% in parts of East Asia, eastern and western West Asia, and northeastern Africa, and decreased by over 50% in northwestern Africa and western Australia.

1.1 Temperature

In 2023, land temperatures in most regions of the world exceeded averages of the normal years (1991-2020). Specifically, eastern West Asia, Central Asia, parts of East Asia, eastern and western Europe, northern North America, and most parts of Greenland experienced temperatures that were over 1 ℃ higher than those in normal years. Central Greenland experienced a temperature increase of over 2 ℃, while certain areas in western North America were 1-2 ℃ below the norm (Figure 1.1).
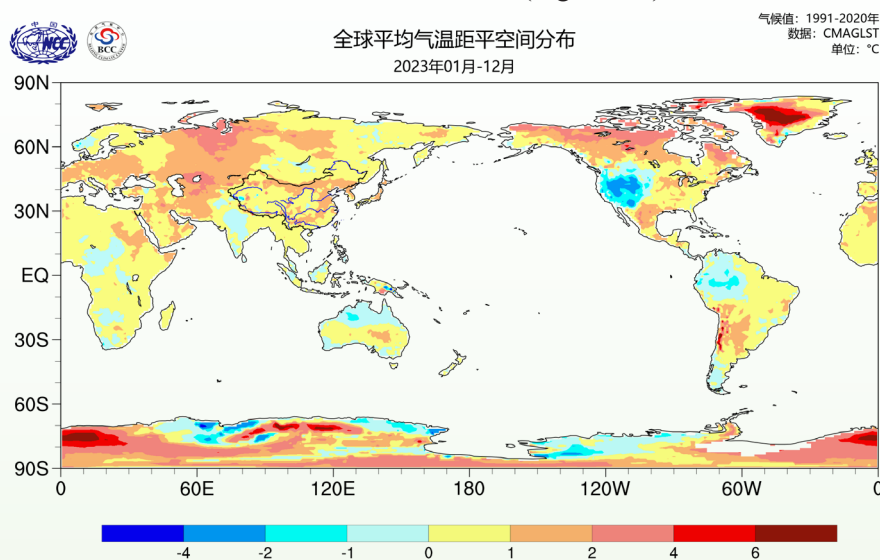

Figure 1.1 Global average temperature anomaly in 2023 (in ℃)

The global annual average land temperature anomaly for 2023 was 2.09 ℃ (averaged from 1850 to 1900), which is the highest since 1850 and 0.42℃ higher than in 2022 (as shown in Figure 1.2).

During the winter of 2023 (December 2022 to February 2023), temperatures in northern and western Europe, eastern North America, most of Greenland, and southern South America were more than 1 ℃ higher than those for winter in normal years. In most of Greenland, the temperature was more than 6 ℃ higher. Conversely, eastern Russia, western North America, northern South America, and northern and eastern Australia experienced temperatures that were more than 1 ℃ lower (Figure 1.3a). The global average temperature anomaly for the winter was 1.68℃, 0.19℃ lower than in 2022 (Figure 1.4a).
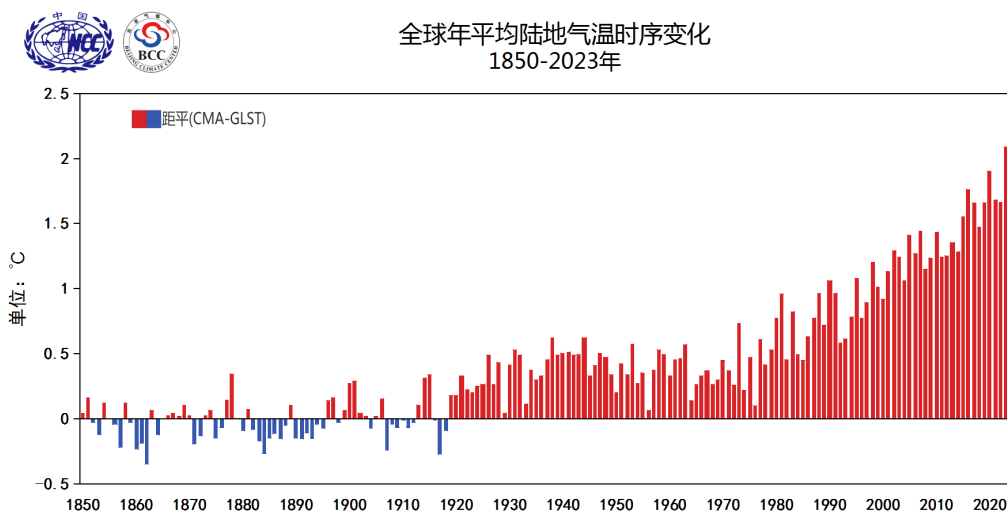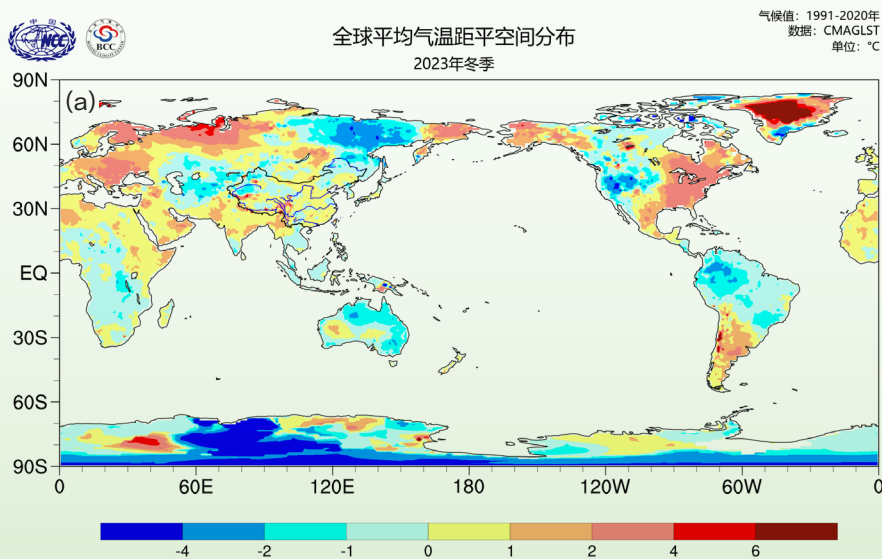
Figure 1.2 Annual fluctuations in global average land temperature anomalies from 1850 to 2023 (in ℃)

During the spring of 2023 (March to May 2023), temperatures in eastern and western Asia, eastern Europe, northern North America, and western Greenland were more than 1 ℃ higher than averages for that season in normal years. Conversely, South Asia, western North America, northern South America, and northern Australia experienced temperatures that were more than 1 ℃ lower (Figure 1.3b). The global average temperature anomaly for the spring was 1.90 ℃, 0.08 ℃ higher than in 2022 (Figure 1.4b).

During the summer of 2023 (June to August 2023), temperatures in northern and western Asia, parts of East Asia, western Europe, northern Africa, southern and northern North America, central South America, and eastern Australia experienced temperatures that were more than 1 ℃ higher than averages for that season in normal years. Conversely, northern Greenland had temperatures that were more than 1℃ lower (Figure 1.3c). The global average temperature anomaly for the summer of the year was 1.89 ℃, which is the highest value recorded since 1850 for the same period and 0.35℃ higher than the temperature recorded in 2022 (Figure 1.4c).

During the autumn of 2023 (September to November 2023), temperatures in most parts of Asia and

全球平均气温距平空间分布
2023年春季

气候值：1991-2020年
数据：CMAGLST
单位：℃

全球平均气温距平空间分布
2023年夏季

气候值：1991-2020年
数据：CMAGLST
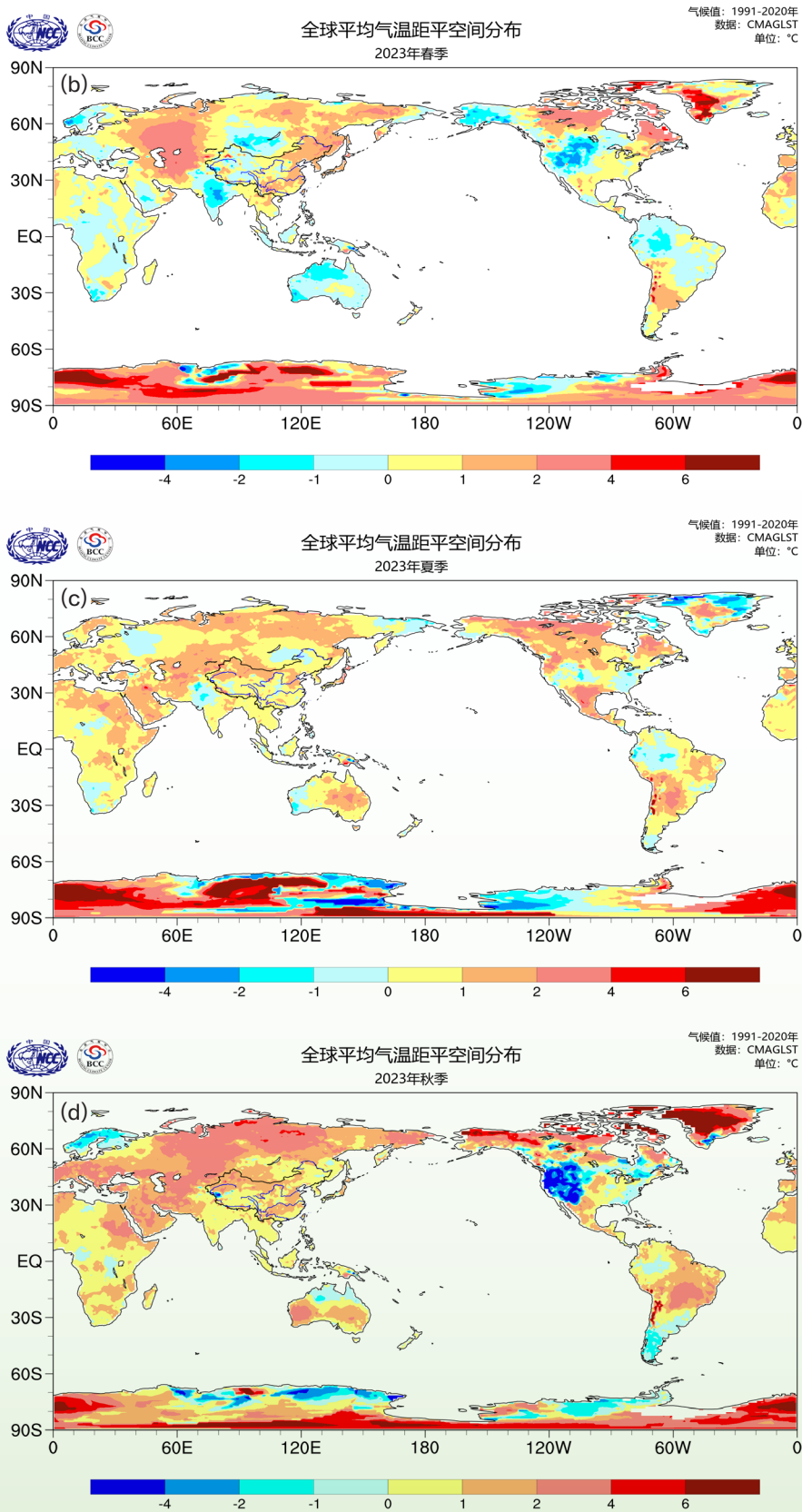单位：℃

全球平均气温距平空间分布
2023年秋季

气候值：1991-2020年
数据：CMAGLST
单位：℃

Figure 1.3 Global seasonal average temperature anomalies in 2023
(a) winter; (b) spring; (c) summer; (d) autumn (in ℃)

Europe, northern and southern Africa, most of Greenland, northern North America, central South America, and southern Australia were more than 1 ℃ higher than averages for that season in normal years. Central Greenland experienced a temperature increase of more than 6 ℃. Conversely, northern Europe and western North America experienced a temperature decrease of more than 1 ℃ (Figure 1.3d). The global average temperature anomaly for the autumn of the year was 2.54 ℃, which is the highest value recorded since 1850 for the same period and 0.89 ℃ higher than the temperature recorded in 2022 (Figure 1.4d).

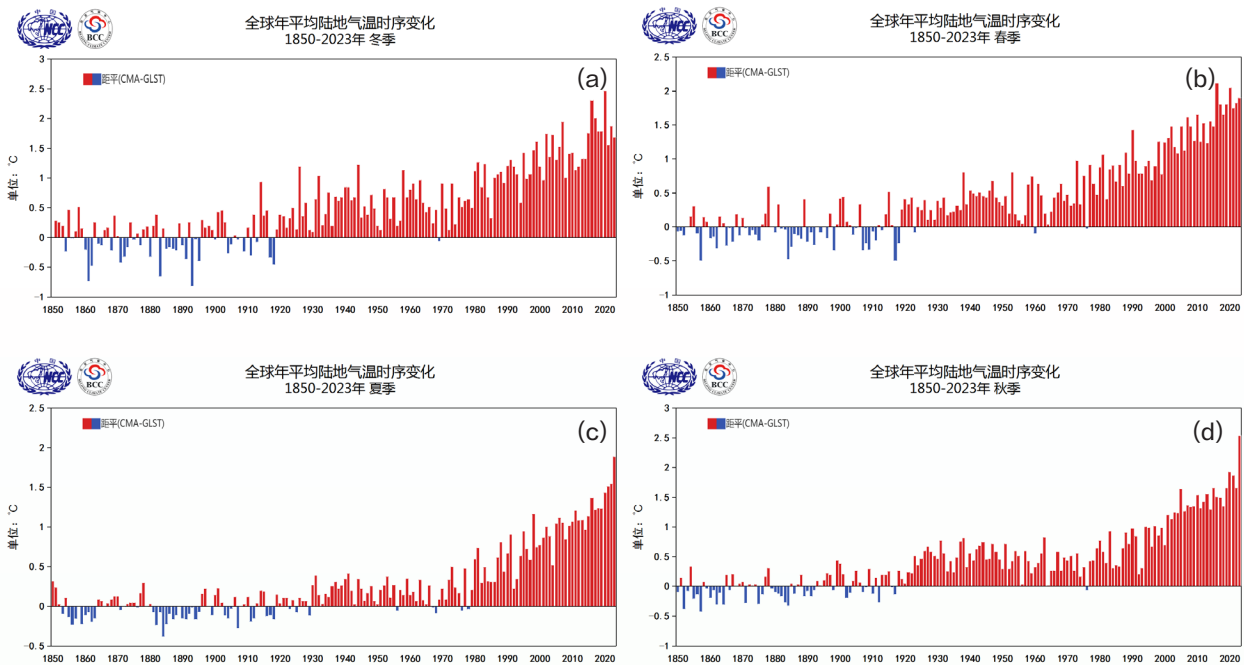Figure 1.4 Annual fluctuations in global seasonal average land temperature anomalies from 1850 to 2023 (a) winter; (b) spring; (c) summer; (d) autumn (in ℃)

The global monthly average temperatures in 2023 were higher than those for the same period in normal years. The temperature anomaly in November was 1.37 ℃ (Figure 1.5).
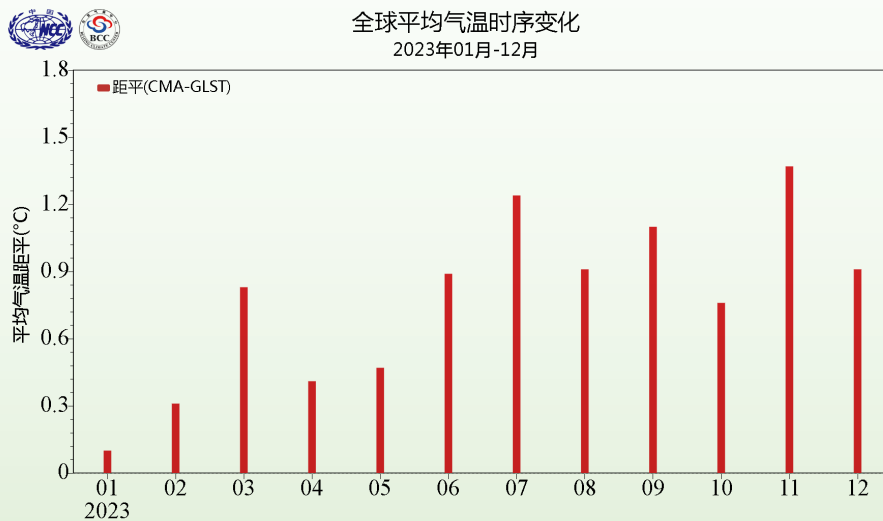
Figure 1.5 Global monthly average temperature anomalies for 2023 (in ℃)

1.2 Precipitation

In 2023, parts of East Asia, eastern and western West Asia, and northeastern Africa received over 50% more precipitation than in typical years, while northwestern Africa and western Australia experienced a decrease in precipitation of more than 50% (Figure 1.6).

Figure 1.6　Distribution of the global precipitation anomaly percentage in 2023 (in %)

In 2023, the global annual average land precipitation is lower than that in normal years, marking the lowest for the same period since 1979 (Figure 1.7).

Figure 1.7　Annual variations in global average land precipitation from 1979 to 2023 (bar chart) and the climatological average (black line) (in mm)

During the winter of 2023, precipitation in central Asia, West Asia, central Europe, central Africa, and central North America experienced an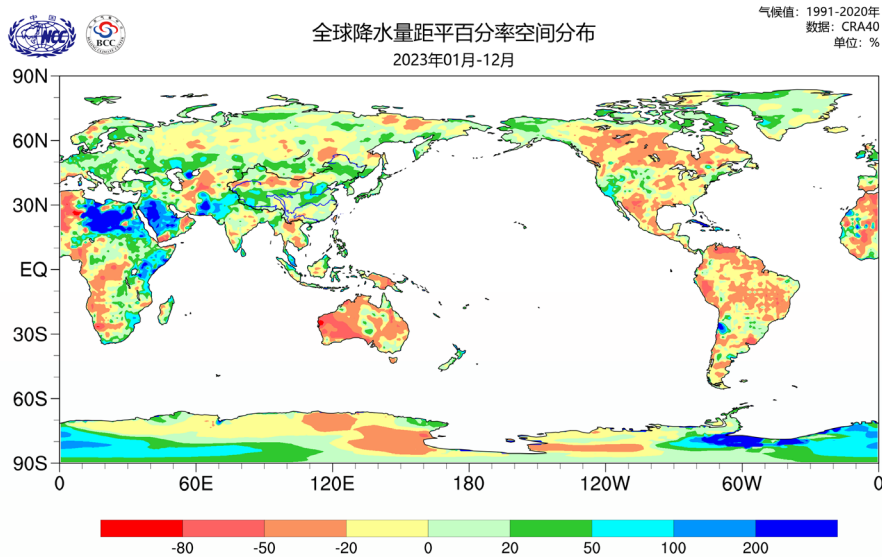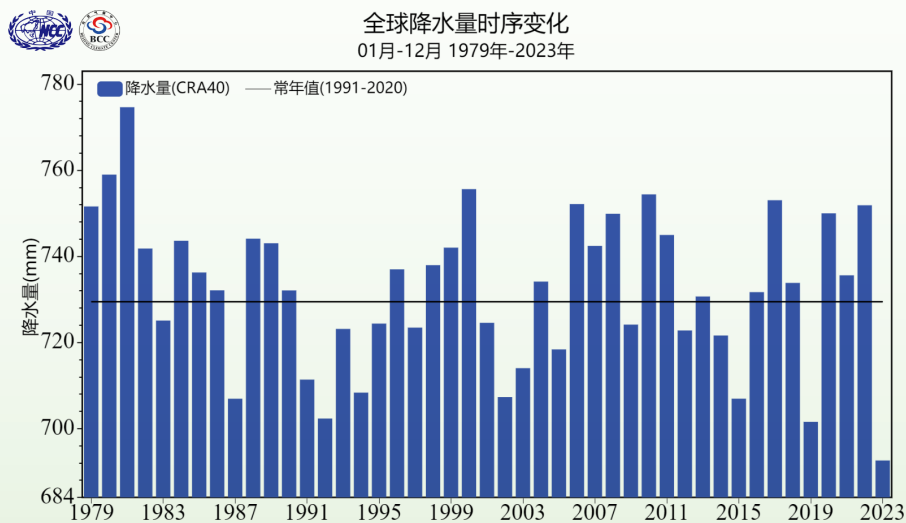 increase of over 50% than that for the winter in normal years. Western West Asia and central Africa had over twice as much. In contrast, South Asia, northern Africa, and western Australia had a decrease of more than 50% (Figure 1.8a). The global average precipitation during the winter was 162.85 mm, which is 4.7% lower than that of normal years and 11.19 mm less than the 2022 level (Figure 1.9a).

During the spring of 2023, precipitation in most parts of East Asia, South Asia, western West Asia, and eastern Africa exceeded that of normal years by over 50%. Western South Asia, western West Asia, and northeastern Africa experienced more than twice the average precipitation. Conversely, Central Asia, northwestern and southern Africa, and central and western Australia received over 50% less than the average amounts (Figure 1.8b). The global average precipitation for the spring was 175.3 mm, which is 3.69% less than the average for spring in normal years and 12.96 mm less than the 2022 level (Figure 1.9b).

In the summer of 2023, precipitation in central East Asia, northern Africa, Greenland, and northern Australia was over 50% more than that for summer in normal years. Northern Africa and northern Australia had over twice as much. Meanwhile, eastern West Asia, southern Africa, southern North America, central South America, and eastern and western Australia had more than 50% less (Figure 1.8c). The global average precipitation for the summer was 188.68 mm, which is 6.68% less than the average for summer in normal years, the lowest since 1979, and 17.66 mm less than the 2022 level (Figure 1.9c).

In the autumn of 2023, precipitation in most parts of East Asia, northern South Asia, western West Asia, most parts of Europe, and eastern Africa was over 50% more than that for autumn in normal years. Western West Asia and eastern Africa had more than twice as much. Meanwhile, western Africa, central and northern South America, and western and northern Australia had more than 50% less (Figure 1.8d). The global average precipitation for the autumn was 166.98 mm, 4.19% less than the average for autumn in normal years and 19.14 mm less than the 2022 level (Figure 1.9d).
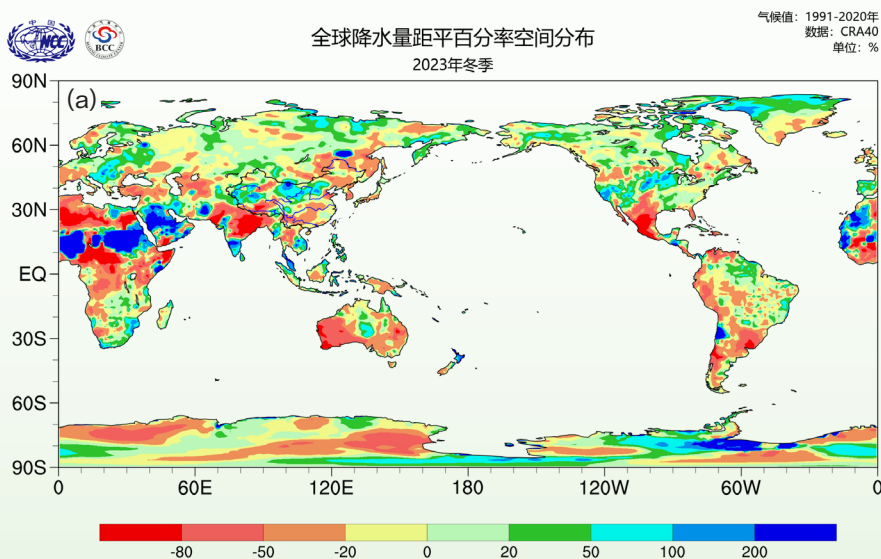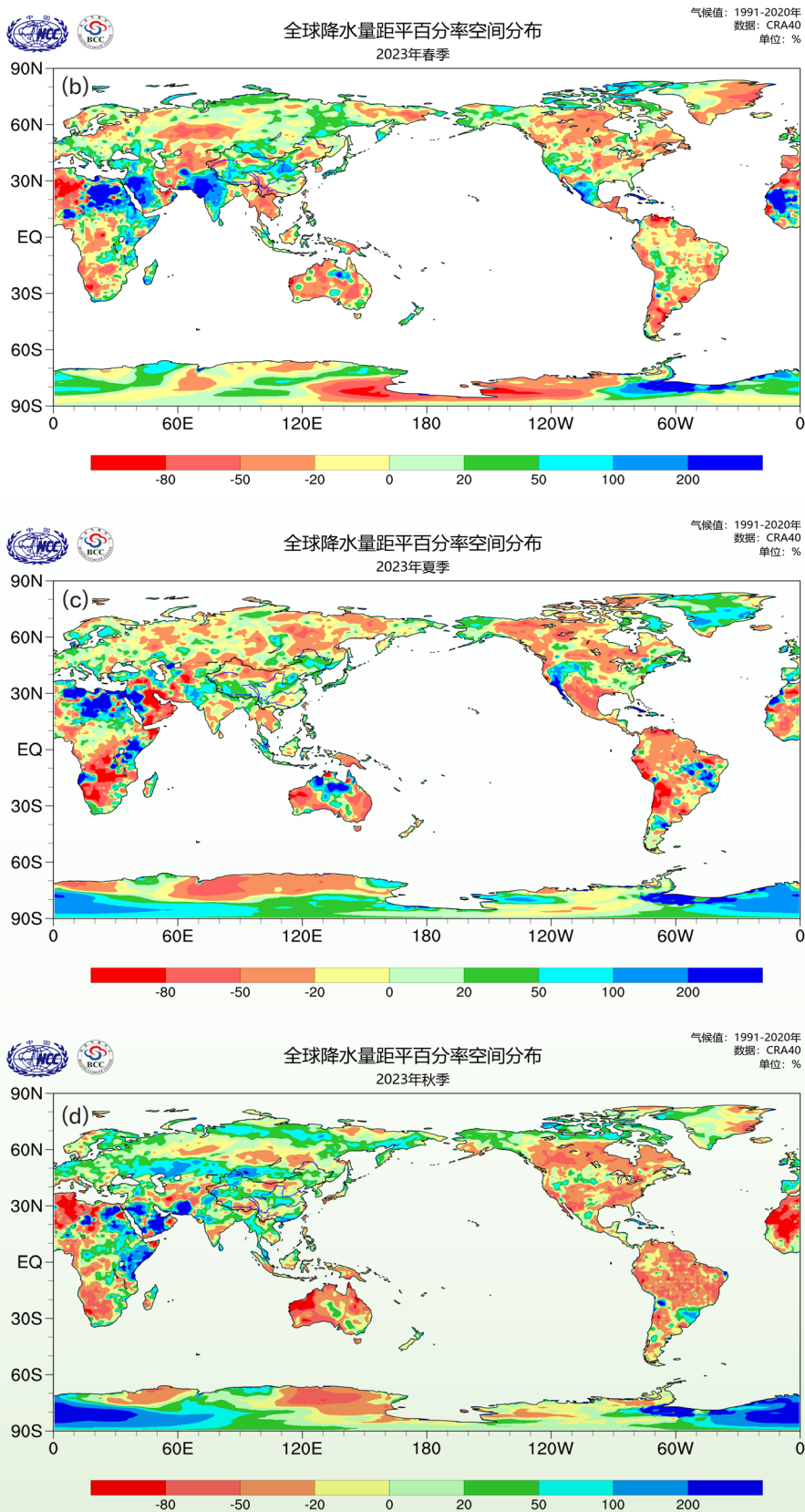
Figure 1.8 Distribution of global seasonal precipitation anomaly percentage in 2023
(a) winter; (b) spring; (c) summer; (d) autumn (in %)
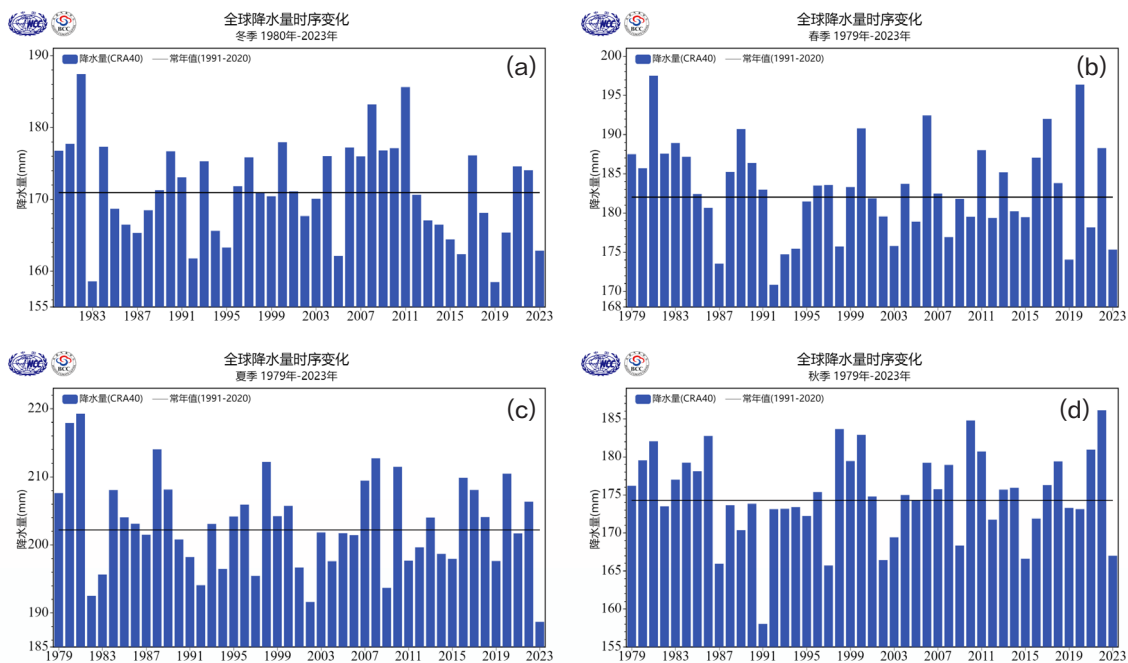
Figure 1.9 Annual variations in global seasonal average land precipitation levels from 1979 to 2023 (bar chart) and the climatological average (black line) (in mm)
(a) winter; (b) spring; (c) summer; (d) autumn

In 2023, the global average precipitation levels for January, March, and November were higher than those for the same period in normal years. Specifically, November saw a 3.38% increase. Conversely, there was a decrease during February, April to October, and December, with February seeing a 10.97% decrease (Figure 1.10).
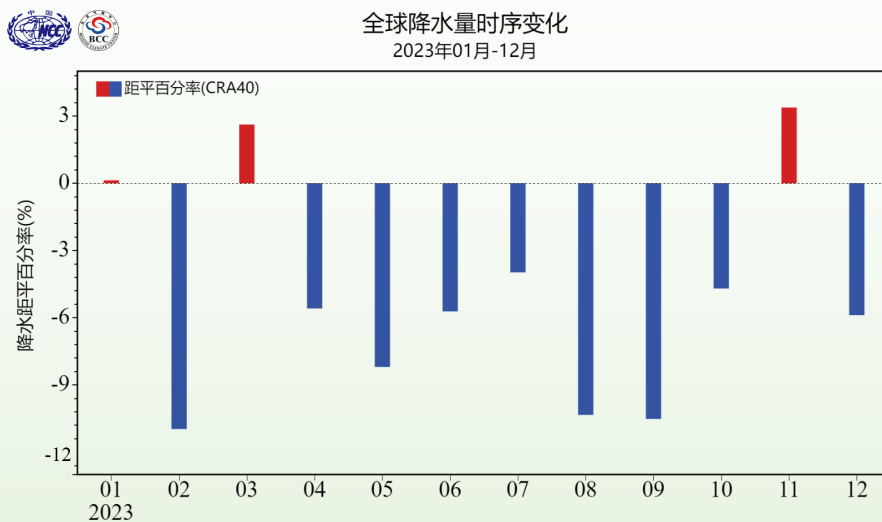
Figure 1.10 Monthly global average precipitation anomaly percentage in 2023 (in %)

Chapter II Global Atmospheric Circulations

In 2023, during the winter, the Northern Hemisphere's Arctic Oscillation exhibited a negative phase, with two strong low-vortex cyclonic centers located outside the Arctic in the Far East of East Asia and the northwest of North America. The global major monsoon regions, including the South Asian, East Asian, and North American monsoons, displayed characteristics of being stronger in winter and weaker in summer. During the summer, the subtropical high-pressure belt in the Northern Hemisphere was stronger. The South Asian high was larger and more intense, while the Ural blocking high was weaker. Additionally, the Okhotsk blocking high was stronger, and the North Atlantic Oscillation was in a negative phase. In 2023, a seesaw phenomenon was observed in the sea-level atmospheric pressure in the tropical Pacific, as it shifted from "high in the east and low in the west" to "low in the east and high in the west."

2.1 Global Atmospheric Circulation Systems

During the winter of 2023, the polar vortex in the Northern Hemisphere was in a negative phase, as evidenced by the 200 hPa geopotential height field and anomaly field. The Arctic experienced a higher-than-normal height field, while the Far East of East Asia and the northwest of North America saw low-pressure cyclones. From the North Pacific to East Asia, the majority of the region was under the control of positive anomalies in the height field. Meanwhile, the atmospheric circulation over the low latitudes of the Pacific exhibited low pressure in the east and high pressure in the west. From the North Atlantic to eastern North America, the region experienced high pressure in the north and low pressure in the south, with most of Europe experiencing higher-than-normal height fields. In the Southern Hemisphere, the polar vortex was in a positive phase. There was a lower-than-normal height field over Antarctica and higher-than-normal over most mid-latitude regions. The region from the South Indian Ocean to most of Africa at low-latitude also had a lower-than-normal height field. In the spring, the Arctic region experienced a lower-than-normal height field, and atmospheric long waves were found at the mid-latitudes of the Northern Hemisphere, with high-pressure ridges and low-pressure troughs alternatively arranged. The North Pacific Oscillation and the North Atlantic Oscillation were both significant, with the low-latitude height field being higher than normal globally, and the positive anomaly centre leaning towards the southern side of the equator. In the Southern Hemisphere, most of the Antarctic region had positive height field anomalies. Two negative anomaly centres were located beyond Antarctica, on the southern side of Australia at mid-latitude and the southeastern part of the South Pacific at high latitude. During the summer, the height field was consistently higher than normal, spanning from most of the Northern Hemisphere to the low latitudes of the Southern Hemisphere. The Southern Hemisphere polar vortex was in a positive phase, causing the Antarctic vortex to extend northward to the mid-latitudes in the eastern and western parts of the South Pacific, forming two negative anomaly centres. In the autumn, the global circulation pattern was similar to that of the summer, except that in the Northern Hemisphere, Europe and the East Siberian Sea had lower-than-normal height fields, each having a negative anomaly centre in the anomaly field. The polar vortex centre in the Southern Hemisphere was located near the Ross Sea (Figure 2.1).
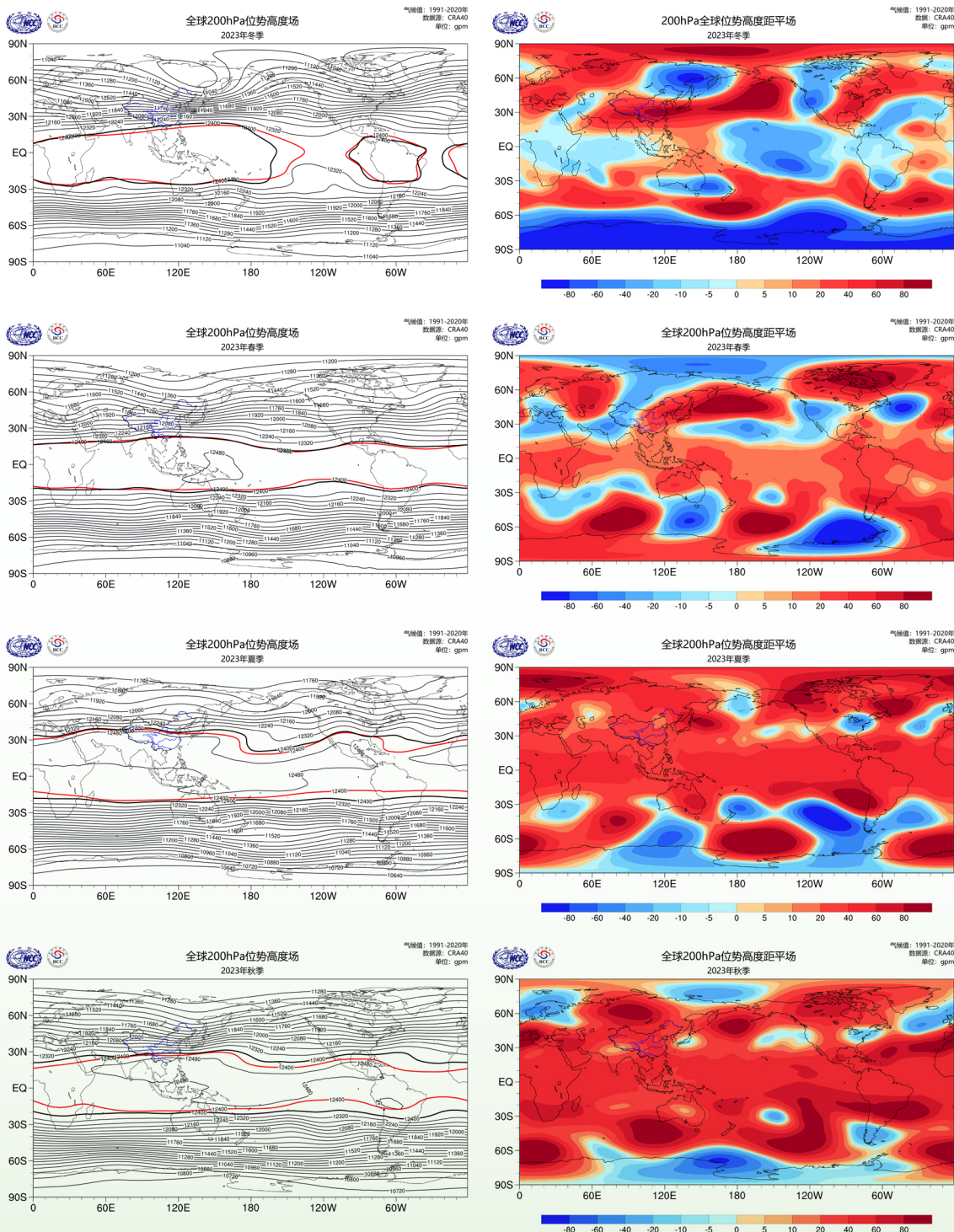
Figure 2.1 Global seasonal average 200 hPa geopotential height fields (left) and anomaly fields (right) in the winter, spring, summer, and autumn of 2023 (from top to bottom) (red isopleths on left-side images represent the climatological state)

The 500 hPa geopotential height field and anomaly field for the winter reveal that the circulation pattern is similar to that at 200 hPa. The Western Pacific Subtropical High was weaker in intensity and smaller in area, with its ridge line located further north compared to the long-term average for winter. In the spring, the circulation characteristics at mid-to-high latitudes in both hemispheres were similar to those at 200 hPa. Prominent atmospheric waves were observed at mid-to-high latitudes in the Northern Hemisphere. The North Pacific Oscillation and North Atlantic Oscillation both exhibited negative-phase characteristics, and the tropical Pacific height field is higher than that observed during spring in normal years. During the summer, the height field over most of the Northern Hemisphere was higher, with the meridional East Asia-Pacific teleconnection pattern showing a positive phase. The Western Pacific Subtropical High was stronger in intensity and larger in area, with its westward ridge point situated noticeably further west and ridge line close to that in the same period in normal years. In the autumn, the circulation distribution at mid-to-high latitudes over Eurasia exhibited low pressure in the west and high pressure in the east. The Western Pacific Subtropical High was stronger in intensity, with its westward ridge point located further to the west, and its ridge line positioned slightly more to the south (Figure 2.2).

The winter sea level pressure (SLP) and anomaly fields reveal that the SLP across a large portion of Siberia was higher than the long-term averages for this season. Additionally, the Aleutian Low exhibited stronger intensity and a more westerly position compared to the norm. The strength of the equatorial convergence zone was marginally higher. In the spring, the Arctic region experienced below-average SLP and the Aleutian Low exhibited signs of weakening. Meanwhile, as the La Niña event declined, the SLP in both the eastern and western tropical Pacific returned to normal levels. During the summer, the equatorial convergence zone was positioned near the norm, though its intensity was slightly higher. In the autumn, due to the development of the El Niño event, the strength of the equatorial convergence zone is somewhat reduced compared to the long-term average for this season. This led to a spatial SLP distribution in the tropical Pacific characterized by higher pressure in the west and lower pressure in the east (Figure 2.3).
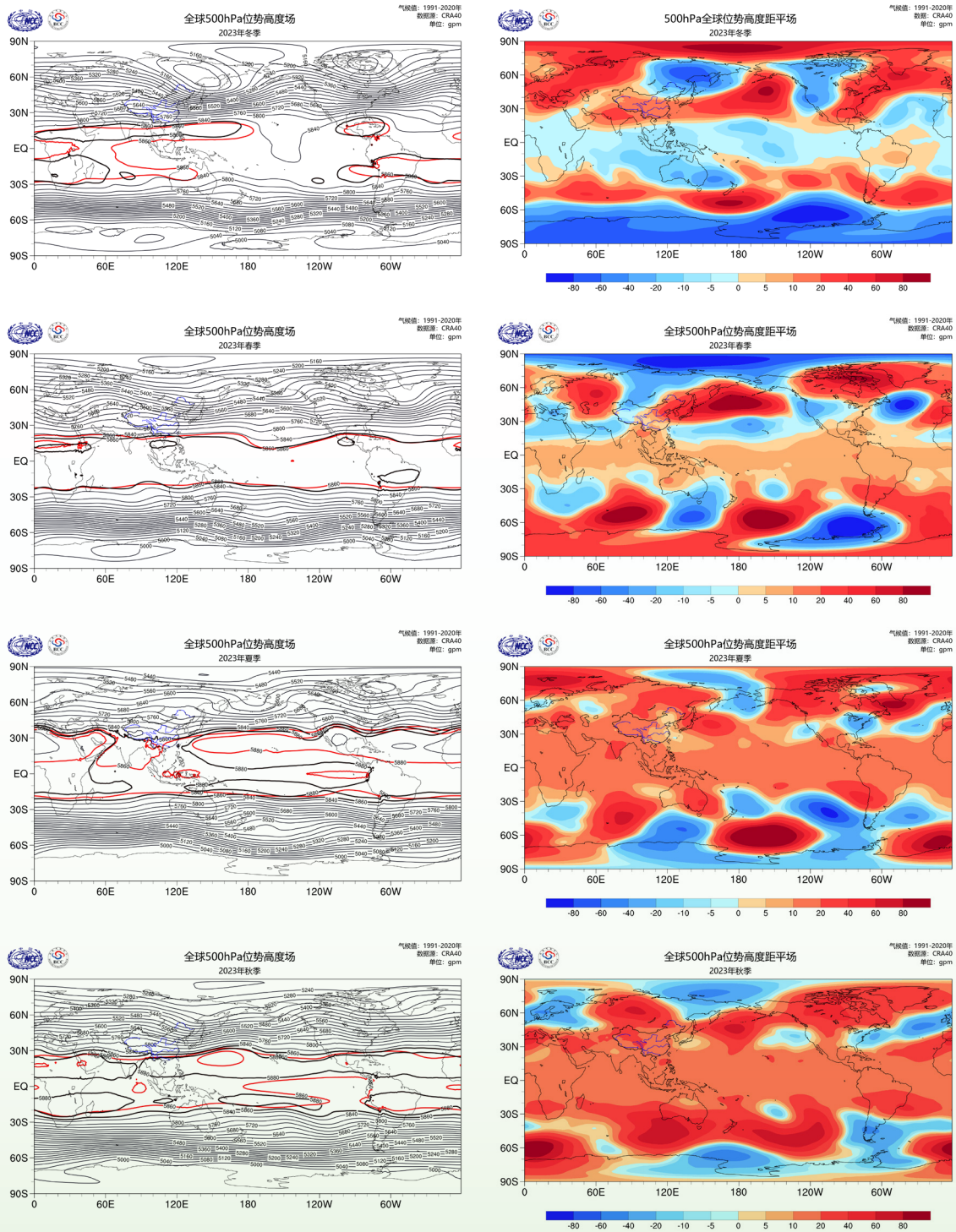
Figure 2.2 Global seasonal average 500 hPa geopotential height fields (left) and anomaly fields (right) in the winter, spring, summer, and autumn of 2023 (from top to bottom) (red isopleths on left−side images represent the climatological state)
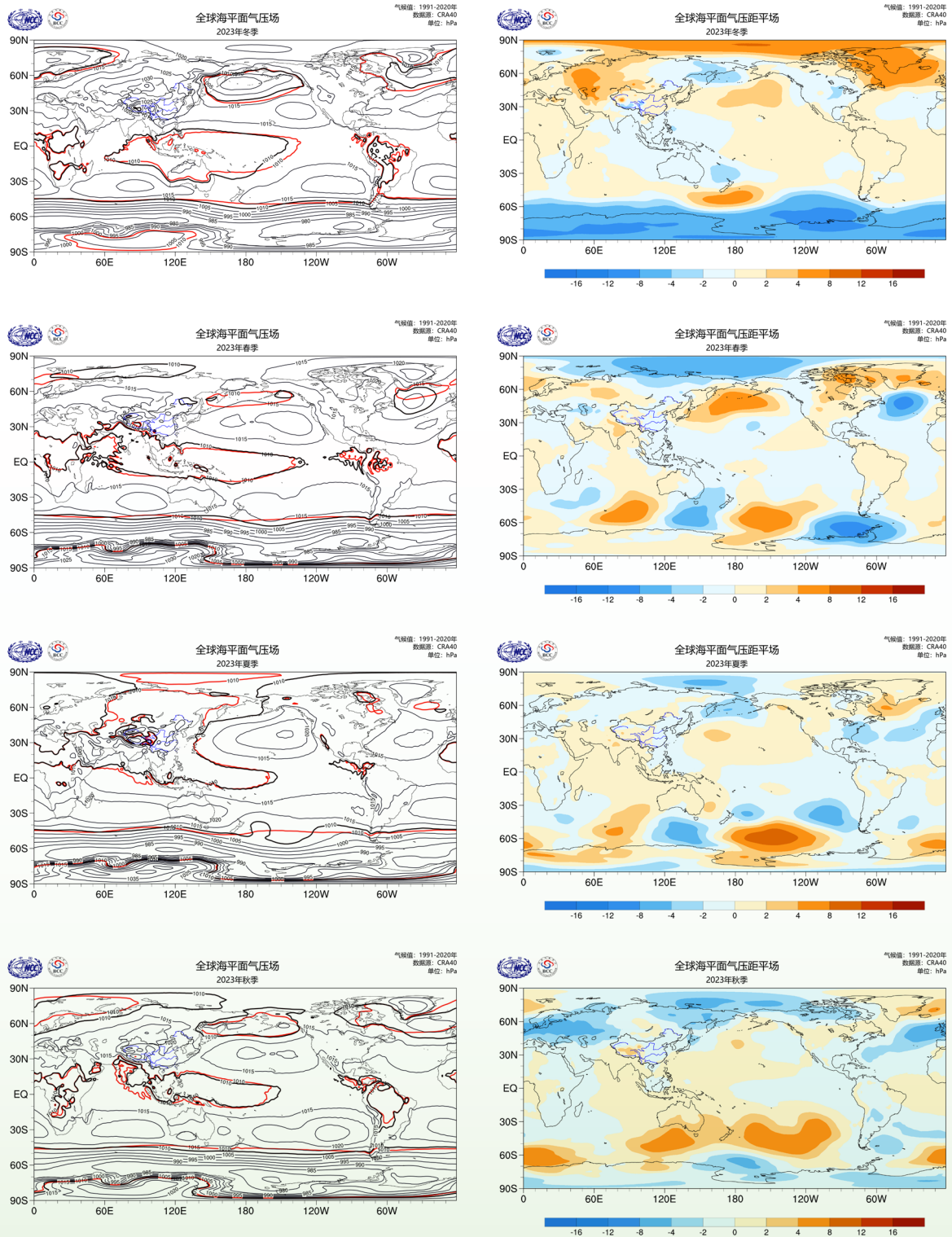
Figure 2.3 Global seasonal average SLP fields (left) and their anomalies (right) for the winter, spring, summer, and autumn of 2023 (from top to bottom) (red isopleths on left−side images represent the climatological state)

2.2 Major Atmospheric Circulations

2.2.1 Teleconnections and Oscillations

During the winter, summer, and autumn of 2023, the Arctic Oscillation was in a negative phase while in spring it was close to normal (Figure 2.4).

Figure 2.4 Historical series of the Arctic Oscillation for (a) winter, (b) spring, (c) summer, and (d) autumn from 1979 to 2023

In 2023, the North Atlantic Oscillation was in a negative phase throughout all four seasons (Figure 2.5).
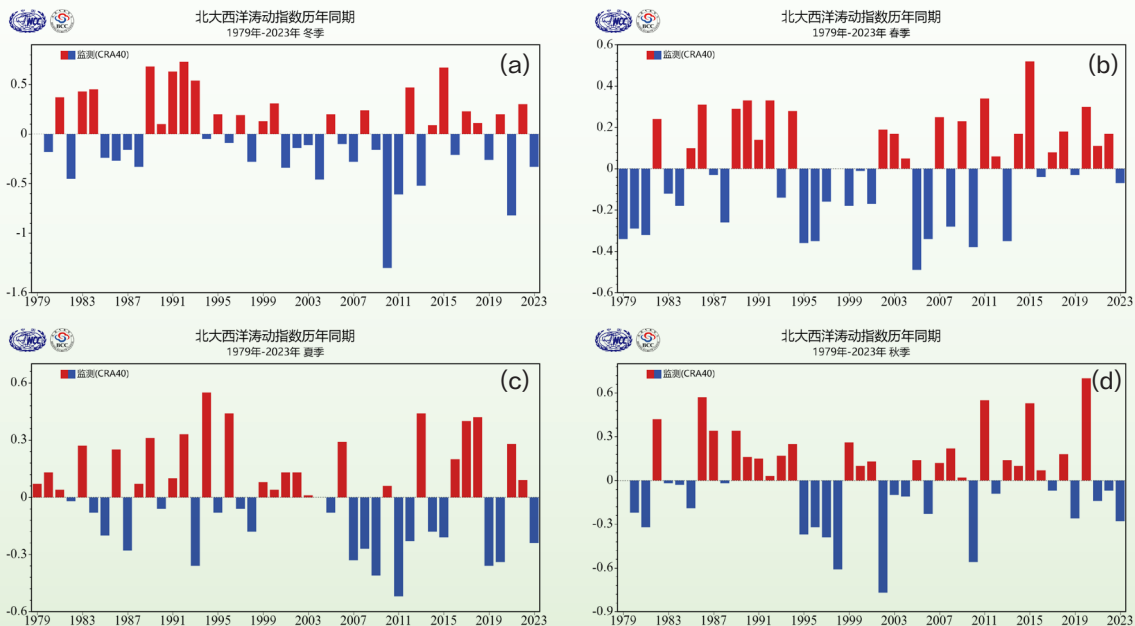
Figure 2.5 Historical series of the North Atlantic Oscillation for (a) winter, (b) spring, (c) summer, and (d) autumn from 1979 to 2023

During the winter of 2023, the Antarctic Oscillation recorded its strongest positive phase for that season since 1979. It remained in a positive phase during the spring and autumn, while transitioning to a weak negative phase in the summer (Figure 2.6).
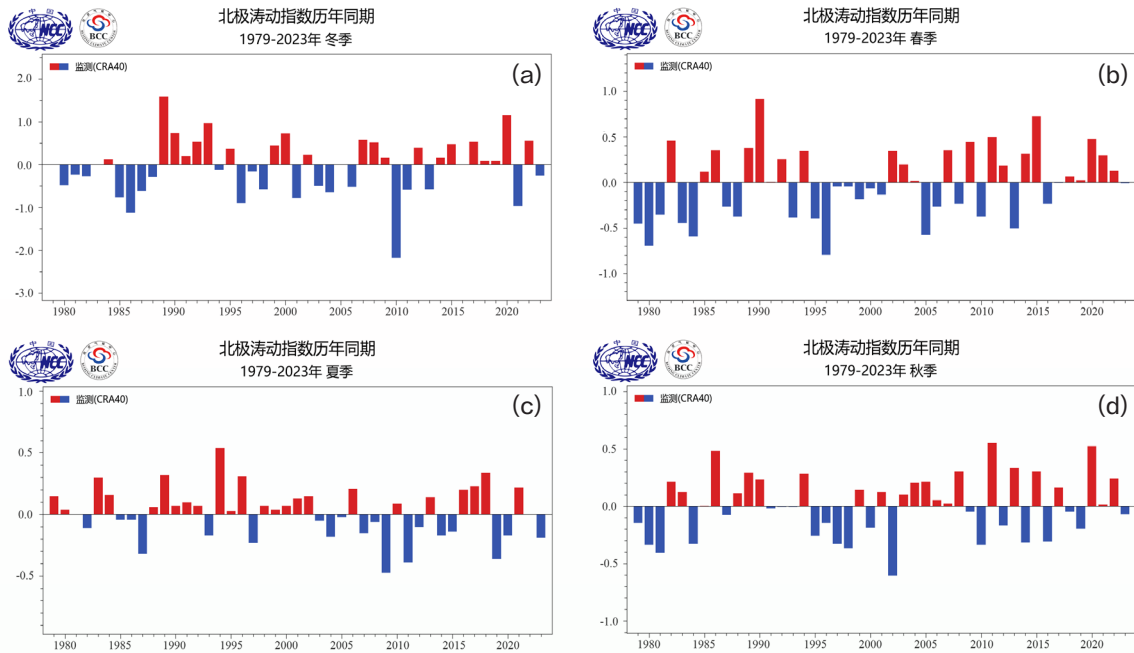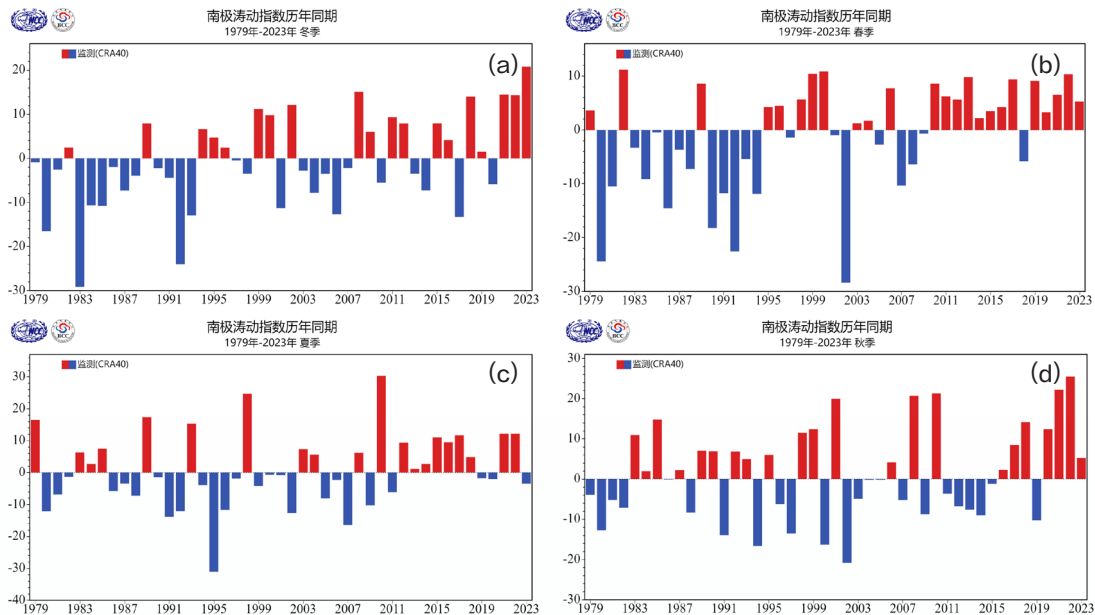

Figure 2.6 Historical series of the Antarctic Oscillation for (a) winter, (b) spring, (c) summer, and (d) autumn from 1979 to 2023

The Pacific-North American teleconnection pattern was in a negative phase only during the spring of 2023, while it was in a positive phase during the winter, summer, and autumn. It is worth noting that the index reached its strongest positive phase during the summer since 1979 (Figure 2.7).
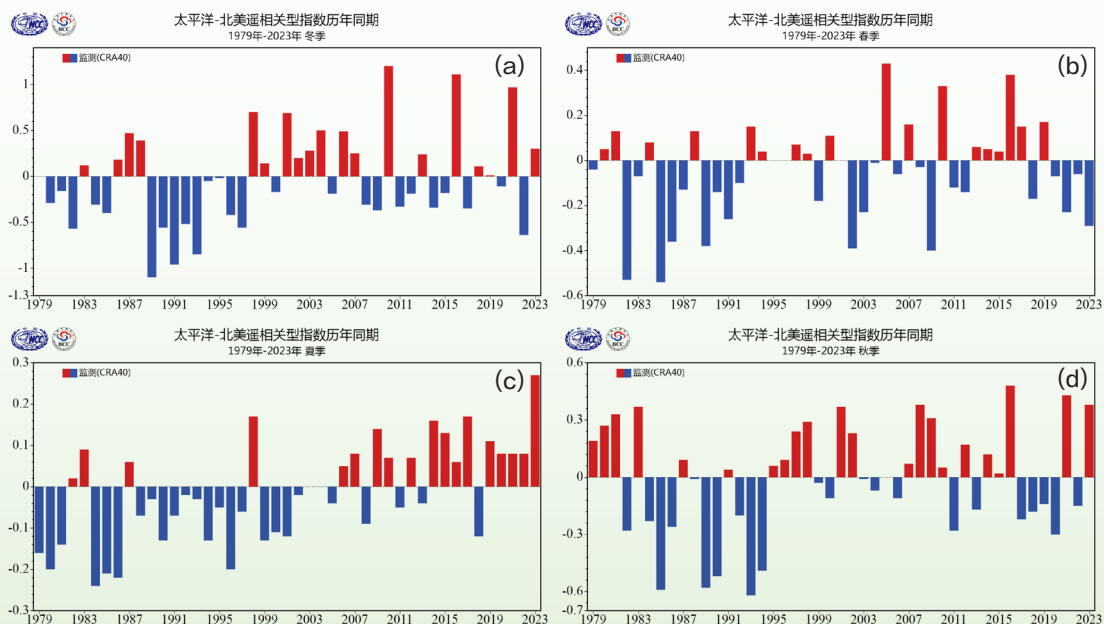
Figure 2.7 Historical series of the Pacific–North American teleconnection pattern for (a) winter, (b) spring, (c) summer, and (d) autumn from 1979 to 2023

The meridional East Asia-Pacific teleconnection pattern entered its third strongest negative phase since 1979 during the winter of 2023. It then transitioned to positive phases in the spring, summer, and autumn (Figure 2.8).
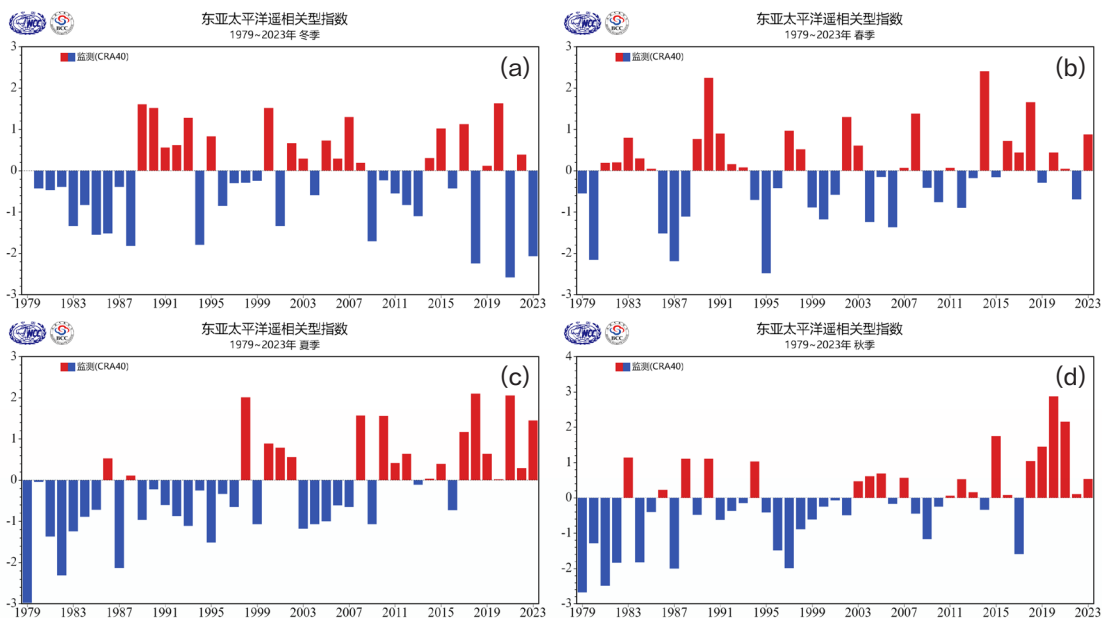
Figure 2.8 Historical series of the East Asia−Pacific teleconnection pattern for (a) winter, (b) spring, (c) summer, and (d) autumn from 1979 to 2023

2.2.2 Eurasian Blocking Highs

Compared to the long-term average, the number of days with blocking highs in the mid to high latitudes (40°E - 70°E) of Eurasia was close to normal but slightly lower during the winter of 2023. In spring, it was above the long-term average, while in summer and autumn, it fell below the averages (Figure 2.9).
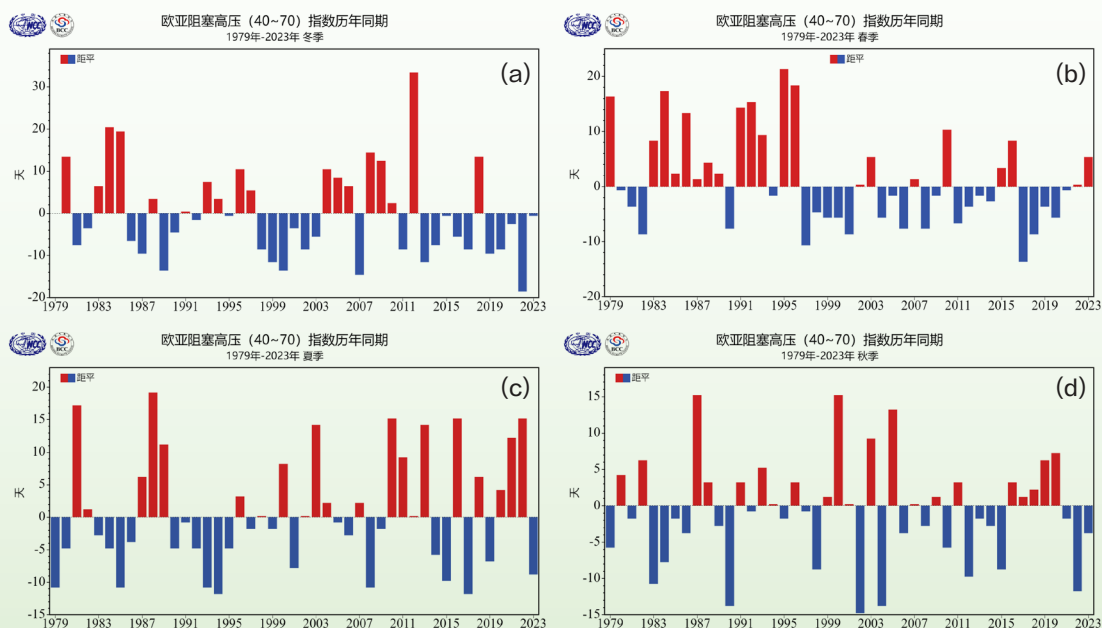
Figure 2.9 Historical anomaly series of the number of blocking high days in the Eurasian region (40°E − 70°E) (in days)

Compared to the long-term averages, the number of days with blocking highs in the mid to high latitudes of Asia (80°E - 110°E) was below normal in the winter, significantly above normal in the spring, reaching the highest level since 1979 for spring, below normal in the summer, and above normal in the autumn (Figure 2.10).
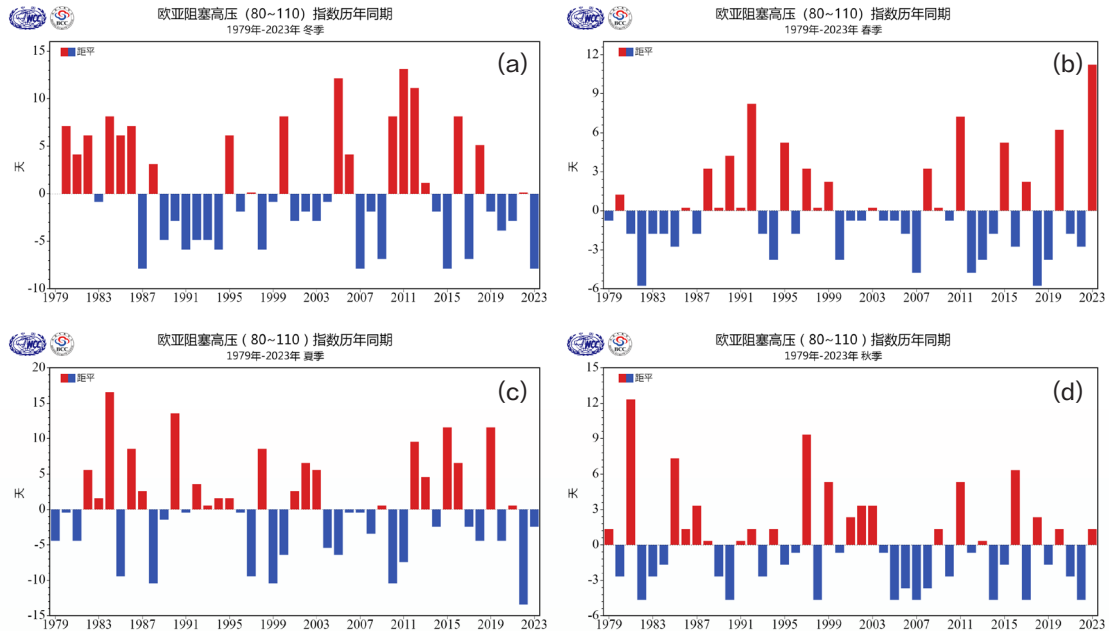
Figure 2.10 Historical anomaly series of the number of blocking high days in the Asian region (80°E – 110°E) (in days)

Compared to the long-term averages, the number of days with blocking highs in the mid to high latitudes of Asia (120°E - 150°E) was below normal during the winter and spring, above average during the summer, and close to normal during the autumn (Figure 2.11).
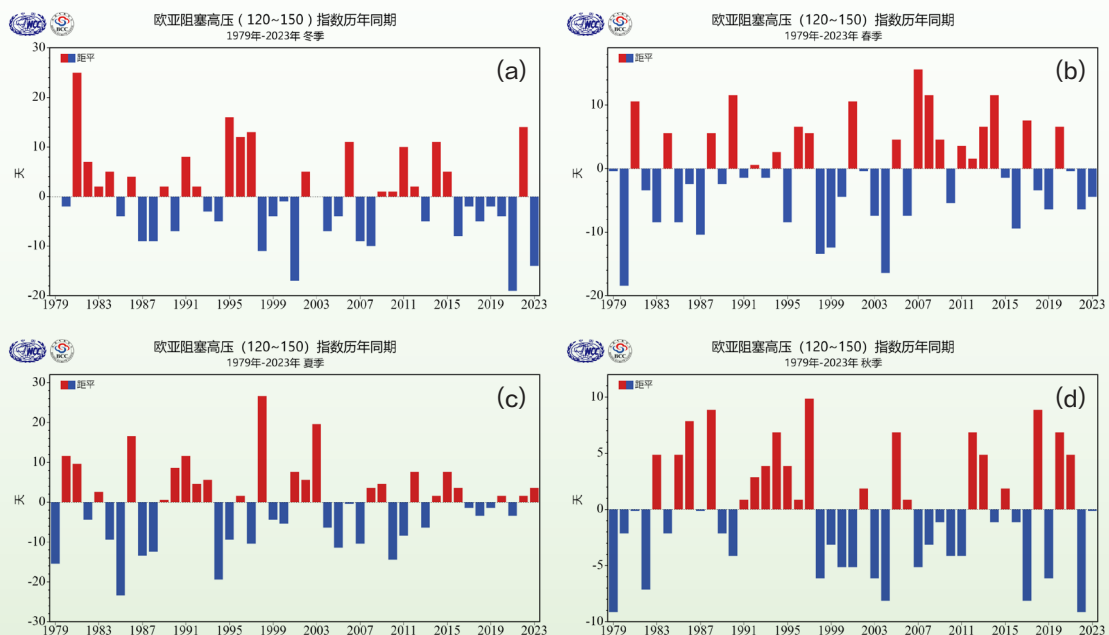
Figure 2.11 Historical anomaly series of the number of blocking high days in the Asian region (120°E – 150°E) (in days)

2.2.3 East Asian Winter and Summer Monsoons

During the winter of 2023, both the East Asian winter monsoon and the Siberian High exhibited intensity surpassing their respective long-term averages for the same period (Figure 2.12). In the summer of 2023, the intensity of both the South China Sea summer monsoon and the East Asian summer monsoon fell below the long-term averages for the same period (Figure 2.13).
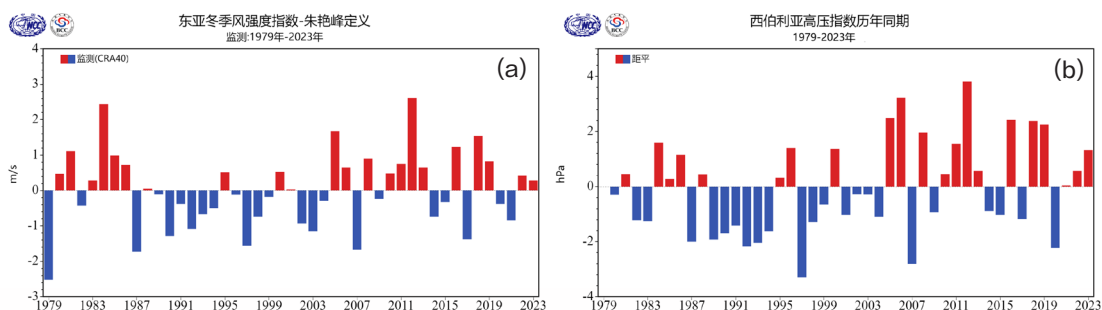
Figure 2.12 Historical series of the East Asian winter monsoon intensity (a) and the Siberian High intensity (b)
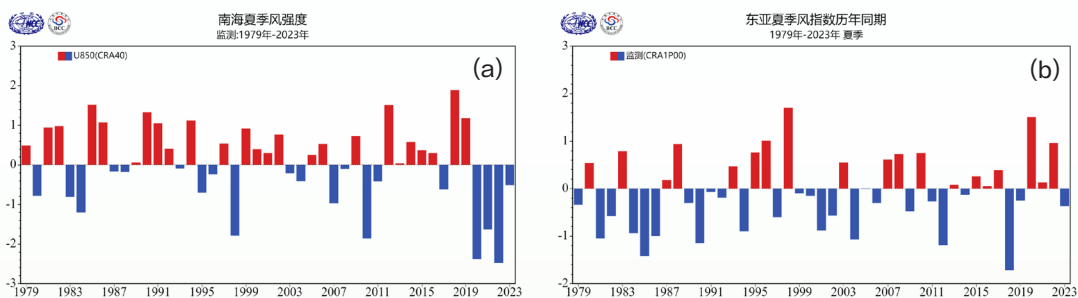
Figure 2.13 Historical series of the South China Sea summer monsoon intensity (a) and the East Asian summer monsoon intensity (b)

2.2.4 Other Monsoons Around the World

In comparison to the long-term averages for the same season, the North American monsoon exhibited greater intensity during the winter and lower intensity during the summer in 2023 (Figure 2.14).
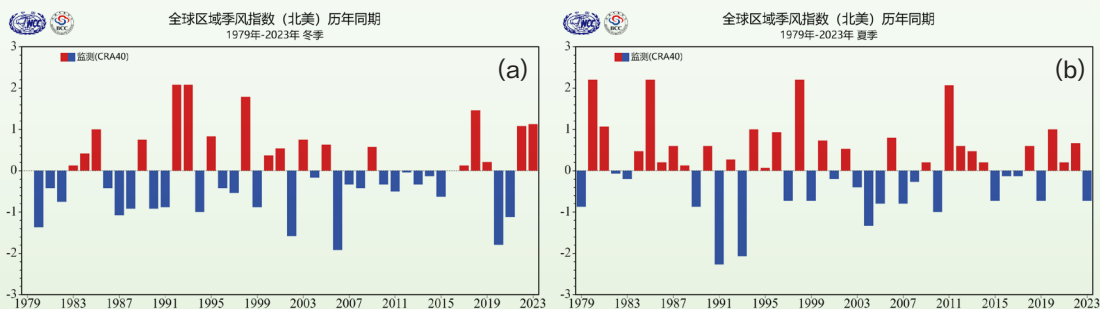
Figure 2.14 Historical series of the North American monsoon for (a) winter and (b) summer

In 2023, the West African monsoon was weaker in both the winter and summer compared to the long-term averages for the same season (Figure 2.15).
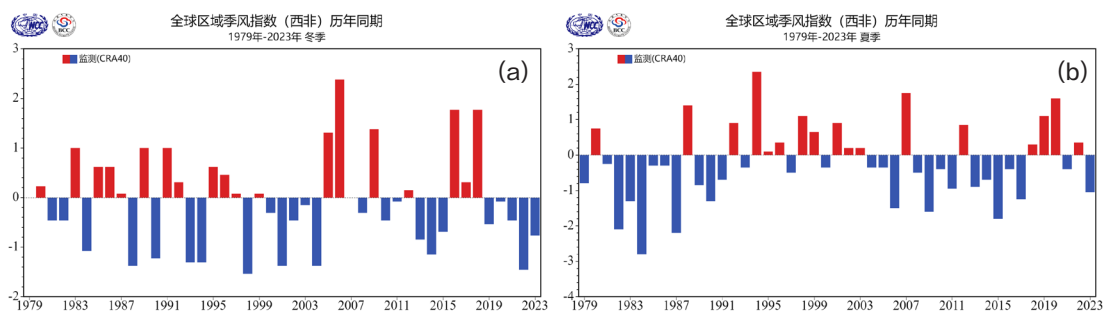
Figure 2.15 Historical series of the West African monsoon for (a) winter and (b) summer

In 2023, the South Asian monsoon was stronger in the winter and weaker in the summer compared to the long-term averages for the same season. In particular, the summer index reached its lowest level for the same period since 1979 (Figure 2.16).
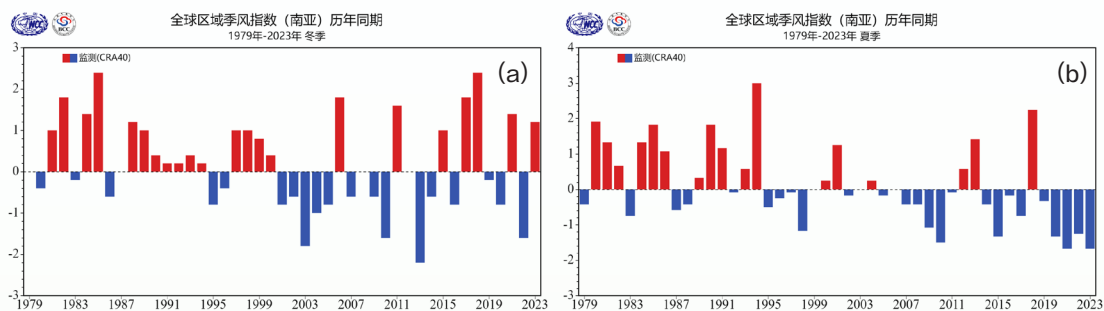
Figure 2.16 Historical series of the South Asian monsoon for (a) winter and (b) summer

Chapter III Global Oceans

In 2023, sea surface temperatures (SSTs) in most global ocean areas were near or above the long-term averages. Notably, SSTs in the central North Pacific were over 2.0 ℃ above the average, and the equatorial central and eastern Pacific showed higher-than-average SSTs. After the La Niña event concluded in January 2023, the equatorial central and eastern Pacific transitioned into an El Niño phase by May and met the El Niño criteria by October 2023. This El Niño event significantly intensified during the autumn and winter, with the warm water centre in the tropical central and eastern Pacific exceeding 3.0 ℃ in December.

3.1 Global SSTs

In 2023, mean SSTs in most global ocean areas were near or above their long-term averages. SSTs were higher by more than 0.5 ℃ in the central North Pacific, tropical Pacific, western mid-latitudes of the South Pacific, western Indian Ocean, mid-latitudes of the North Atlantic, tropical Atlantic, and mid-latitudes of the South Atlantic. Notably, SSTs exceeded 1.0 ℃ above the averages in the central North Pacific, equatorial central and eastern Pacific, western South Pacific, mid-latitudes of the southern Indian Ocean, eastern tropical Atlantic, and mid-latitudes of the South Atlantic, with localized areas even showing increases of more than 1.5 ℃. In the tropical central and eastern Pacific, the average SSTs exceeded the long-term averages. Particularly, the SST anomalies in the equatorial region and southern areas were greater than 2.0 ℃ (Figure 3.1).
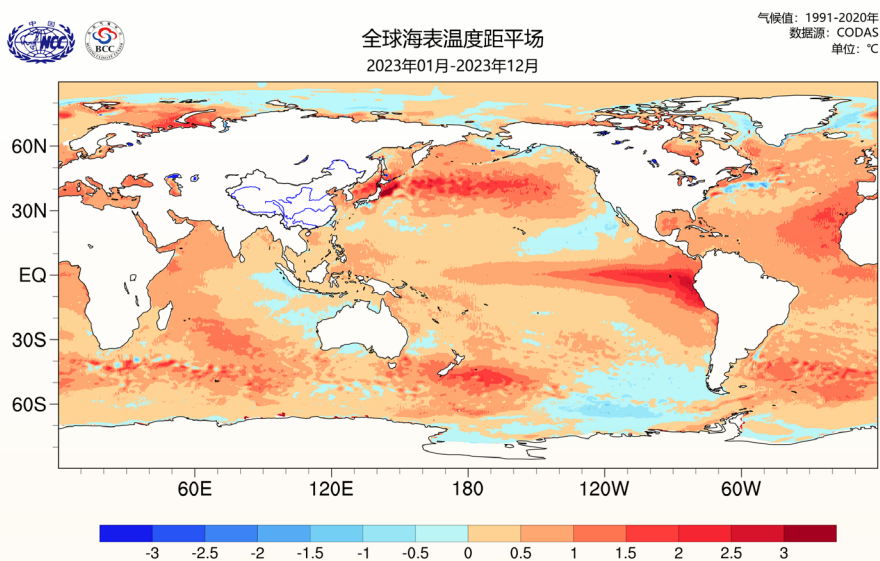
Figure 3.1 Global SST anomalies in 2023 (in ℃)

The distribution of average SST anomalies across different seasons shows that during the winter of 2023, SSTs in most of the central and eastern equatorial Pacific were below the long-term averages for the same season. The negative anomaly centre in the eastern equatorial Pacific was lower than -0.5 ℃. In the central North Pacific and the western mid-latitudes of the South Pacific, SSTs were above the historical averages for winter, with anomaly centres exceeding 2.0 ℃. With the exception of the eastern equatorial Indian Ocean, most of the rest of the Indian Ocean exhibited SSTs that were close to or above the long-term averages for winter. This was particularly true in the mid-latitudes of the southern Indian Ocean where the anomaly centre was more than 2.0 ℃ above average. In the Atlantic, most regions exhibited hig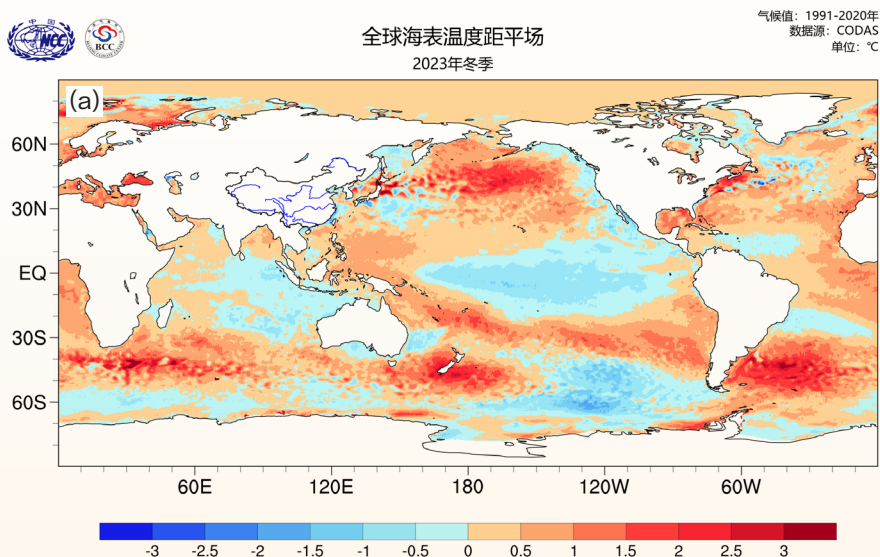her SSTs than the historical averages for winter. Positive anomaly centres were observed above 2.0 ℃ along the east coast of North America and in the mid to high latitudes of the South Atlantic (Figure 3.2a).

In the spring, cold SST anomaly centres in the equatorial central and eastern Pacific shifted towards the Northern Hemisphere, albeit with reduced intensity and extent compared to the winter. The eastern Pacific experienced anomalous warming, while warm SST anomalies persisted in the North Pacific and western mid-latitudes of the South Pacific. The Indian Ocean was predominantly warmer, with significant warming in the southern Indian Ocean compared to the winter. The SSTs across much of the North and South Atlantic mostly remained higher than normal, with the exception of some areas south of Greenland that experienced cold SST anomalies (Figure 3.2b).

During the summer, there was a shift in SST anomalies in the equatorial central and eastern Pacific to widespread anomalously warm conditions. The eastern warm SST anomaly centre exceeded 3.0 ℃. Warm SST anomalies persisted in the North Pacific and western mid-latitudes of the South Pacific. Warm SST anomalies in the Indian Ocean increased compared to the spring. The North Atlantic, equatorial Atlantic, and South Atlantic continued to maintain warm SSTs. Additionally, SSTs in the Barents Sea-Kara Sea of the Arctic Ocean exhibited an anomalous increase, with the positive anomaly centre exceeding 3.0 ℃ (Figure 3.2c).

In the autumn, the equatorial central and eastern Pacific maintained warm SST conditions, while the North Pacific and western mid-latitudes of the South Pacific continued to experience warm SST anomalies. The tropical Indian Ocean maintained warm SSTs, and the North Atlantic showed continued warm SSTs (Figure 3.2d).

全球海表温度距平场
2023年春季

气候值：1991-2020年
数据源：CODAS
单位：℃

全球海表温度距平场
2023年夏季

气候值：1991-2020年
数据源：CODAS
单位：℃

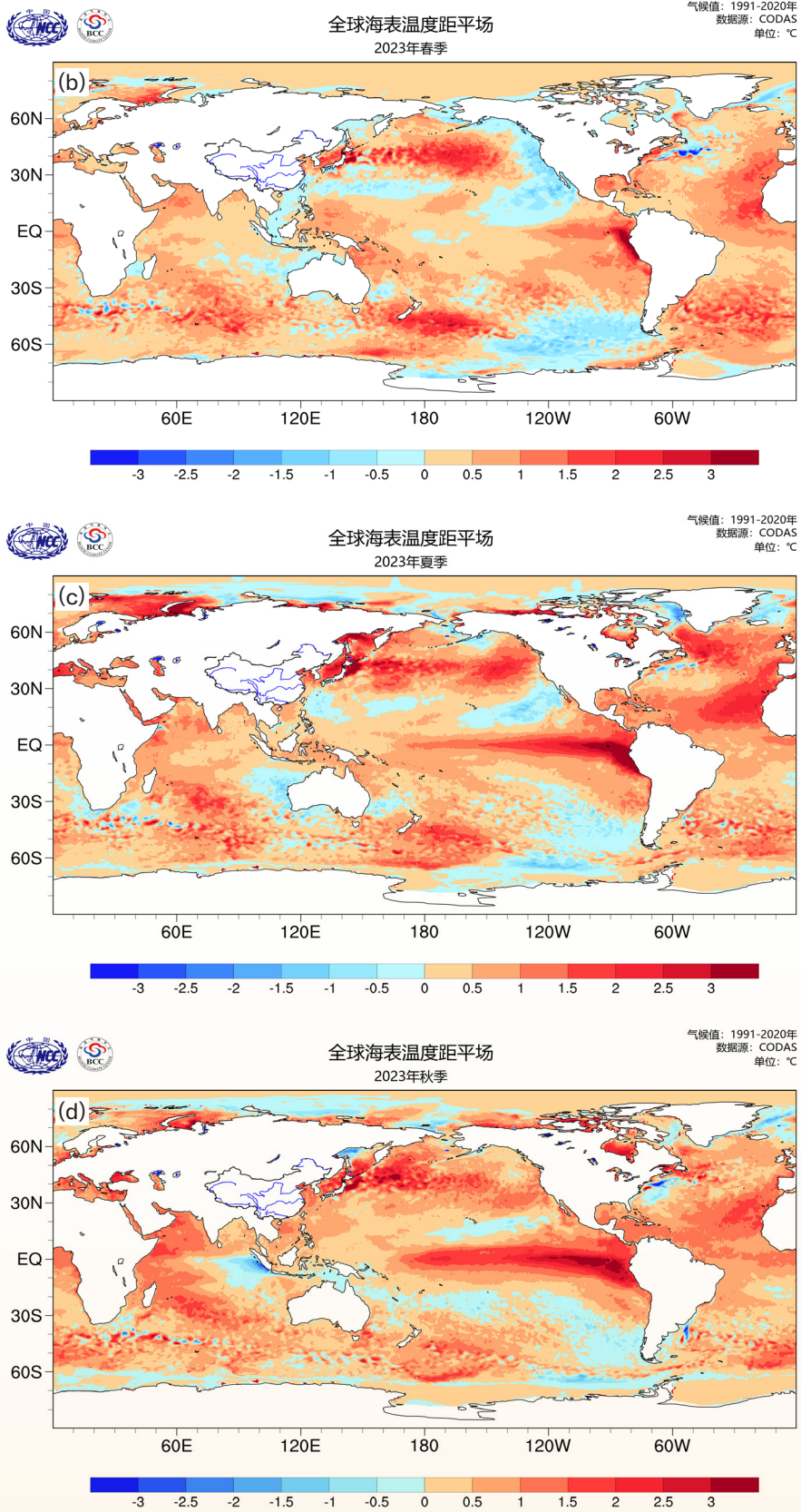全球海表温度距平场
2023年秋季

气候值：1991-2020年
数据源：CODAS
单位：℃

Figure 3.2 Global seasonal SST anomalies in 2023 for (a) winter, (b) spring, (c) summer, and (d) autumn (in ℃)

3.2 Pacific Ocean SSTs

El Niño and La Niña are phenomena characterized by a large-scale, persistent abnormal warming and cooling of the sea surface in the central and eastern equatorial Pacific Ocean. These events represent the strongest signal in the interannual variability of the climate system. From 1979 to 2023, the SSTs in the Niño 3.4 region of the central and eastern equatorial Pacific exhibited significant interannual variability. According to the "El Niño/La Niña Event Discrimination Method" (National Committee for Climate and Climate Change Standardization, 2017), between 1979 and 2023, the central and eastern equatorial Pacific experienced 14 El Niño and 11 La Niña events.

El Niño/La Niña events are typically classified as Eastern or Central types based on the location of SST anomaly centres. Eastern type events, also known as Eastern Pacific type or cold tongue type, have anomaly centres in the eastern equatorial Pacific and are characterized by the EP index. Central type events, also known as Central Pacific type or warm pool type, have anomaly centres in the central equatorial Pacific and are characterized by the CP index. Out of the 14 El Niño events recorded between 1979 and 2023, 8 were of the Eastern type and 6 were of the Central type (Figures 3.4 and 3.5). The majority of these events began in autumn, with 6 instances, followed by spring and summer, each with 4 occurrences. The most common ending season was spring, with 6 instances, followed by winter with 4, and summer with 3 (Figure 3.3). Out of the 11 La Niña events, 9 were of the Eastern type and 2 were of the Central type. The majority of these events began in summer and autumn, each with 5 instances, with an additional occurrence starting in spring. The most common ending season was spring, with 7 instances, followed by summer with 2, and winter with 2. In recent years, there have been frequent consecutive El Niño/La Niña events. For example, the super El Niño event from 2014 to 2016 lasted two winters and is historically rare. From September 2018, there were consecutive occurrences of two El Niño events, followed by two La Niña events, which is also rare historically.

According to monitoring data from the National Climate Centre, the La Niña event that began in September 2021 concluded in January 2023. By May 2023, conditions in the central and eastern equatorial Pacific had transitioned to an El Niño state, which fully met the criteria for an El Niño event by October 2023. The Niño 3.4 index was at -0.74 ℃ in the winter, but shifted to warm SST anomalies with indices of 0.13 ℃, 0.83 ℃, and 1.63 ℃ in the spring, summer, and autumn of 2023, respectively (Figure 3.3). This El Niño event was determined to be primarily of the Eastern type since its peak corresponded with a higher EP index than CP index (Figures 3.4 and 3.5). The changes in SST anomalies in the Pacific, as shown by the FY-3E MERSI SST product, reflected the evolution of the 2023 ENSO event (Figure 3.6).

The Southern Oscillation (SO) phenomenon is a reflection of the interaction between the tropical ocean and atmosphere. El Niño and La Niña events correspond to the negative and positive phases of the SO, respectively. In 2023, the Southern Oscillation Index (SOI) showed a positive anomaly in the winter, then stabilized in negative anomalies (Figure 3.7). This demonstrates the tropical atmosphere's response to the shift from cold to warm SST anomalies in the central and eastern equatorial Pacific.

Figure 3.3 Historical series of the Niño 3.4 index from 1979 to 2023 for (a) winter, (b) spring, (c) summer, and (d) autumn (in ℃)

Figure 3.4 Historical series of the EP index from 1979 to 2023 for (a) winter, (b) spring, (c) summer, and (d) autumn (in ℃)
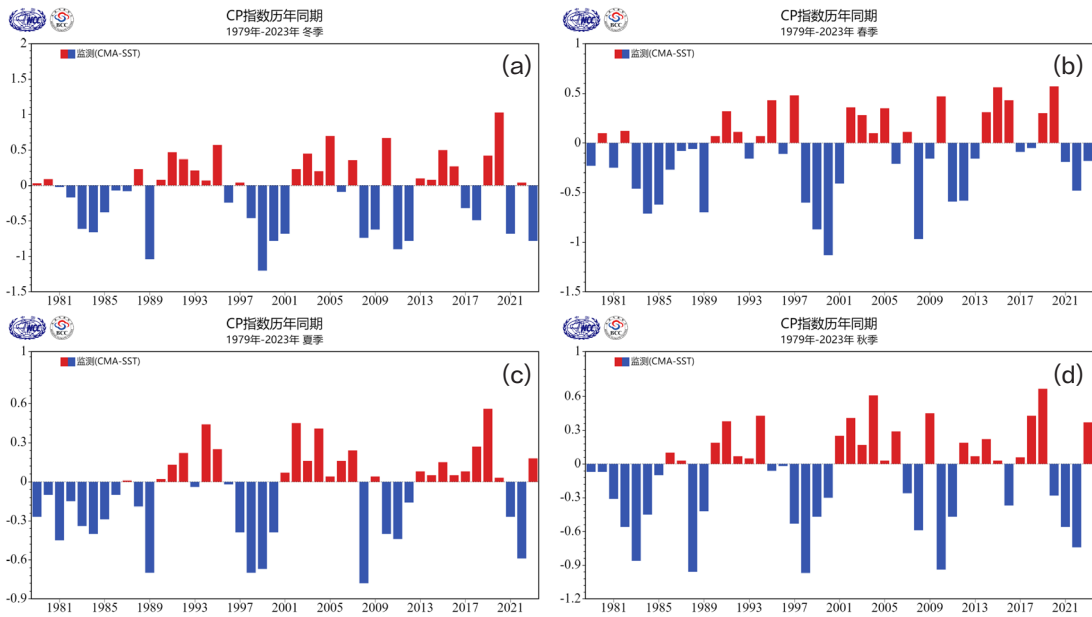
Figure 3.5 Historical series of the CP index from 1979 to 2023 for (a) winter, (b) spring, (c) summer, and (d) autumn (in ℃)
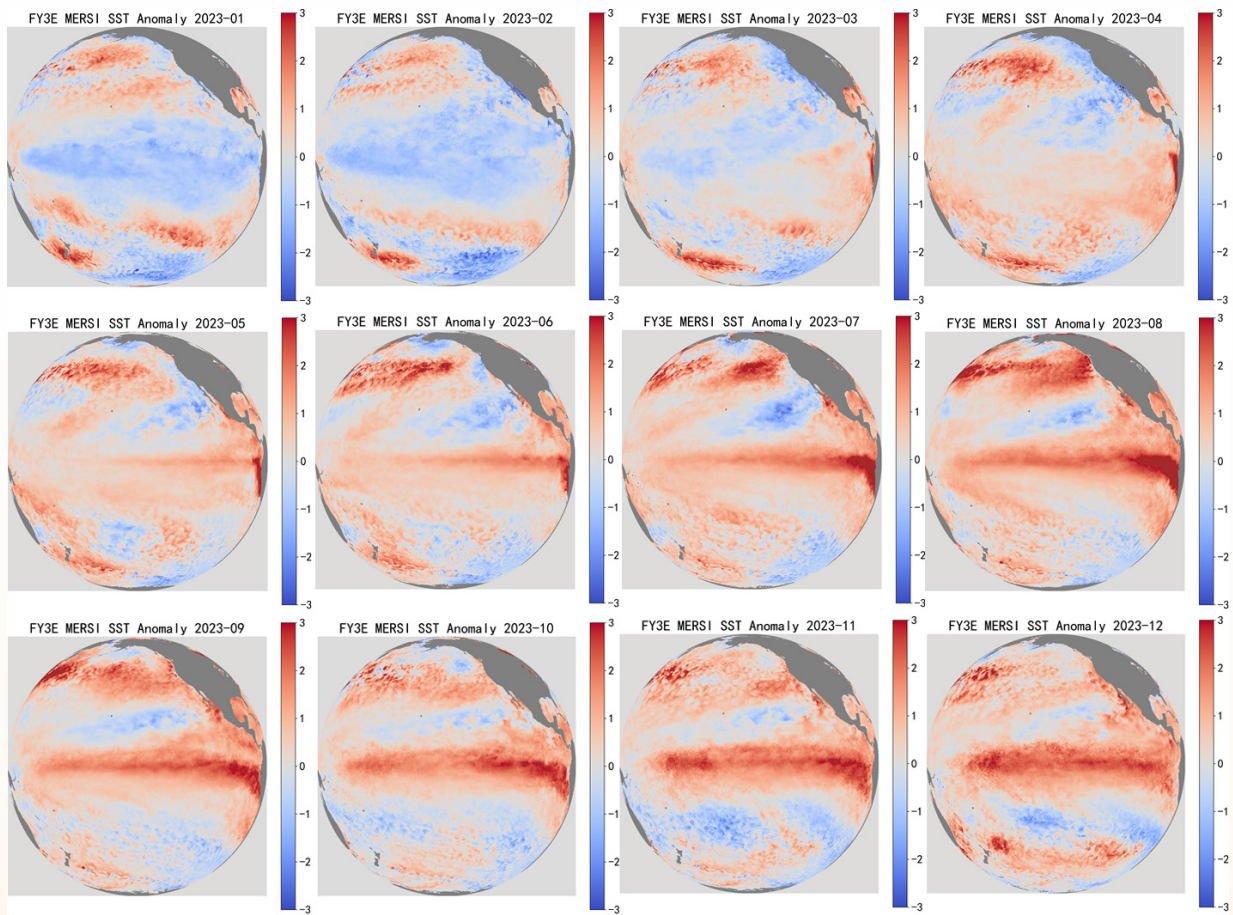
Figure 3.6 Monthly SST anomalies in 2023 monitored by FY−3E MERSI (Normal values: monthly average OISST from 1991 to 2020, in ℃)
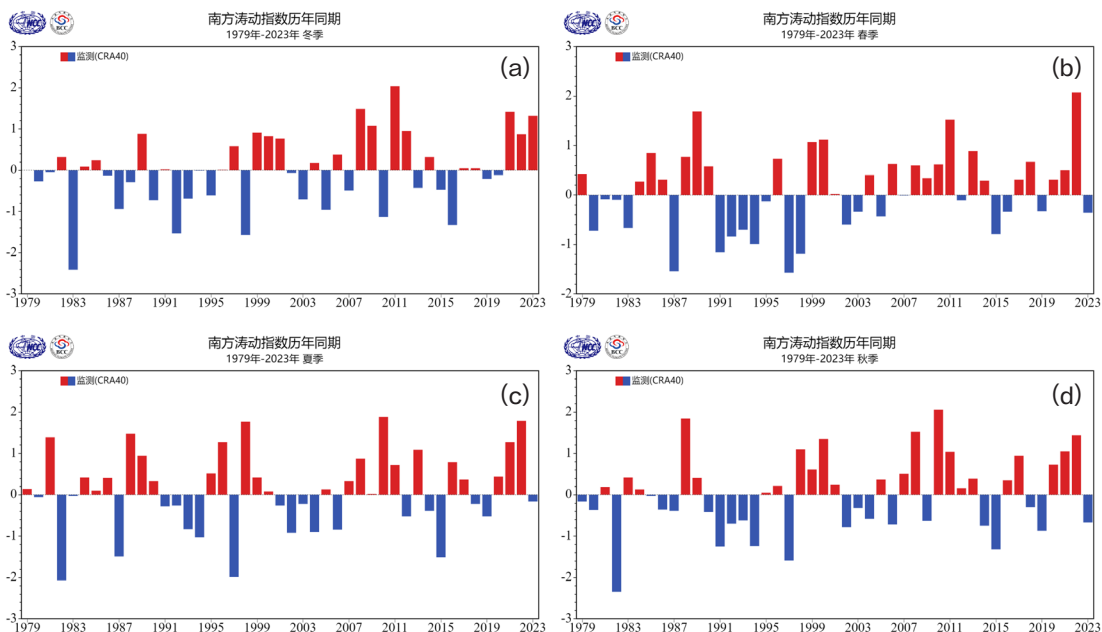
Figure 3.7 Historical series of the SOI from 1979 to 2023 for (a) winter, (b) spring, (c) summer, and (d) autumn (in ℃)

The Pacific Decadal Oscillation (PDO) is a type of climatic variability that occurs on the basin-wide spatial scale and the decadal temporal scale in the Pacific Ocean, primarily manifest in quasi-20-year and quasi-50-year cycles. During a warm phase of the PDO, SSTs in the central and eastern tropical Pacific are anomalously warm, while SSTs in the mid-latitude North Pacific are anomalously cool. Conversely, the distribution pattern of SST anomalies during a cold phase of the PDO is the exact opposite. Throughout the past century or so, cold phases of the PDO were observed during the periods of 1909-1925, 1943-1976, and 1998-2013, while warm phases were observed during the periods of 1926-1942 and 1977-1997. From 2014 to 2019, the PDO shifted from an earlier predominantly negative phase to a predominantly positive phase. Since 2020, the PDO has shifted back to a sustained negative phase, with the PDO index in 2023 at -1.58 ℃, a decrease of 0.14 ℃ from 2022 (Figure 3.8).
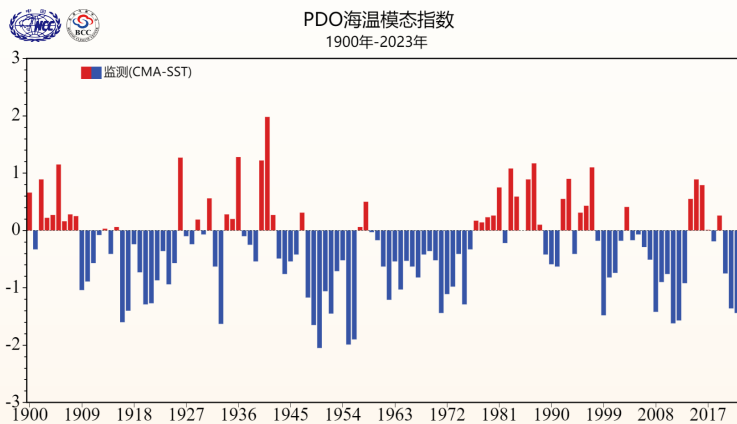
Figure 3.8 Annual average PDO index series since 1900 (in ℃)

3.3 Indian Ocean SSTs

The Indian Ocean Basin-Wide (IOBW) mode is defined as SST anomalies across the tropical Indian Ocean and is the primary mode of SST variability in the tropical Indian Ocean. It typically begins to develop in winter and reaches its peak in the following spring. From 1979 to 2023, the IOBW index showed a clear upward trend. From 1979 to the end of the last century, the tropical Indian Ocean SSTs were mostly below the long-term averages. However, since the beginning of this century, they have been mostly above normal (Figure 3.9). In 2023, the winter IOBW index was at -0.19 ℃. The index then gradually rose, shifted to a positive phase in the summer, and reached its peak in the autumn at 0.38 ℃.

Figure 3.9 Historical series of the IOBW index from 1979 to 2023 for (a) winter, (b) spring, (c) summer, and (d) autumn (in ℃)

The Tropical Indian Ocean Dipole (TIOD) characterizes the seesaw-like inverse variations between the SSTs of the tropical western Indian Ocean and the tropical southeastern Indian Ocean. The TIOD index is defined as the difference in SST anomalies between the tropical western Indian Ocean and the tropical southeastern Indian Ocean. The TIOD usually occurs in summer and dissipates in winter. In 2023, the TIOD showed a consistent positive phase, with the winter TIOD index at 0.42 ℃. The spring TIOD index slightly weakened to 0.22 ℃, and the summer to autumn TIOD indices continuously strengthened to 0.68 ℃ and 1.12 ℃, respectively (Figure 3.10).

The South Indian Ocean Dipole (SIOD) is a zonal dipole located in the subtropical region of the South Indian Ocean and is the secondary mode of SST variations in the Indian Ocean. It exhibits distinct seasonal phase-locking characteristics, typically begins to develop in early winter, reaches its peak strength from January to March of the following year, and then significantly weakens in April. The SIOD index is defined as the difference in average SST anomalies between the southwestern and southeastern Indian Ocean. In 2023, the SIOD index remained in a positive phase, with its peak occurring during the winter, followed by a weakening trend. The SIOD index values for the winter, spring, summer, and autumn were 1.51 ℃, 0.77 ℃, 0.73 ℃, and 0.62 ℃, respectively (Figure 3.11).
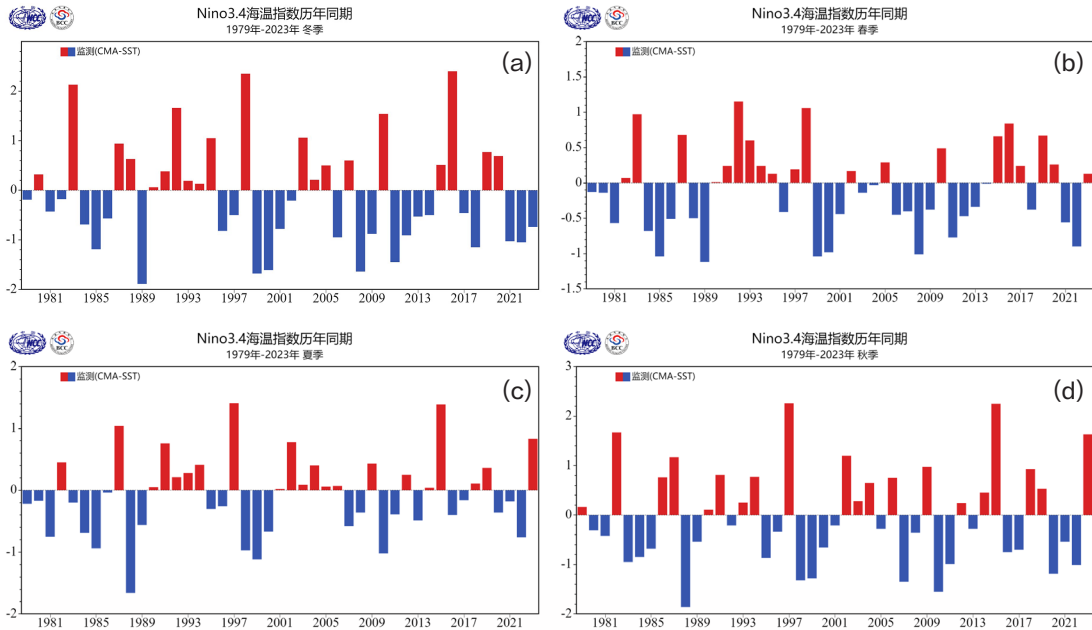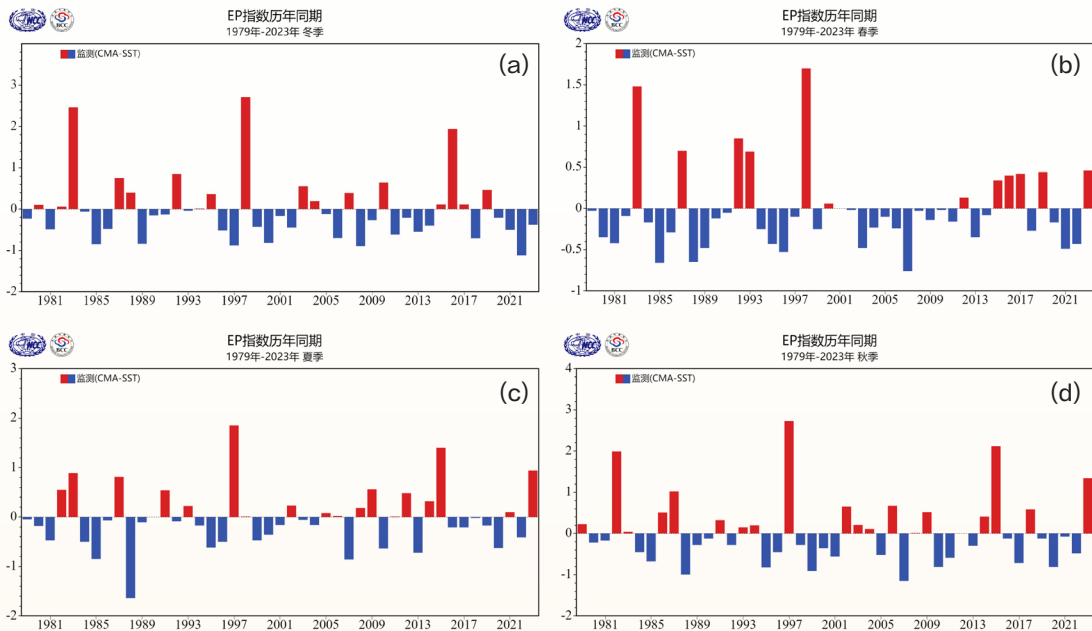
Figure 3.10 Historical series of the TIOD index from 1979 to 2023 for (a) winter, (b) spring, (c) summer, and (d) autumn (in ℃)
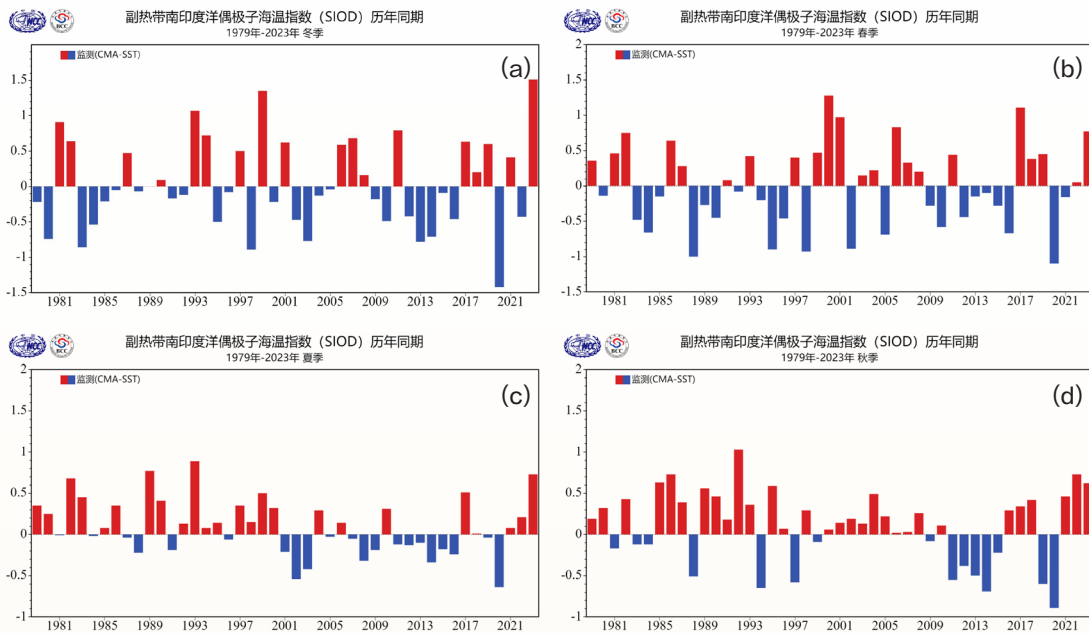
Figure 3.11 Historical series of the SIOD index from 1979 to 2023 for (a) winter, (b) spring, (c) summer, and (d) autumn (in ℃)

3.4 Atlantic Ocean SSTs

The North Atlantic Oscillation (NAO) is an important mode of high-latitude variability in the atmosphere of the Northern Hemisphere. On a seasonal scale, this atmospheric oscillation pattern induces a response in SSTs of the same region, resulting in a "- + -" tri-pole pattern of SST anomalies across the North Atlantic from south to north, associated with a positive phase of the NAO. This feature is characterized by

the North Atlantic Tri-pole (NAT) index. In the past decade, the NAT index has predominantly been in a positive phase. However, in 2023, except for the winter, which was close to 0 ℃, the spring, summer, and autumn all showed a significant negative phase. The index values were -0.54 ℃, -2.29 ℃, and -1.33 ℃, respectively (Figure 3.12).
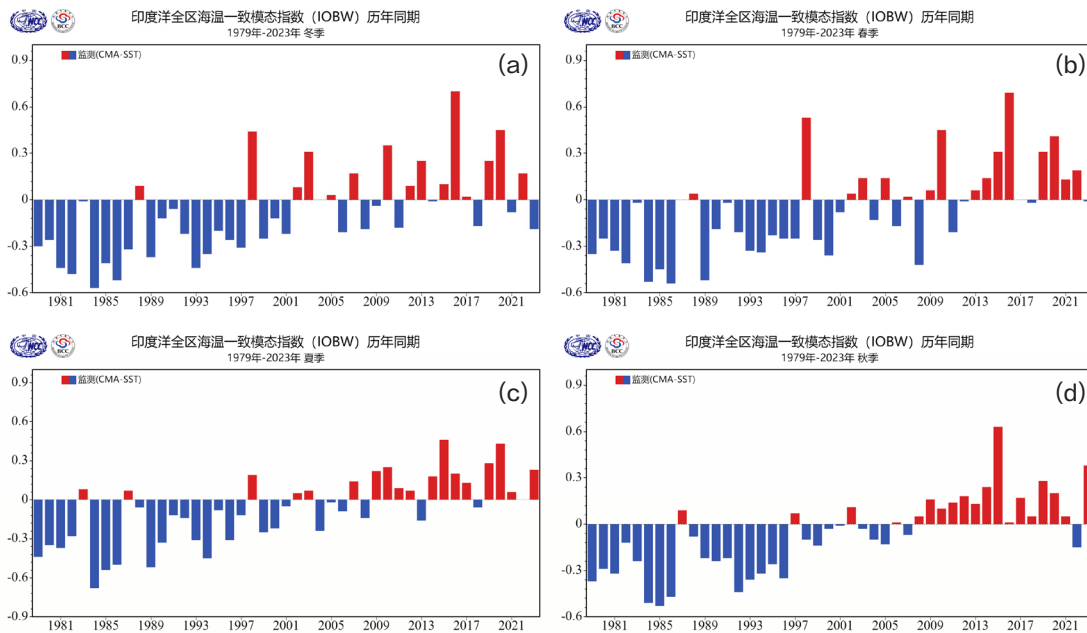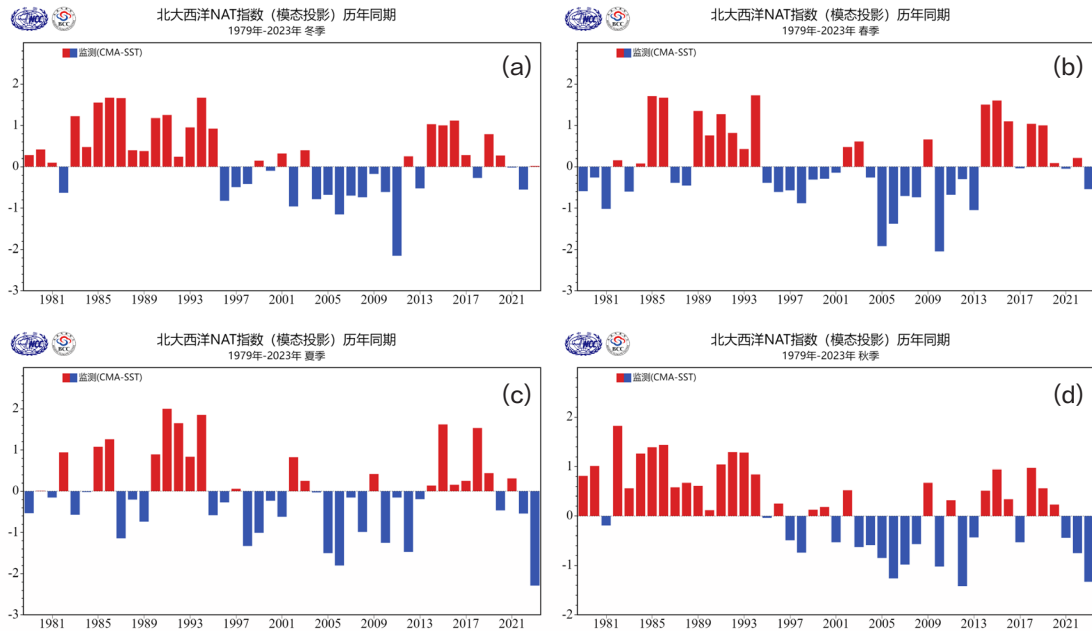
Figure 3.12 Historical series of the NAT index from 1979 to 2023 for (a) winter, (b) spring, (c) summer, and (d) autumn (in ℃)

SST anomalies in the tropical North Atlantic and the equatorial Atlantic affect the global climate through ocean-atmosphere interactions and atmospheric teleconnections. The strength of these anomalies can be characterized by SST anomaly indices for key ocean areas. From 1979 to 2023, the SST indices for the tropical North Atlantic and the equatorial Atlantic showed varying degrees of warming trends in all seasons. From the 1980s to the early 21st century, the SSTs in the tropical North Atlantic and the equatorial Atlantic were predominantly below the long-term averages, but over the past 20 years, they have been predominantly above normal (Figures 3.13 and 3.14). In the winter of 2023, the tropical North Atlantic SST index was -0.06 ℃, then it shifted to a positive phase and peaked in the summer, reaching an index value of 1.17 ℃. The equatorial Atlantic SST index maintained a positive phase, with its highest index in the summer at 0.70 ℃.

The Atlantic Multi-decadal Oscillation (AMO) is a mode of multi-decadal natural variability of SST anomalies that occur in the North Atlantic and has a basin-scale spatial pattern with an oscillation period of 65-80 years. From 1900 to 2023, North Atlantic SSTs showed clear decadal variations, transitioning between cold and warm phases. From the early 20th century to the 1920s, SSTs were generally lower than normal. From the 1930s to the 1950s, they were predominantly higher than normal. From the mid-1960s to the mid-1990s, temperatures again shifted to colder than normal. Since the late 1990s, North Atlantic SSTs have consistently been higher. In 2023, the annual AMO index increased by 0.12 ℃ from the previous year, reaching 0.36 ℃ (Figure 3.15).

Figure 3.13 Historical series of the tropical North Atlantic index from 1979 to 2023 for (a) winter, (b) spring, (c) summer, and (d) autumn (in ℃)
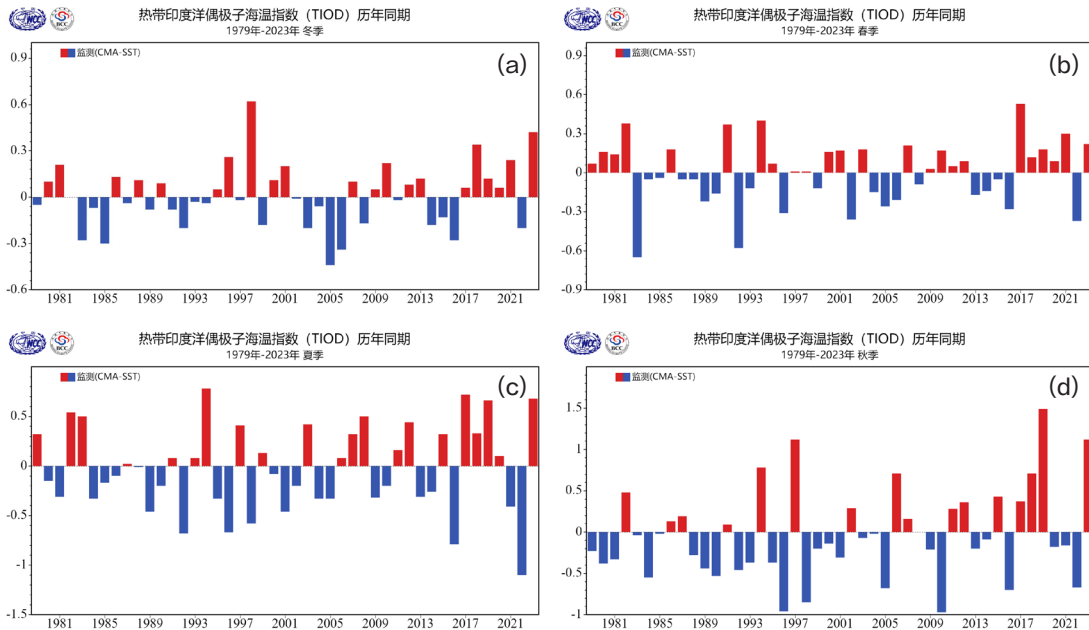

Figure 3.14 Historical series of the equatorial Atlantic index from 1979 to 2023 for (a) winter, (b) spring, (c) summer, and (d) autumn (in ℃)
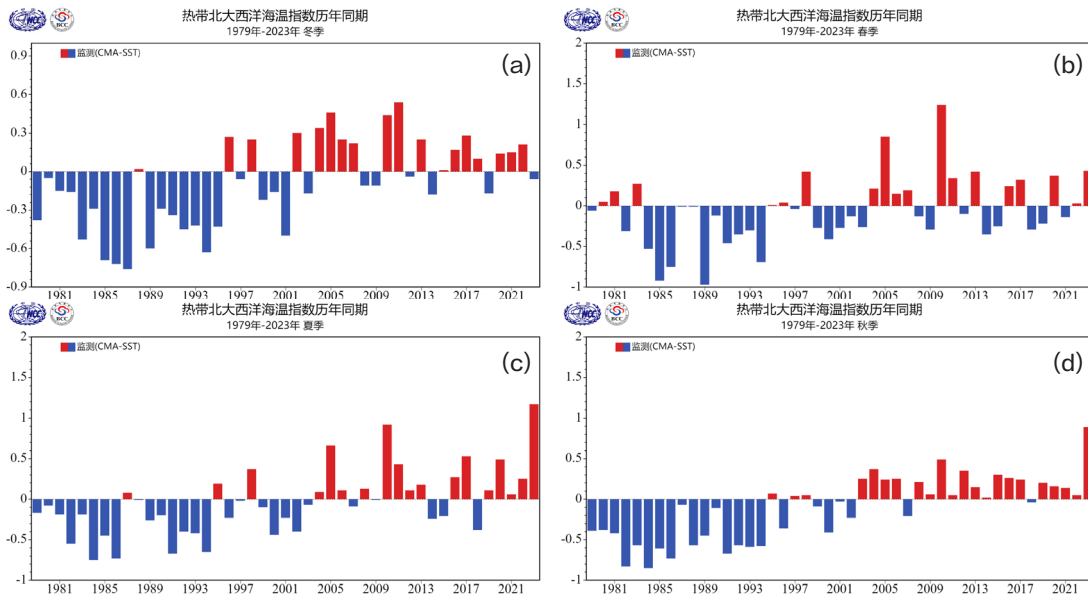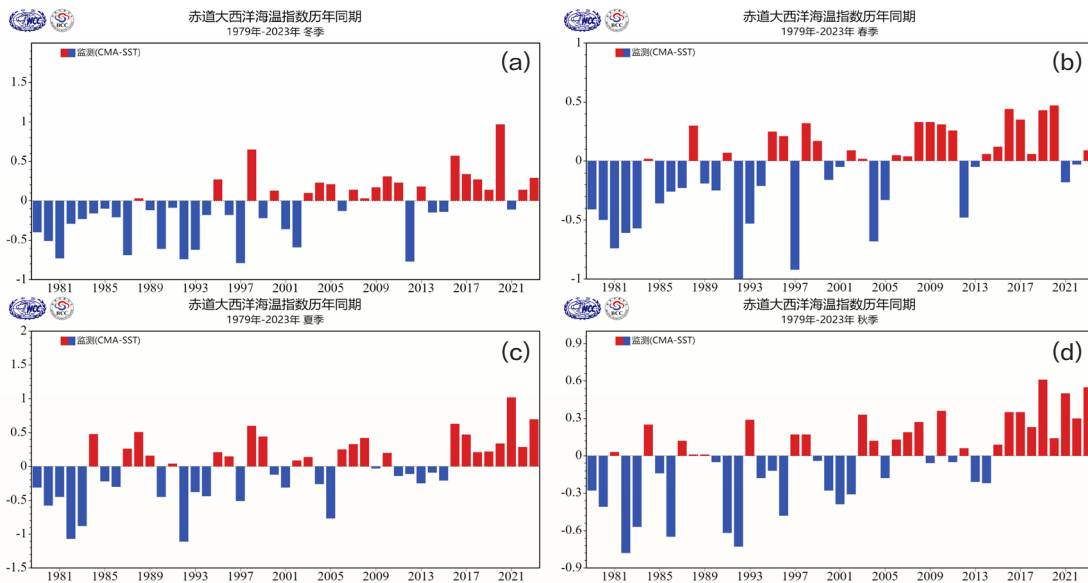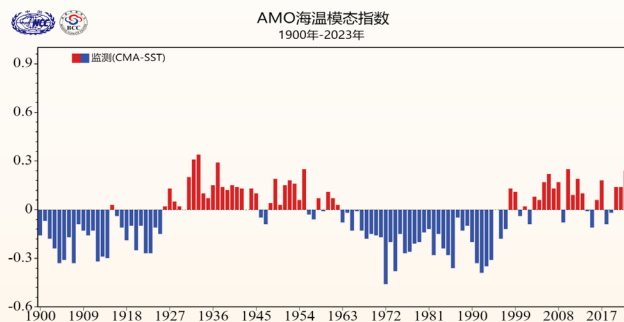

Figure 3.15 Annual average AMO index series since 1900 (in ℃)

Chapter IV Snow Cover and Sea Ice

In 2023, the snow cover area in both the Northern Hemisphere and Eurasia exceeded the long-term averages, while in China it remained consistent with the previous year. Throughout 2023, the monthly Arctic sea ice extent was consistently below the averages for the same period in previous years, with March and September experiencing reductions of 3.9% and 21.7%, respectively. Similarly, Antarctic sea ice had below-average extent every month throughout the year, with very significant reductions. In February and September, the extent was 38.2% and 9.7% smaller, respectively, marking the smallest for these two months since satellite observations began.

4.1 Snow Cover Monitoring

4.1.1 Snow Cover Area in the Northern Hemisphere

1. Annual Snow Cover Area

Between 1972 and 2023, the annual average snow cover area in both the Northern Hemisphere and Eurasia decreased significantly, with an average decrease of $0.13 \times 10^6 km^2$ and $0.10 \times 10^6 km^2$ per decade, respectively. However, in 2023, the snow cover area in both regions rebounded compared to 2022, reaching $22.49 \times 10^6 km^2$ and $13.15 \times 10^6 km^2$, respectively, which were above the long-term averages. The snow cover area in China has be increasing at an average rate of approximately $0.03 \times 10^6 km^2$ per decade, with a significant increase observed in Northeast China. However, the increase in the Tibetan Plateau and northern Xinjiang was not as noticeable. As of 2023, the snow cover area in China stood at $1.29 \times 10^6 km^2$, the same as in 2022, and the eighth highest on record (since 1972). The Tibetan Plateau had snow cover area of $0.49 \times 10^6 km^2$, which is 8.11% larger than the long-term average but decreased compared to 2022. In northern Xinjiang, the snow cover area was $0.28 \times 10^6 km^2$, which is an increase from the previous year and above the long-term average. The snow cover area in Northeast China (including eastern Inner Mongolia, the same below) was $0.47 \times 10^6 km^2$, which is above the long-term average and slightly decreased compared to 2022 (Figure 4.1).

2. Seasonal Snow Cover Area

From 1972 to 2023, the winter snow cover area in the Northern Hemisphere and Eurasia exhibited distinct interdecadal variations. During the 1980s and 1990s, snow cover was predominantly below average, while the early 21st century saw mostly above-average years. Similarly, changes in China, the Tibetan Plateau, northern Xinjiang, and Northeast China followed this pattern, with all these regions showing a linear increase in winter snow cover. Notably, northern Xinjiang experienced a significant linear growth in snow cover. In the winter of 2022/2023, the snow cover area in the Northern Hemisphere and Eurasia was $40.83 \times 10^6 km^2$ and $25.20 \times 10^6 km^2$, respectively, both below the long-term averages for the same period. Snow cover in China and the Tibetan Plateau measured $2.79 \times 10^6 km^2$ and $0.79 \times 10^6 km^2$, respectively, which are 2.81% and 14.91% less than the averages, indicating a significant decrease from the previous winter by 22.93% and 47.09%, respectively. In contrast, the snow cover in northern Xinjiang and Northeast China is 9.35% and 3.01% higher than the averages, respectively (Figure 4.2).

Figure 4.1 Long-term changes in mean annual snow cover area for (a) Northern Hemisphere, (b) Eurasia, (c) China, (d) Tibetan Plateau, (e) northern Xinjiang, (f) Northeast China. The black solid line represents the multi-year average, and the blue dashed line represents the linear trend over the entire period. Except for (f) Northeast China, which averaged 8 months from January to May and October to December, all others were 12-month averages (in $10^6 km^2$)

Figure 4.2 Long-term changes in mean winter snow cover area for (a) Northern Hemisphere, (b) Eurasia, (c) China, (d) Tibetan Plateau, (e) northern Xinjiang, (f) Northeast China. The black solid line represents the multi-year average, and the blue dashed line represents the linear trend over the entire period (in $10^6 km^2$)

Similar to the annual averages, the spring snow cover area in the Northern Hemisphere and Eurasia has shown a linear decreasing trend over the past 50 years, with the trend being more pronounced, reducing by $0.51\times10^6 km^2$ and $0.42\times10^6 km^2$ per decade, respectively. In the spring of 2023, both regions experienced a substantial recovery in snow cover area from 2022, with the Northern Hemisphere being 8.80% above the long-term average, the seventh largest since 1972. In China and on the Tibetan Plateau, the spring snow cover area drastically reduced in the early 1980s and has since fluctuated around the long-term averages. Northern Xinjiang's spring snow cover area has shown a significant linear decrease trend over the past 50 years, while Northeast China has also exhibited a declining trend. As of the spring of 2023, the snow cover area in China measured $0.80\times10^6 km^2$, below the long-term average and slightly reduced from the previous year. The Tibetan Plateau is 6.83% below the long-term seasonal average, while northern Xinjiang was 18.42% above normal, both showing increases from the previous year. Northeast China experienced a 40.38% decrease from the long-term seasonal average, which is the sixth smallest since 1972 (Figure 4.3).
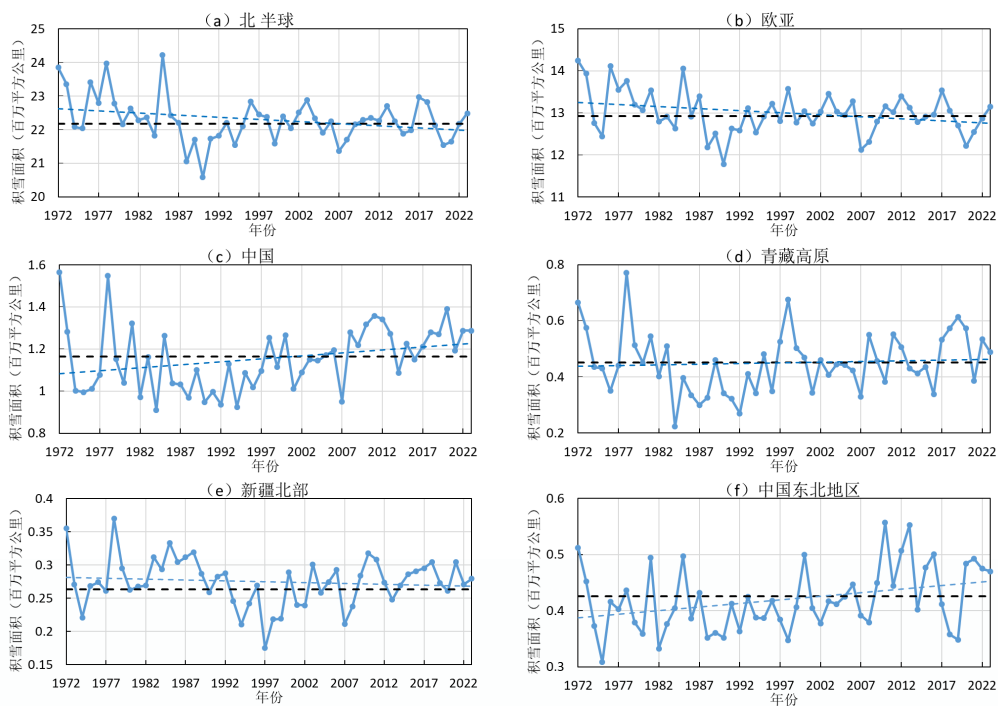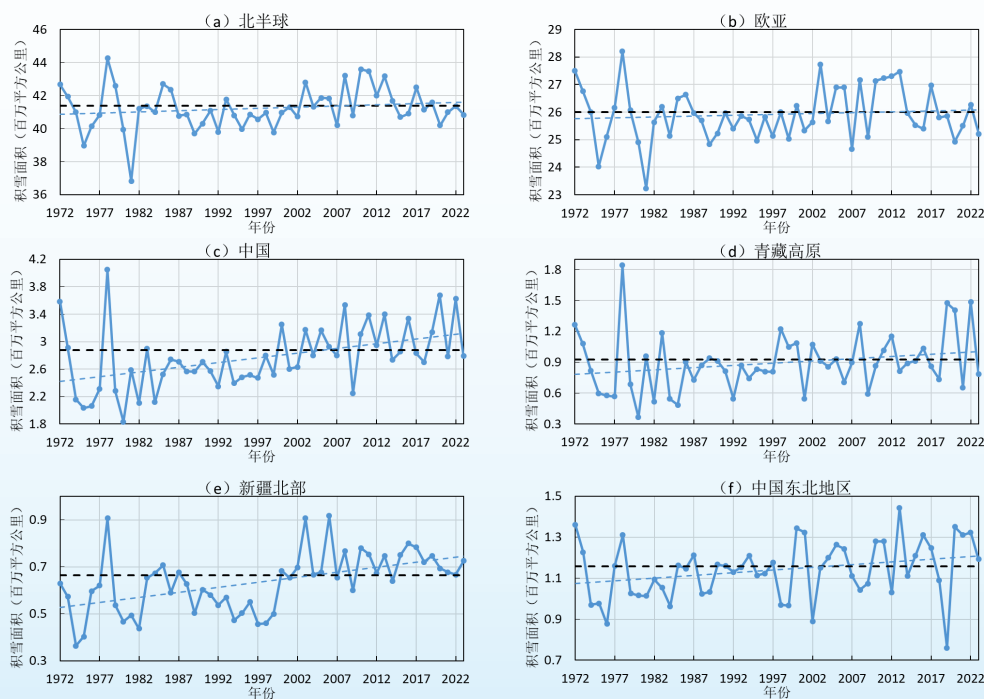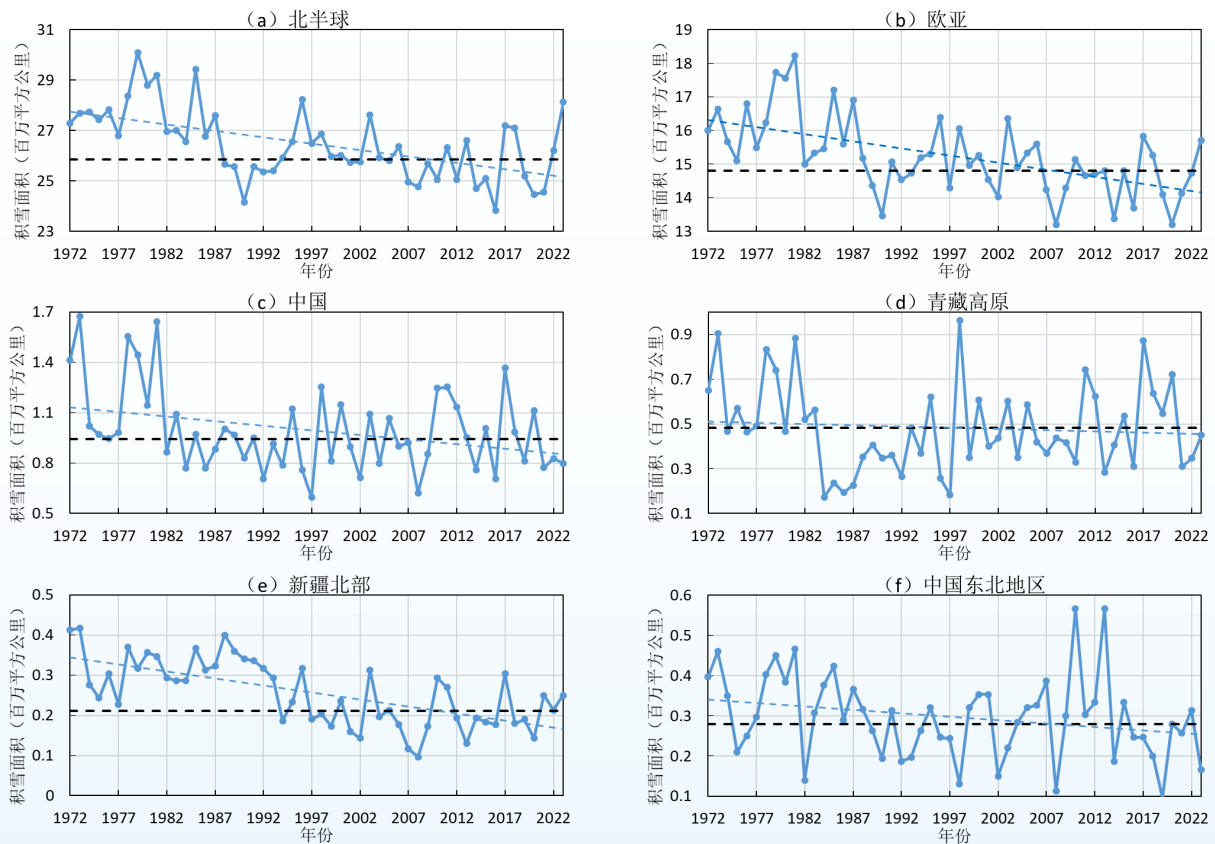

Figure 4.3 Long-term changes in mean spring snow cover area for (a) Northern Hemisphere, (b) Eurasia, (c) China, (d) Tibetan Plateau, (e) northern Xinjiang, (f) Northeast China. The black solid line represents the multi-year average, and the blue dashed line represents the linear trend over the entire period (in $10^6 km^2$)

During the autumn of 2023, the snow cover area in the Northern Hemisphere and Eurasia was close to the long-term averages for the same season but was smaller than that in the autumn of 2022. In China, the snow cover was 41.53% above the long-term average and also larger than in the autumn of 2022, making it the third highest on record. The snow cover in the Tibetan Plateau and Northeast China was significantly above their respective long-term averages, ranking as the tenth and third largest historically for this season, respectively. Conversely, the snow cover in northern Xinjiang was 13.44% below the long-term average and also smaller than in the autumn of 2022 (Table 4.1).

Table 4.1 Snow cover area anomaly percentage by season and region in 2023 (in %)

Season	Northern Hemisphere	Eurasia	China	Tibetan Plateau	Northern Xinjiang	Northeast China
Winter 2022/2023	-1.33	-3.18	-2.81	-14.91	9.35	3.01
Spring 2023	8.80	6.10	-15.06	-6.83	18.42	-40.38
Summer 2023	-4.04	12.18	57.60	65.52	-25.00	No snow in summer
Autumn 2023	-0.35	2.15	41.53	46.11	-13.44	67.37

*Due to the absence of snow in September, the autumn snow cover in Northeast China was averaged over October and November

3. Monthly Snow Cover Area

When examining the monthly changes in 2023 (Figure 4.4), it was found that the snow cover area in the Northern Hemisphere during April, May, and June was larger than the long-term averages. May, in particular, showed an increase of $6.84 \times 10^6 km^2$ (43.99% above the long-term average). The other months either recorded decreases or remained at levels close to the long-term averages. Similarly, Eurasia's snow cover area in May and June was significantly larger than the long-term averages for those two months. In May, there was a remarkable increase of $4.74 \times 10^6 km^2$ (61.08% above the long-term average), while the other months saw decreases or were close to the long-term averages. In China, the snow cover area showed a significant increase in June and from October to December, with increases of 113.20%, 42.15%, 45.48%, and 27.36%, respectively, while the remaining months were close to or below the long-term averages. The snow cover area changes in the Tibetan Plateau and Northeast China largely mirrored those in China, but the reductions in the Northeast during the spring were more pronounced, with April and May seeing decreases of 32.73% and 78.52%, respectively. In northern Xinjiang, the snow cover area was larger from January to June and in December. However, in the other months, it was either smaller or close to the long-term averages. The significant expansion of China's snow cover area in the autumn of 2023 was primarily driven by the substantial increases in the Tibetan Plateau and Northeast China.
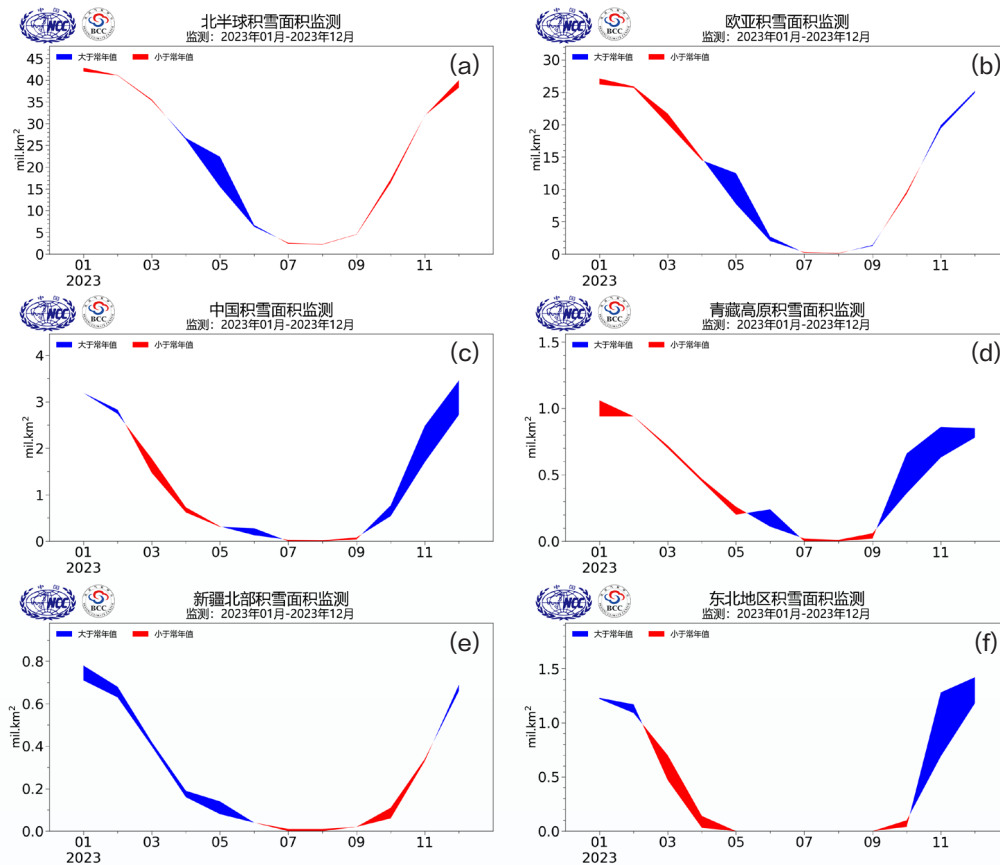
Figure 4.4 Monthly snow cover area index (in 10^6km^2) for (a) Northern Hemisphere, (b) Eurasia, (c) China, (d) Tibetan Plateau, (e) northern Xinjiang, (f) Northeast China

4.1.2 Snow-cover Days in the Northern Hemisphere

1. Annual Snow-cover Days

According to the monitoring data in 2023 (Figure 4.5), the majority of areas in the mid to high latitudes of the Northern Hemisphere experienced more than 90 snow-cover days. Compared to the long-term averages for the same period, significant reductions in snow-cover days were observed in most parts of Europe, most parts of Central Asia, the northern part of West Asia, the northern part of North Asia, the southern Tibetan Plateau and areas east of it, northern Canada, and the central United States, with southern Europe, the northern part of West Asia, and northern Canada experiencing reductions of more than 20 days. Conversely, parts of northwestern Europe, eastern Russia, eastern Mongolia, Northeast China, most of the Tibetan Plateau, and central and western North America saw an increase in snow-cover days. Specifically, the central Tibetan Plateau, Northeast China, and western regions of North America experienced increases of more than 25 days.
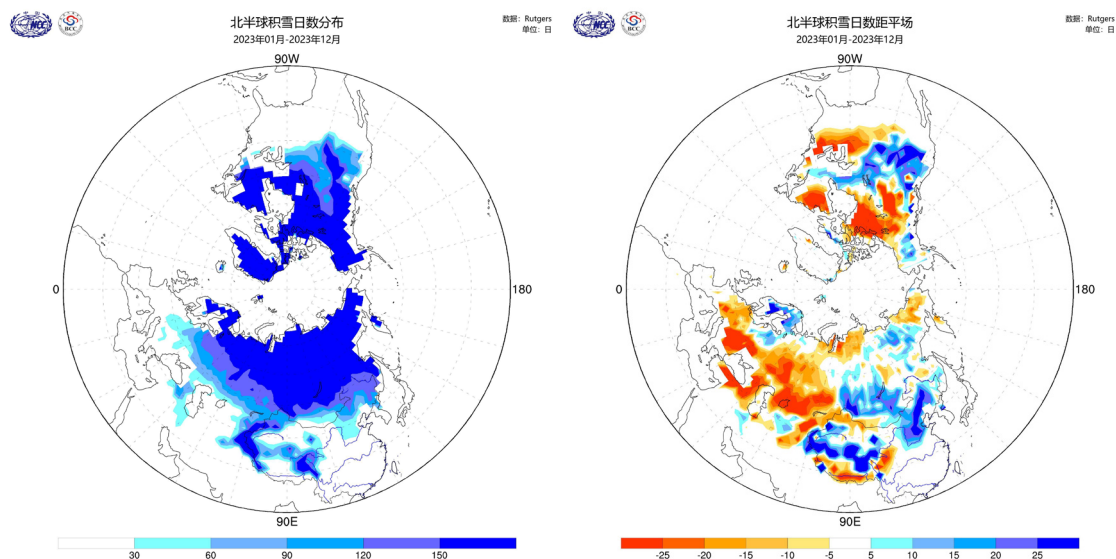
Figure 4.5 Northern Hemisphere snow-cover days (left) and anomaly (right) distribution in 2023 (in days)

2. Seasonal Snow-cover Days

Monitoring of seasonal snow-cover days in each season of the year (Figure 4.6) indicates that during the 2022/2023 winter, most regions in the mid to high latitudes of the Northern Hemisphere had more than 75 snow-cover days. Compared to the long-term averages for the same period, most areas north of 50°N were close to the averages. The central and western United States, eastern West Asia, southern Central Asia, western Tibetan Plateau, northern and western Xinjiang, and central and eastern East Asia experienced an increase in snow-cover days, with the central and western United States having more than 25 additional days. Conversely, the central and eastern parts of North America, southwestern Europe, northwestern West Asia, central and eastern Tibetan Plateau, southern Mongolia, and parts of northern China saw fewer snow-cover days, with southwestern Europe and parts of northeastern West Asia experiencing a decrease of more than 25 days.

In the spring of 2023, most regions north of 50°N in the Northern Hemisphere and the western and southeastern Tibetan Plateau had more than 30 snow-cover days, with northern Eurasia, Greenland, and northern North America having more than 75 snow days. Compared to the long-term averages, there was an excess of snow-cover days in the central and western North America, southern and eastern Central Siberia, and the southeastern and western edges of the Tibetan Plateau, while northern North America, much of Europe, Northeast China, parts of northern Xinjiang, and the southern edges of the Tibetan Plateau had fewer snow-cover days.

In the autumn of 2023, most regions north of 50°N in the Northern Hemisphere and the eastern and western Tibetan Plateau had more than 30 snow-cover days, with Greenland experiencing more than 75 snow-cover days. Compared to the long-term averages, some regions experienced an increase in snow-cover days, including localized areas in western and central Canada, localized areas in northern Europe, most of the Tibetan Plateau, northern Central Siberia, and from eastern Mongolia to Northeast China. Conversely, other regions had fewer snow-cover days, such as northern and eastern North America, southeastern Europe, Central Asia, northern Xinjiang, and central West and Central Siberia.
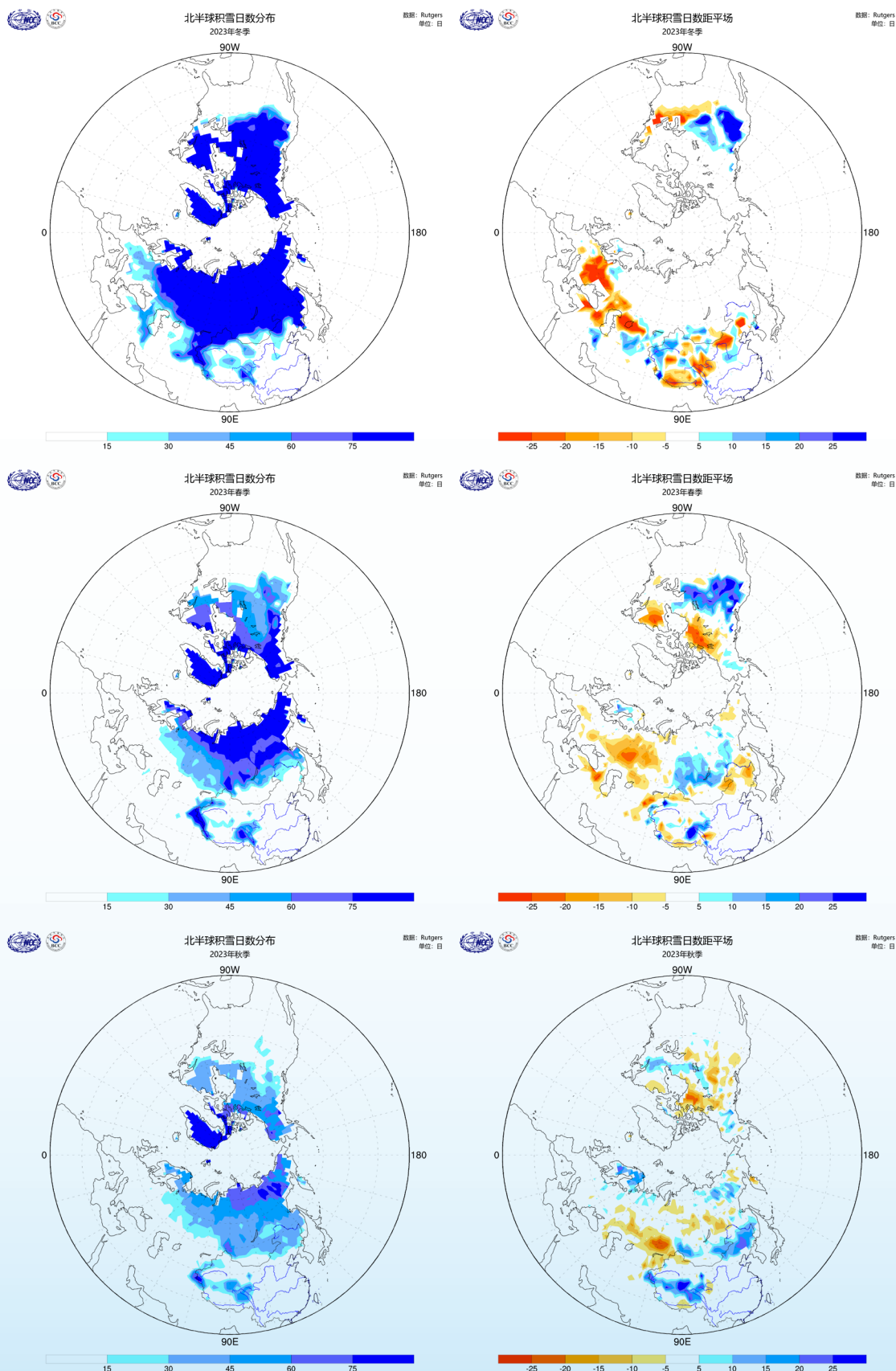
Figure 4.6 Northern Hemisphere snow-cover days (left) and anomaly (right) distribution in 2023 (in days), from top to bottom are winter, spring, and autumn

4.1.3 Snow Cover on the Tibetan Plateau Monitored by FengYun Satellites

1. Snow Cover Area in Winter

Since 2019, there has been an increase in the annual variability of the average winter snow cover area on the Tibetan Plateau, with significant fluctuations observed in both the eastern and western parts. In the winter of 2020, the eastern part of the Tibetan Plateau experienced its largest snow cover area between 2005 and 2023, while the western part and the entire Plateau saw the second largest area. During the winter of 2021, the western part of the Tibetan Plateau had its smallest snow cover area between 2005 and 2023, with the eastern part and the entire Plateau experiencing the second smallest area, both larger than the record low in 2006. In contrast, during the winter of 2022, the western part and the entire region of the Tibetan Plateau had their largest snow cover area between 2005 and 2023, with the eastern part having the third largest area during the same period. In the winter of 2023, the snow cover area on the Tibetan Plateau was below average (Figure 4.7).
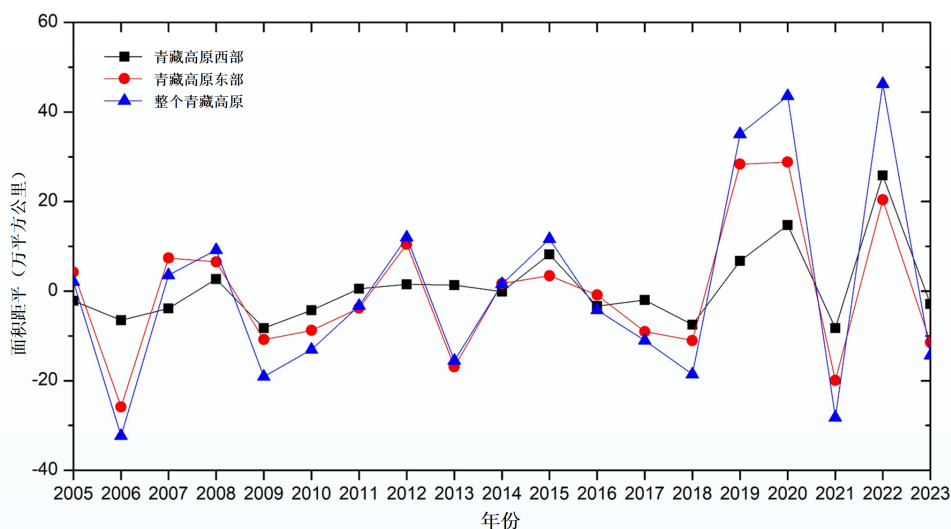
Figure 4.7 Anomalies of the average winter snow cover area on the Tibetan Plateau from 2005 to 2023, with the black dotted line representing the western part of the Plateau, the red dotted line representing the eastern part, and the blue dotted line representing the entire Plateau (in $10^4 km^2$)

2. Seasonal Snow Days

In 2023, the Tibetan Plateau showed a pattern of increased snow-cover days around the edges and slightly fewer in the interior during the winter, spring, and summer (Figure 4.8 left). Snow cover was present for most of the time during the winter and spring in the northwestern part of the Plateau, the major bend of the Yarlung Tsangpo River, and the Himalayas, but reduced significantly in the summer, with no snow cover in the southern interior and northeastern part of the Plateau. During the autumn, snow cover increased in the western, north-central, and southeastern parts of the Plateau, as well as in the Qilian Mountains. However, the Qaidam Basin and the southwestern interior of the Plateau had no snow cover. Looking at the anomalies in snow-cover days on the Tibetan Plateau (Figure 4.8 right), the western part had 15-30 more days in the winter, with localized areas around the great bend of the Yarlung Tsangpo River and the Qilian Mountains experiencing 30-60 more days; most other areas had 15-45 fewer days. In the spring, apart from the eastern part of the Hengduan Mountains and the Kunlun Mountain area in the Plateau's interior having 15-60 more days, the Qaidam Basin remained largely unchanged, with other areas having 15-30 fewer days. During the summer, the Himalayas, northwestern and central northern parts of the Plateau, and the Linzhi area

experienced an increase of 15-30 days, while most other areas were consistent with the long-term averages. A few areas showed a decrease of 15-30 days in coverage. In the autumn, the interior and the northwestern parts of the Plateau saw an increase of approximately 30-60 snow-cover days. In contrast, the central western Himalayas and some mountainous areas in the southeastern part of the Plateau had a sporadic increase of about 15 days, while other areas generally decreased by 15 to 30 days.
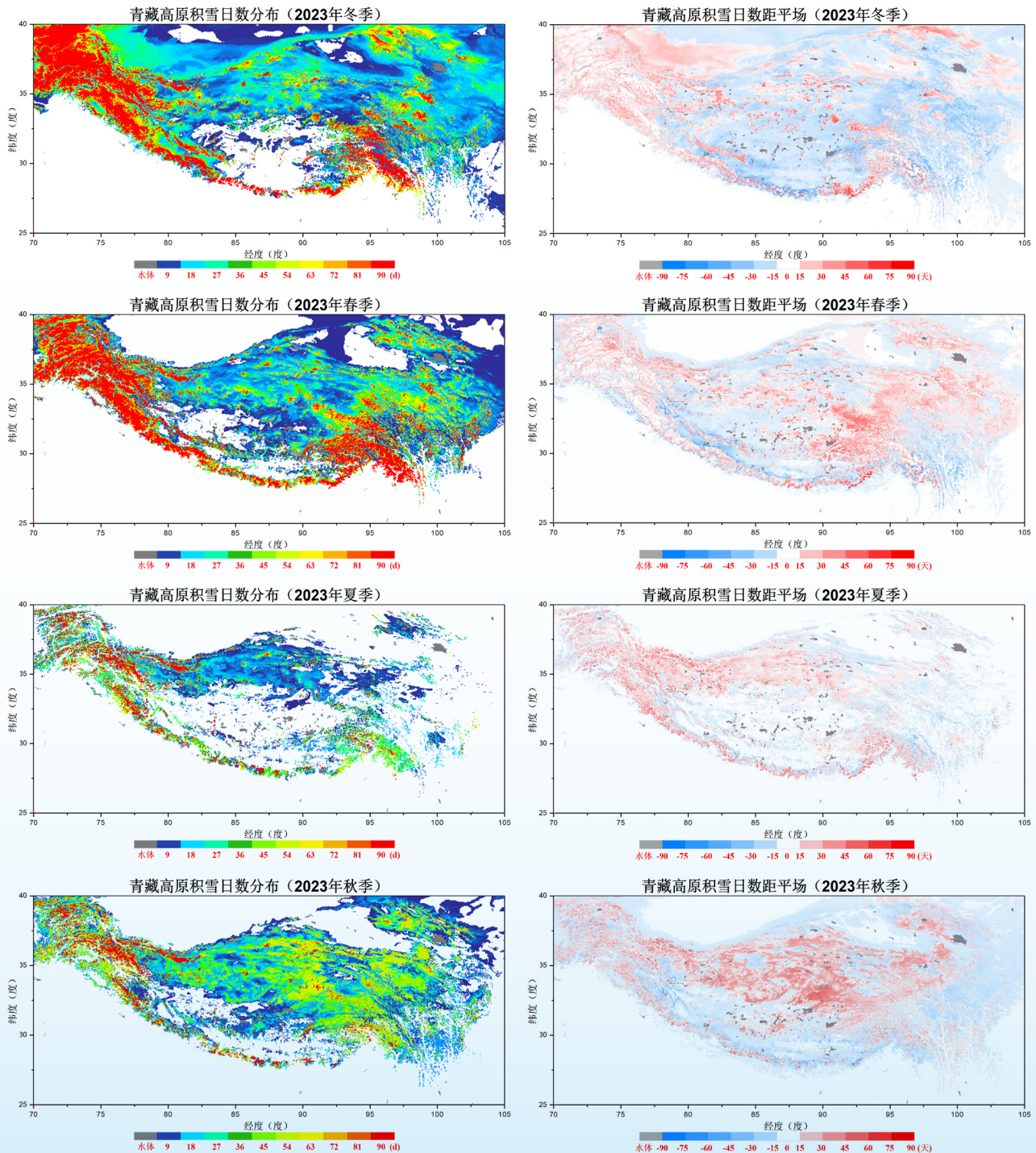
Figure 4.8 Tibetan Plateau's snow-cover days in 2023 by season (left) and their anomalies (right), compared to the averages from 2005-2019, from top to bottom are winter, spring, summer, and autumn (in days)

4.2 Sea Ice Monitoring

4.2.1 Arctic Sea Ice Extent and Density

The monthly monitoring of Arctic sea ice extent in 2023 shows that, in each month, the extent was consistently smaller than that of the same period over the years (averaged from 1991 to 2020, the same below). In 2023, the maximum extent was observed in March, while the minimum was observed in September (Figure 4.9).
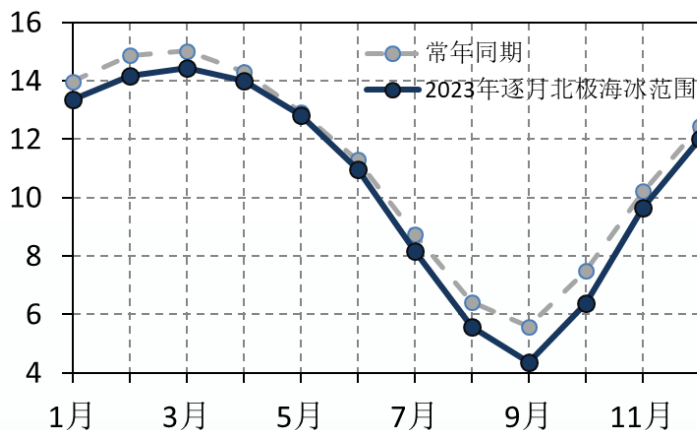
Figure 4.9 Monthly series of Arctic sea ice extent in 2023 (in $10^6 km^2$)

Since satellite observations became available in 1979, the overall extent of Arctic sea ice has shown a significant decreasing trend. In March 2023, the extent was $14.44 \times 10^6 km^2$, which was 3.9% smaller than that of the same period over the years ($15.03 \times 10^6 km^2$) and $0.15 \times 10^6 km^2$ smaller than that of the same period in 2022 (Fig 4.10 left). In September, the extent series of Arctic sea ice also showed a significant downward trend. In 2007, the Arctic sea ice extent experienced a cliff-like decline and has continued to shrink since then. As of September 2023, the extent was $4.37 \times 10^6 km^2$, which was 21.7% smaller than that of the same period over the years ($5.58 \times 10^6 km^2$) and $0.5 \times 10^6 km^2$ smaller than that of the same period in 2022 (Figure 4.10 right).
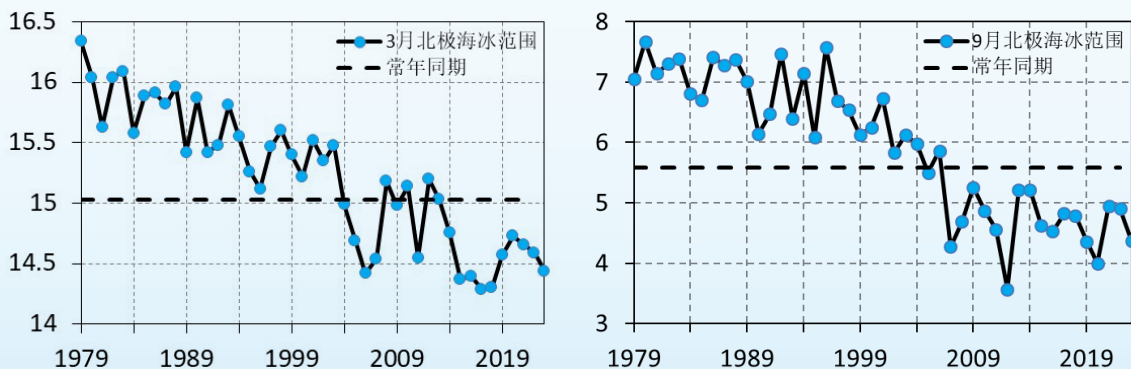
Figure 4.10　Time series of the Arctic sea ice extent in March (left) and September (right) (in $10^6 km^2$)

Figure 4.11 displays the sea ice concentration and its anomalies in the Northern Hemisphere for each season in 2023. During the winter in the Northern Hemisphere, the sea ice concentration exceeded 80% in the Arctic and surrounding areas such as the Baffin Bay, Greenland Sea, Kara Sea, Laptev Sea, New Siberian Sea, Chukchi Sea, Bering Strait, eastern Bering Sea, and Hudson Bay. In contrast, the sea ice concentration in the western and northern Okhotsk Sea, northern Bering Sea, and Davis Strait ranged from 10 to 80%. Regarding the concentration anomalies, they were 10 to 30% higher in the northwestern part of the Okhotsk Sea, the southern part of the Bering Sea Strait, and the western side of the Greenland Sea. Conversely, the anomalies were 10-30% lower in the northern part of the Barents Sea and the southern part of the Kara Sea.

In the spring, the distribution of sea ice concentration in the Northern Hemisphere was generally similar to that in the winter, but the sea ice extended further south. Sea ice concentration in most parts of the Okhotsk Sea and the southern end of the Davis Sea ranged from 10% to 40%. Regarding the concentration anomalies, they were higher by 10 to 40% in most of the Okhotsk Sea, the Bering Strait and the northern part of the Bering Sea, the Greenland Sea, the Davis Strait and its southern end. Conversely, the anomalies were 10 to 30% lower in the Barents Sea and parts of the central Bering Sea.

In the summer, areas in the Arctic with sea ice concentration exceeding 80% markedly diminished. The Arctic Ocean maintained its sea ice concentration above 80%, while the surrounding sea areas had reduced ice concentration ranging from 20-80%. On the anomaly field, apart from lower sea ice concentration in the southern Kara Sea and the northern Barents Sea, most other areas were close to or slightly above the normal levels of the same period over the years.

In the autumn, the extent of Arctic sea ice further reduced from its summer coverage, with areas such as most of the Hudson Bay, the majority of the Bering Strait, and the southern part of the Baffin Bay having sea ice concentration below 10%. However, areas with sea ice concentration above 80% expanded southward to the vicinity of the New Siberian Islands and the central part of the Canadian Basin. Additionally, the areas within the Greenland Sea with sea ice concentration above 80% were also extensive. In terms of anomalies, the Greenland Sea, areas near the New Siberian Islands, and the East Siberian Sea showed higher than average concentration by 10-30%, while areas like the Canadian Basin showed lower concentration by 10-30%.
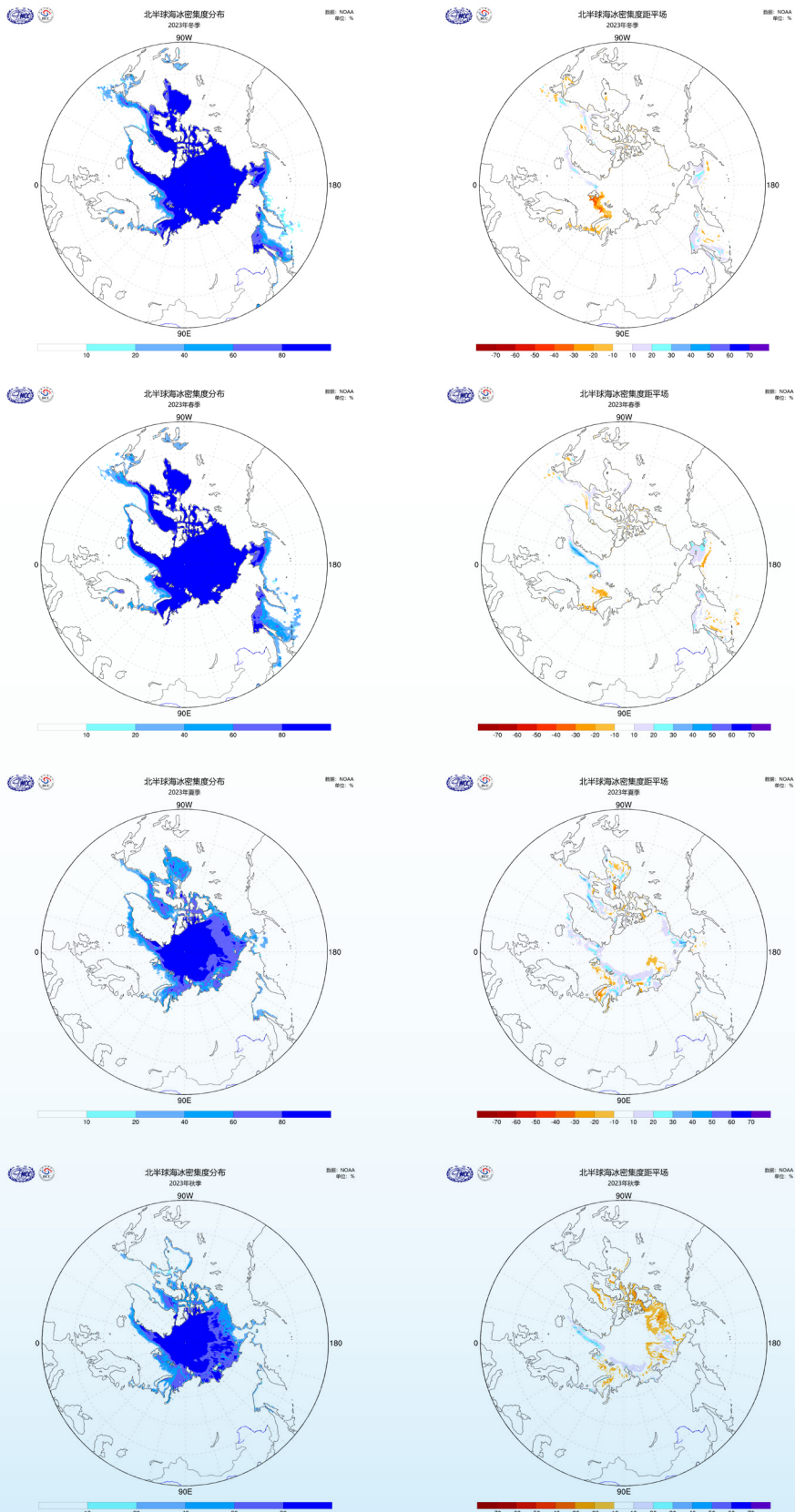
Figure 4.11 Distribution of seasonal sea ice concentration (left) and anomalies (right) in the Northern Hemisphere in 2023 (in %), from top to bottom are winter, spring, summer and autumn of the Northern Hemisphere

The monitoring of sea ice concentration and anomaly distribution in March and September 2023 (Figure 4.12) shows that in March, the Arctic Ocean basin and surrounding areas such as the Greenland Sea, Barents Sea, northern Bering Sea, Hudson Bay, Baffin Bay, Davis Strait, and the northern part of the Okhotsk Sea had sea ice concentration above 80%. In terms of anomalies, the northern and western parts of the Okhotsk Sea, northern Bering Sea, Greenland Sea, and Denmark Strait exhibited higher concentration by 10 to 40%, while the central Bering Sea, eastern and parts of southern and northern Barents Sea, scattered areas in the central Okhotsk Sea, and Davis Strait showed lower concentration by 10-30%.

In September, the extent of Arctic sea ice with concentration above 80% contracted northwards to regions including the northern Canadian Basin, Franz Josef Land, Greenland and north of the Queen Elizabeth Islands. Sea ice concentration in the Arctic Ocean from west of the Mendeleev Ridge (180°E) to 90°E was lower, ranging from 40 to 80%. Regarding anomalies, except for the areas near the Greenland Sea and Franz Josef Land where concentration was 10 to 40% above the long-term averages, most other regions experienced concentration 10 to 40% below the averages or near typical levels.
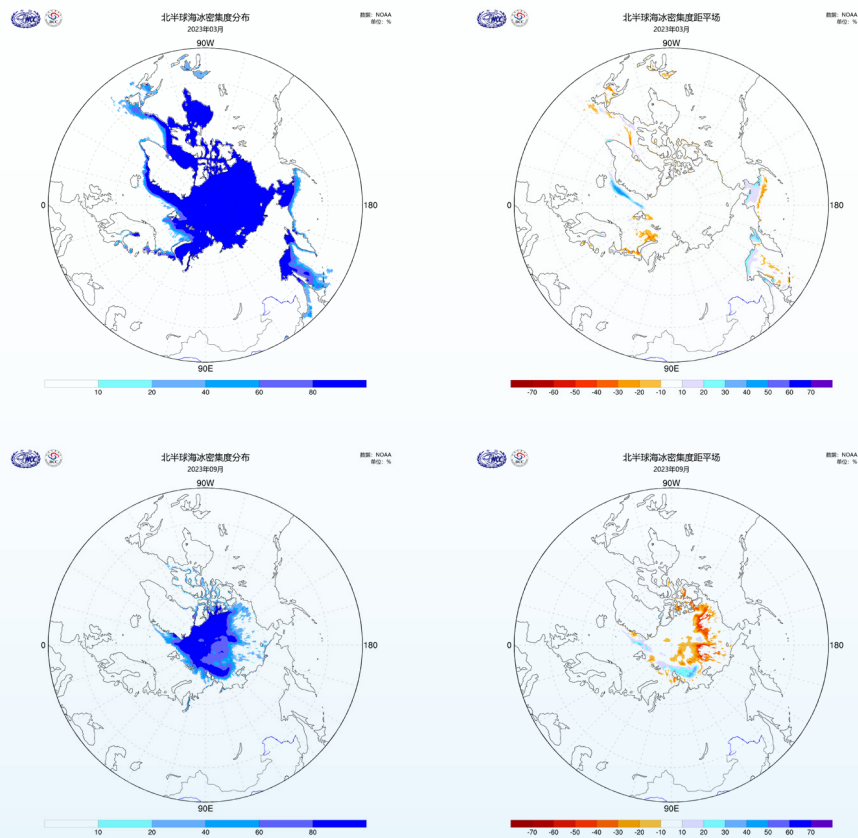
Figure 4.12 Sea ice concentration (left) and anomalies (right) in the Northern Hemisphere in March and September of 2023 (in %)

4.2.2 Arctic Sea Ice Extent and Concentration Monitored by FengYun Satellites

Figure 4.13 displays the long-term series of the Arctic sea ice extent based on the FY-3 MWRI sea ice concentration product. The daily maximum and minimum values of the Arctic sea ice extent in 2023 were observed on March 4th and September 18th, respectively, with the corresponding sea ice area of 14.67 $\times 10^6 km^2$ and $4.72\times 10^6 km^2$.
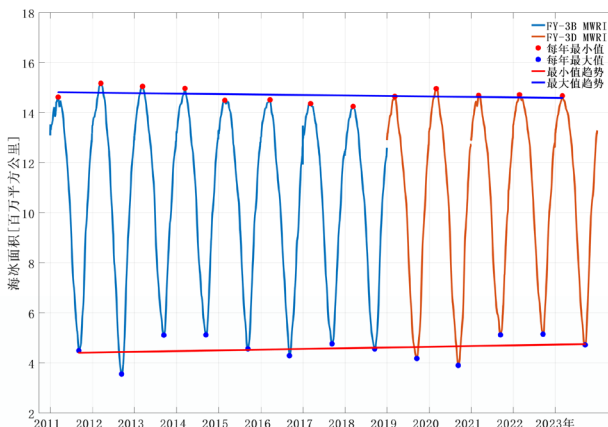
Figure 4.13 Long-term series of the Arctic sea ice extent (2012-2018: FY-3B/MWRI, 2019-2023: FY-3D/MWRI) (in $10^6 km^2$)

The time series graph comparing the Arctic sea ice extent for typical years (2012, 2020, and 2023) with the 2011-2022 average reveals distinct patterns: 2012 saw the largest area in winter and the smallest in summer since 2011, 2020 had the tenth lowest winter area and the second lowest in summer, while 2023 marked the seventh lowest winter area and the eighth lowest in summer (Figure 4.14).
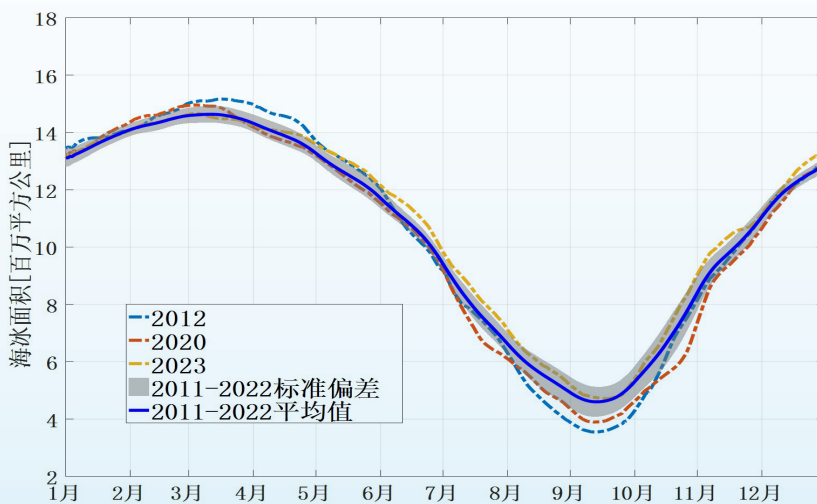
Figure 4.14 Time series graph of Arctic sea ice extent in typical years compared to the average from 2011-2022 (in $10^6 km^2$). The gray area represents the standard deviation of the sea ice extent from 2011 to 2022, while the blue line indicates the average sea ice extent from 2011 to 2022.

Figure 4.15 shows the percentage differences in the monthly average Arctic sea ice extent for March and September from 2011 to 2023 compared to the same months in the reference period (2011-2022). The graph indicates that in 2023, the March and September monthly averages were 0.42% lower and 2.78% higher, respectively, compared to the averages of the same months from 2011-2022. The linear fitting trend reveals that the percentage difference in the March monthly averages declined by 1.54% every ten years, while the September monthly averages increased by 5.69% every ten years.
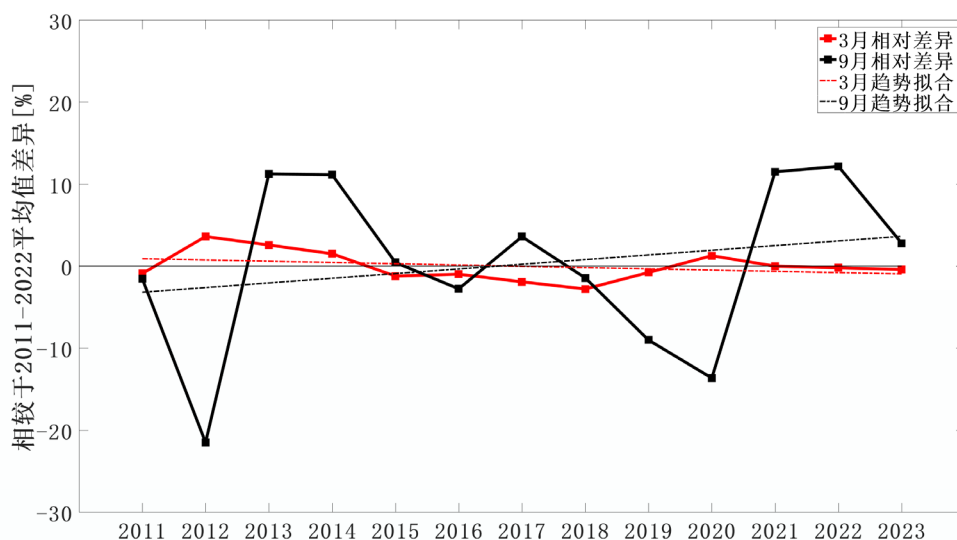
Figure 4.15 Time series graph of the percentage difference in average extent of Arctic sea ice in March and September (in %)

Figure 4.16 shows the spatial distribution of the monthly sea ice concentration anomalies in the Arctic for the year 2023. As can be seen from the figure, from January to March 2023, there were positive anomalies at the edge of the sea ice in the waters east of Greenland, the Bering Sea, and the Okhotsk Sea, while the edges of the sea ice in other areas generally experienced negative anomalies. During the sea ice melting season, the retreat of sea ice in April was very slow, the retreat rate in May and June was close to the average, and it accelerated in July and August. By mid-July, most of the sea ice along the coasts of Alaska and the East Siberian Sea had retreated, with the sea ice in Hudson Bay nearly completely melted. In August, the retreat of sea ice on the Pacific side was particularly noticeable, opening up large areas in the Beaufort Sea, Chukchi Sea, and East Siberian Sea regions.
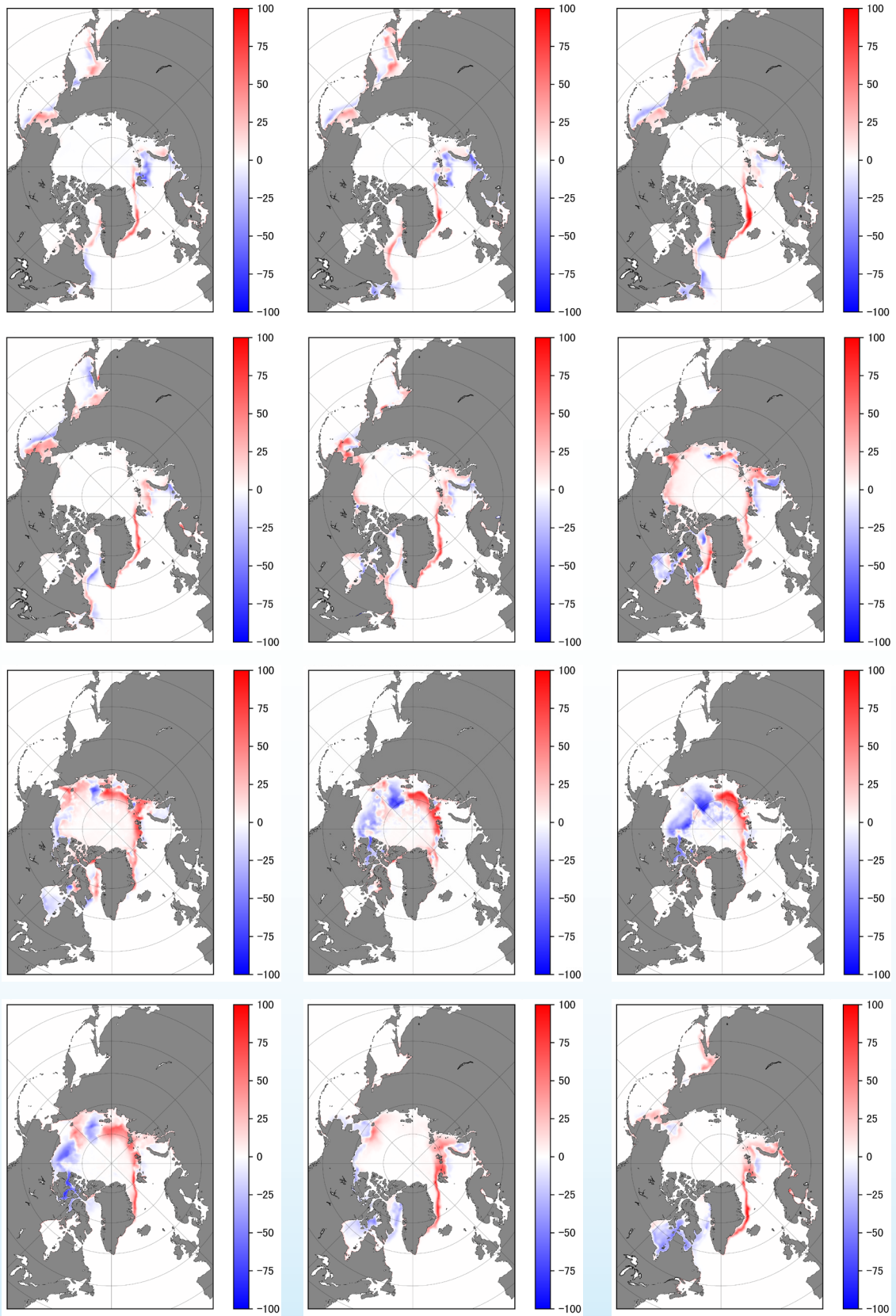
Figure 4.16 Spatial distribution map of monthly sea ice concentration anomalies in the Arctic for the year 2023 (from top to bottom are January to March, April to June, July to September and October to December) (in %)

4.2.3 Antarctic Sea Ice Extent and Concentration

Monthly monitoring of the Antarctic sea ice extent (Figure 4.17) shows that the monthly sea ice extent in 2023 consistently remained below the averages for the same period in previous years, with the deficit being quite significant. March, April, November, and December had the second lowest sea ice extent on record for the same period, while all other months had the lowest on record. The maximum value for the year occurred in September, and the minimum value was observed in February, consistent with the average annual pattern.
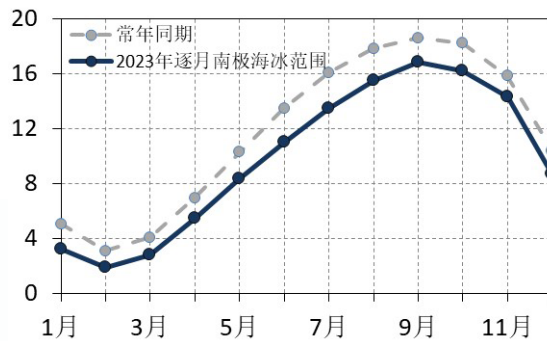
Figure 4.17 Monthly series of the Antarctic sea ice extent in 2023 (in 10^6km^2)

Figure 4.18 shows the historical series of Antarctic sea ice extent for February and September. The monitoring series of Antarctic sea ice extent in February indicates that from 1979 to 2015, there was a fluctuating upward trend in Antarctic sea ice extent. However, since 2016, the overall extent of Antarctic sea ice has generally been smaller than average. In February 2023, the Antarctic sea ice extent was $1.91 \times 10^6km^2$, which was 38.2% smaller than the average for the same period in previous years, marking the smallest extent for that period since satellite observations began. Before 2014, there was a significant linear increasing trend in the Antarctic sea ice extent for September, reaching its maximum historical extent in 2014. However, there was a substantial decrease in the Antarctic sea ice extent in the September of 2015, and since then, it has generally been smaller than average. In September 2023, the Antarctic sea ice extent was $16.80 \times 10^6km^2$, which was 9.7% smaller than the average for the same period in previous years, marking the smallest extent for that period since satellite observations began.
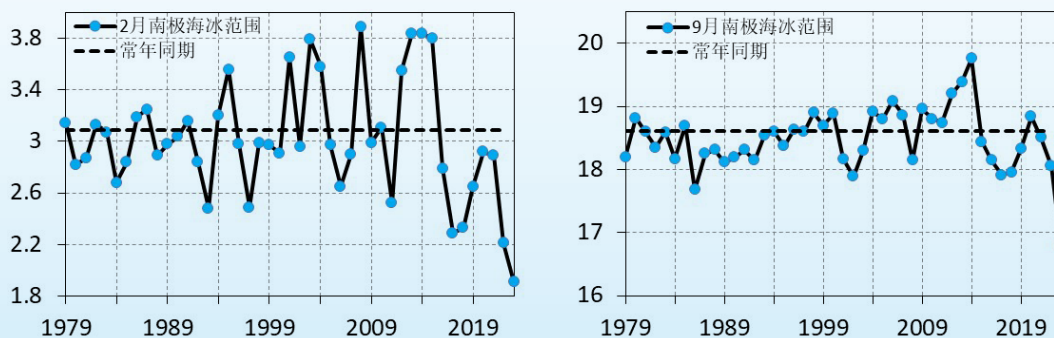
Figure 4.18 Time series of Antarctic sea ice extent in February (left) and September (right) (in 10^6km^2)

Figure 4.19 presents the distribution of sea ice concentration and anomalies throughout the seasons in the Southern Hemisphere. Monitoring shows that during the Southern Hemisphere summer (December 2022 - February 2023), except near the Weddell Sea reaching around 60°S, Antarctic sea ice was mainly distributed south of 65°S in the circumpolar region. In areas such as the Weddell Sea, the Wilkes Land coast, and the coast along Queen Maud Land, sea ice concentration exceeded 80%. In some parts of the continental edge around East Antarctica, concentration varied between 10 to 80%, while in regions near the Antarctic Circle in the Atlantic and South Pacific, they ranged from 10-60%. In terms of anomalies, areas like most of the Ross Sea, large parts of the Amundsen Sea, and some southern parts of the Weddell Sea showed higher-than-normal concentration by 10 to 30%. In contrast, regions near the Balleny Islands, the Edward VII Peninsula, the Bellingshausen Sea, and the northern part of the Weddell Sea showed lower concentration by 10 to 50%.

In the Southern Hemisphere autumn (March to May), the central and southern parts of the Ross Sea, as well as the Weddell Sea, had sea ice concentration over 80%. The Amundsen Sea and the King Haakon VII Sea also featured dense sea ice, exceeding 80% concentration. From the northern Ross Sea to the vicinity of the South Sandwich Islands and other areas around the continental edge of Antarctica, concentration ranged from 40-80%. On the anomaly map, apart from areas near the Queen Mary Coast, the Amundsen Sea, the Edward VII Peninsula, and the Ross Sea showing higher concentration, most other regions were 10 to 40% below average or near the long-term averages.

In the Southern Hemisphere winter (June to August), Antarctic sea ice significantly extended northward, with concentration exceeding 80% in most areas south of 65°S and in large parts of the Weddell Sea. Anomalies show that most regions around Antarctica in the South Atlantic, South Indian Ocean, and Southeast Pacific near polar areas, and east of the Antarctic Peninsula were 10 to 40% below normal, except for areas near the Queen Mary Coast and the eastern Bellingshausen Sea to the Amundsen Sea, which were 10 to 40% above normal.

During the Southern Hemisphere spring (September to November), Antarctic sea ice extent further extended northward to regions south of Oceania, north of the Amundsen Sea, and south of South Africa. In terms of anomalies, most areas in the South Atlantic, South Indian Ocean, and Southeast Pacific near polar regions were 10-40% below normal. However, areas near the Antarctic Peninsula, the Bellingshausen Sea, the Amundsen Sea, and from the coast of King George V to near Macquarie Island showed higher-than-normal concentration, 10 to 30% above normal.
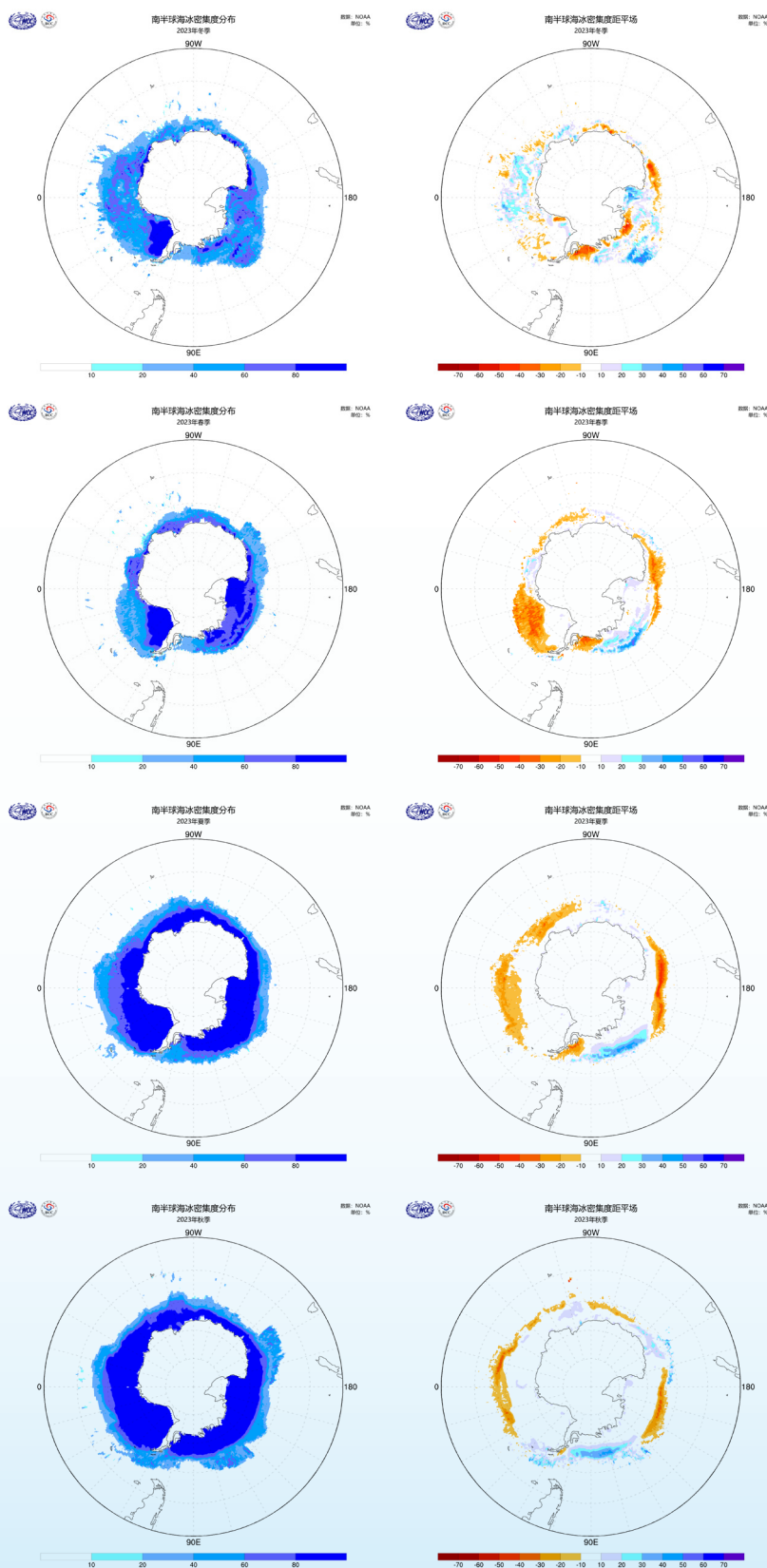
Figure 4.19 Seasonal sea ice concentration (left) and anomalies (right) in the Southern Hemisphere in 2023 (in %), from top to bottom are summer, autumn, winter and spring of the Southern Hemisphere

Monitoring of sea ice concentration and anomalies in the Southern Hemisphere in February and September 2023 (Figure 4.20) indicates that in February, Antarctic sea ice was primarily distributed in the Weddell Sea and around the continental margin of Antarctica, with concentration ranging from 10 to 80%. On the anomaly map, sea ice concentration was 10 to 30% higher than average in parts of southern Weddell Sea, northern Amundsen Sea, along the coast of Victoria Land, and Queen Maud Land. Conversely, concentration was 10 to 40% lower than average in the northern Weddell Sea, most of the Ross Sea, near Wilkes Land, near Queen Maud Land, and near the Coats Land.

In September, regions in the Southern Hemisphere with sea ice concentration exceeding 80% were mainly located around and south of 60°S. On the anomaly map, areas including the South Orkney Islands, from the Antarctic Peninsula to the Amundsen Sea, showed sea ice concentration 10 to 30% higher than average. In contrast, most peripheral areas around Antarctica had lower sea ice concentration, particularly in the South Pacific, South Atlantic, and west of the South Indian Ocean, where it was 10 to 40% below average.
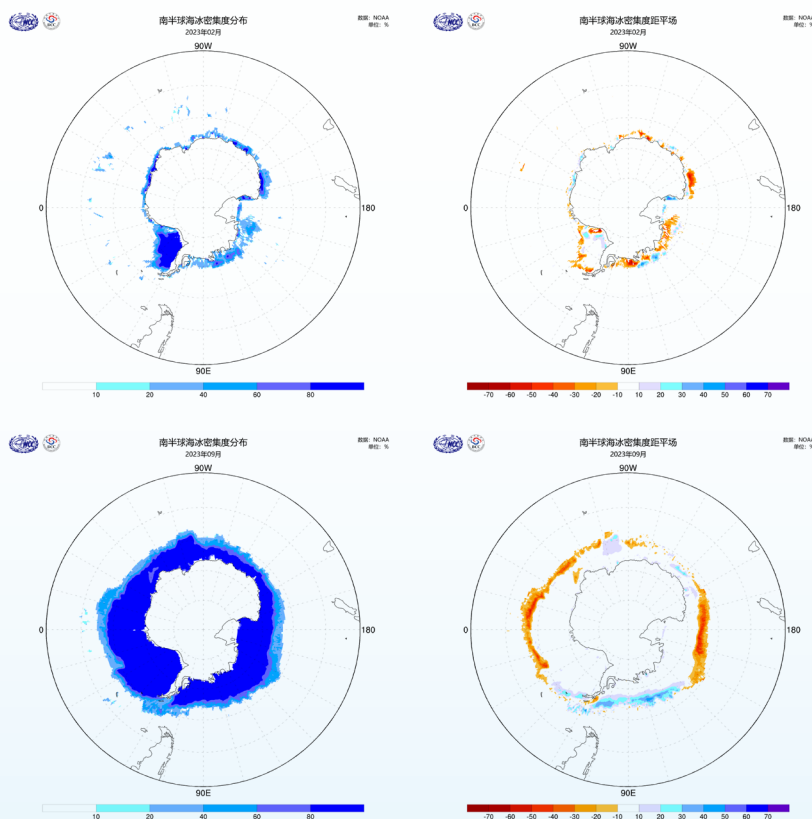
Figure 4.20　Sea ice concentration (left) and anomalies (right) in the Southern Hemisphere in February and September, 2023 (in %)

4.2.4 Antarctic Sea Ice Extent and Concentration Monitored by FengYun Satellites

Figure 4.21 presents the long-term time series of Antarctic sea ice extent based on the FY-3 MWRI sea ice concentration product. It is observed that in 2023, the daily minimum and maximum extent of Antarctic sea ice occurred on February 21st and September 11th, respectively, with corresponding sea ice area of $2.53 \times 10^{6} km^{2}$ and $17.37 \times 10^{6} km^{2}$. Both values were the lowest recorded since statistics began in 2011.
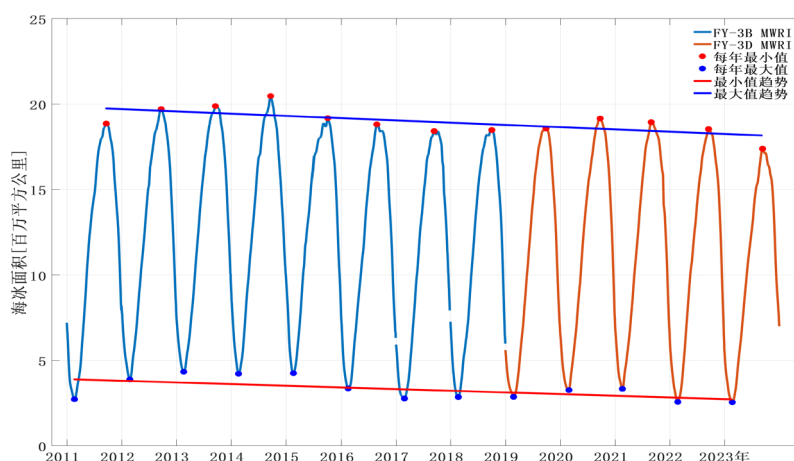
Figure 4.21 Long−term series of Antarctic sea ice extent (2012−2018: FY−3B/MWRI, 2019−2023: FY−3D/MWRI) (in 10^6km^2)

The time series chart of Antarctic sea ice extent for typical years (2014, 2017, 2018, 2022, 2023) compared to the average from 2011-2022 (Figure 4.22) shows: In 2014, the Antarctic sea ice extent was consistently above the multi-year average, marking it the year with the largest sea ice area in both winter and summer since 2012; 2017 recorded the third lowest summer extent and the second lowest winter extent; 2018 had the fifth lowest summer extent and the third lowest winter extent; 2022 saw the second lowest summer extent and the fourth lowest winter extent; 2023 had the lowest extent for both summer and winter on record.
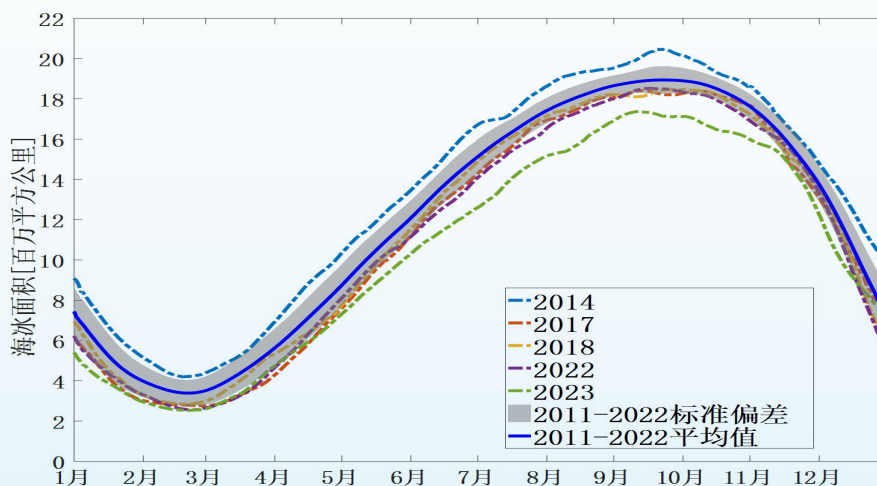
Figure 4.22 Time series chart of Antarctic sea ice extent for typical years compared to the average from 2011 to 2022 (in 10^6km^2). The gray area represents the standard deviation of the sea ice extent from 2011 to 2022, and the blue line indicates the average sea ice extent during 2011 and 2022.

Figure 4.23 shows the percentage difference in the February and September monthly averages of Antarctic sea ice extent from 2011 to 2023 compared to the average values of the same moths in the reference years (2011 to 2022). The chart reveals that in February and September 2023, the monthly averages were 25.24% and 8.78% smaller, respectively, than the averages for the same periods from 2011 to 2022. The linear trend suggests that the percentage difference in February's monthly averages decreased by 24.84% every ten years, while in September, it decreased by 5.57% every ten years.
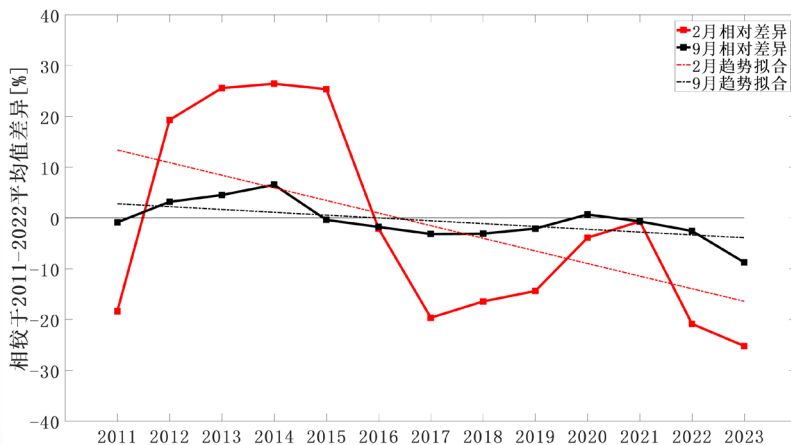
Figure. 4.23 Time series of the percentage difference in the February and September average sea ice extent in Antarctica (in %)

Figure 4.24 shows the spatial distribution of monthly sea ice concentration anomalies in the Antarctic for the year 2023. In February 2023, except for the sea ice in the Weddell Sea, which was close to the average level, the sea ice in other regions exhibited anomalously low concentration. Since April, with the exception of the Amundsen Sea, the sea ice extent in other Antarctic regions had been below the historical averages. The changes in various regions in 2023 showed a similar trend, leading to a very clear anomaly of smaller-than-average sea ice extent in the Antarctic.
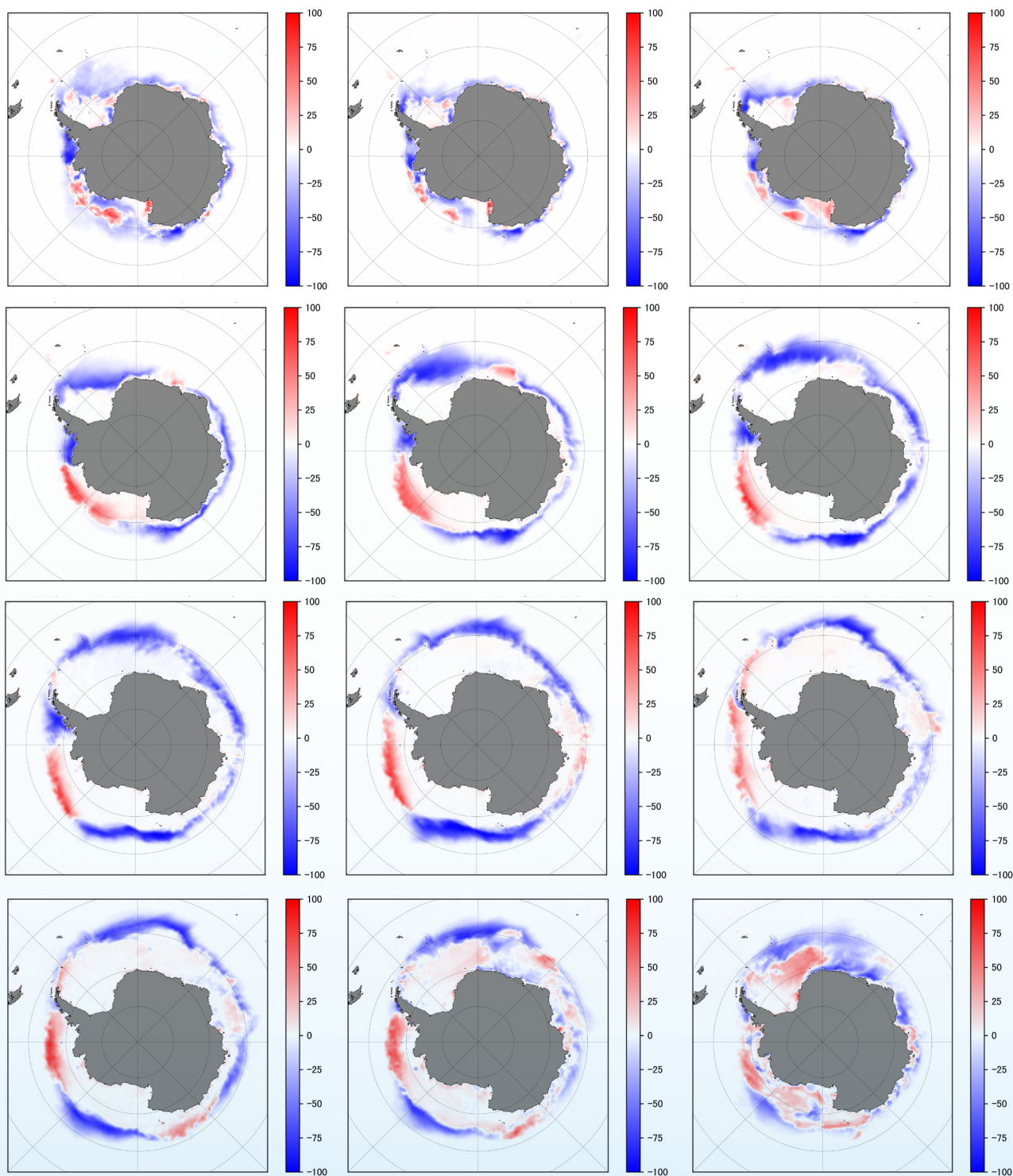
Figure 4.24 Spatial distribution of monthly average anomalies in Antarctic sea ice concentration for 2023 (from top to bottom are January to March, April to June, July to September and October to December) (in %)

Chapter V Major Global Meteorological Disasters and Significant Weather and Climate Events

In 2023, the global average temperature was 1.45 ℃ (±0.12 ℃) higher than pre-industrial levels, marking the hottest year on record. Global sea levels continued to rise, with the average global sea level reaching its highest point since satellite records began in 1993, reflecting ongoing ocean warming and the melting of glaciers and ice sheets. Arctic sea ice area remained significantly below the long-term average, while Antarctic sea ice area reached a historical low. Severe weather and climate events included rainstorms and floods in Greece, southern Bulgaria, parts of Iceland, and the North Island of New Zealand; severe drought in northwestern Africa, parts of the Iberian Peninsula, Central Asia and parts of Southwest Asia, as well as Central America and northern South America; record-breaking heatwaves in South Europe, North America, East Asia, and South Asia; cold waves and blizzards in Europe and North America; frequent severe convective weather worldwide; and frequent tropical cyclone activities globally.

5.1 Rainstorms and Floods

In Asia. During June, Pakistan experienced severe rainstorms that resulted in at least 30 deaths and 210 injuries. From mid to late June, continuous rainfall in Assam, India, flooded over 1300 villages, affecting nearly 500,000 people, destroying 14,000 hectares of crops, and causing 7 deaths. In early to mid-July, parts of northern India faced persistent heavy rain, leading to floods, landslides, and urban waterlogging, ultimately resulting in 91 fatalities. From July 29 to August 1, extreme precipitation occurred in North China and the Huang-Huai region, leading to a numbered flood event in the Haihe River basin. Multiple flood detention and storage areas in Beijing, Tianjin, Hebei, and other locations were activated. Local cumulative rainfall reached 650 mm to 1003 mm, and the intense precipitation triggered secondary disasters such as flash floods and urban waterlogging, resulting in severe damage.

In Europe. On May 18, an extreme rainstorm rain swept across the Emilia-Romagna region in northern Italy, leaving over 36,000 people homeless, at least 15 dead, and resulting in billions of euros in economic losses. On July 27, Moscow experienced record-breaking intense rainfall, with precipitation reaching 46 mm within a few hours, surpassing the previous highest record of 42.5 mm set in 1894. In early August, Storm *Hans* wreaked havoc across multiple countries in North Europe, causing flooding disasters in various places in Sweden, Norway, Denmark, and others. In September, Storm *Daniel* led to extreme precipitation in areas like Greece and southern Bulgaria. On September 5, the Thessaly region in Greece recorded a maximum rainfall of 759.6 mm, and between September 4 and 5, Kosti in Bulgaria experienced 329 mm of rainfall within 16 hours; together, Greece and Bulgaria reported a combined death toll of 19 people.

In America. In February, several cities along the northern coast of São Paulo state in Brazil suffered from rainstorms, resulting in 65 deaths. On April 12, the city of Fort Lauderdale in southern Florida, USA, experienced "once-in-a-millennium" heavy precipitation that led to flooding. On July 15, the northern part of Philadelphia in Bucks County, USA, was hit by successive flash floods and heavy precipitation, with 170 mm of rain falling within 45 minutes, leading to 5 deaths and 2 missing people.

In Oceania. During January and February, the North Island of New Zealand was subjected to several extreme precipitation and flooding events. On January 27-28, Auckland experienced torrential rain that caused local flooding, resulting in 4 deaths. On February 13-14, Hurricane *Gabrielle* led to daily rainfall exceeding 500 mm in some areas of the North Island, with Auckland recording the lowest atmospheric

pressure (971.5 hPa) ever recorded, and 11 deaths. The two rainstorms caused economic losses of 5.3 to 8.6 billion USD for New Zealand.

In Africa. In May, the Western and Northern Provinces of Rwanda were hit by heavy precipitation and floods, leading to 130 deaths and the collapse of over 5000 houses. Also in May, persistent torrential rain in South Kivu Province in the eastern part of the Democratic Republic of the Congo caused floods, resulting in at least 438 deaths and over 5500 missing. On September 10-11, Storm *Daniel* led to 414.1 mm of rain in 24 hours in Baida, Libya, with the intense rainfall causing the collapse of two dams. As of October 11, at least 4345 people had died and 8500 were missing in Libya. In October, heavy rainfall in the eastern part of Ghana brought severe flooding to the region, forcing nearly 26,000 people to evacuate. Also in October, torrential rain led to the displacement of over half a million people in Ethiopia, Somalia, and Kenya, and resulted in at least 130 deaths. In early November, Somalia was again hit by successive torrential rain, causing 96 deaths and affecting 2.3 million people.

5.2 High Temperatures, Heatwaves, Drought and Wildfires

In Asia. Mid-April saw regions like Maharashtra and Bihar in India hit by a severe heatwave, with daytime temperature exceeding 40 ℃, resulting in 13 heatstroke deaths in Mumbai. In April, Thailand faced ongoing high temperature, with many areas exceeding 40 ℃; Tak Province recorded a historic high of 45.4 ℃. Myanmar also set nearly 60-year high temperature records in April, causing over 10 heatstroke fatalities. In May, record-breaking heat affected several Southeast Asian countries: temperature reached 45 ℃ in northern Thailand, 43.5 ℃ in the city of Luang Prabang, Laos, 44.2 ℃ in northern Vietnam, 37 ℃ in Singapore, and 44 ℃ in parts of India. This extreme heat led to infrastructure damage, power shortage, and a surge in heatstroke cases. On April 11, a wildfire in the Gangneung area of Gangwon-do, South Korea, resulted in 17 deaths and damage to over 70 lodges and residences. In May, severe and ongoing drought in Yunnan, China, impacted the growth of spring crops and reduced electricity production. In June, China experienced its second highest number of high temperature days since 1961, with three heatwaves in North China and the Huang-Huai region leading to numerous cases of heatstroke and thermoplegia, putting pressure on the power sector. On June 11, wildfires in eastern Mongolia burned over 200,000 hectares, resulting in one death.

In Europe. Late July saw a severe and unusually prolonged heatwave sweep through southeastern Europe. On July 24, temperature in Lozolla and Yerzu on the island of Sardinia, Italy, reached 48.2 ℃, just 0.6 ℃ lower than the highest recorded temperature in Europe set in Sicily in 2021. On July 25, Tirana, Albania, recorded a local high of 43.0 ℃. Late August and early September saw the largest wildfire in EU history in northeastern Greece.

In America. January in Argentina set 75 high and low temperature records. On January 14, Florida Province in Uruguay matched the high of 44.0 ℃ set in January 1943. Mid to late June brought unusually high temperature to the southern United States (US) and Mexico, with most areas averaging over 4 ℃ higher than typical for the period. From April to October, wildfires in Canada destroyed an area over 18.5 million hectares, six times higher than the average of the last decade (2013-2022), and resulted in six fatalities. Wildfires in Hawaii caused at least 115 deaths and 850 missing people, marking the deadliest wildfire in US history. In South America, the subtropical regions experienced the worst drought of the year, resulting in wheat yields in Argentina more than 30% below the average of the last five years.

In Africa. Prolonged drought in northwestern Africa displaced 2.7 million people and severely affected crop yields.

5.3 Severe Cold and Heavy Snow

In mid-January, parts of Russia experienced extreme cold weather, with temperature in the coldest areas of Siberia reaching -73 ℃, setting a record for the lowest temperature in the Northern Hemisphere's history.

In January, Afghanistan had its coldest winter in nearly 15 years, resulting in 158 deaths due to the severe cold. In February, a severe winter storm swept across many parts of the USA, stretching from California in the Southwest to Maine in the Northeast. The storm brought gales, icing, extreme cold, blizzards, sleet, heavy precipitation, and other severe weather conditions, leading to school closure, flight delays, power outage, and road closure, severely affecting people's lives. On February 7, the Mount Washington Observatory in New Hampshire recorded a nighttime wind chill temperature of -78 ℃, setting the record for the lowest recorded in the USA. At the end of November, Ukraine experienced a winter storm that resulted in five deaths and one person missing.

5.4 Tropical Cyclones

In 2023, a total of 45 tropical cyclones were generated globally, a number below historical levels but with an intensity above average. Cyclone activity in the North Atlantic was near normal, while it was above normal in the East Pacific, North Indian Ocean, and South Indian Ocean. Activity in other regions, including the West Pacific which has been below normal for four consecutive years, was lower than normal.

In the Indian Ocean. Tropical Cyclone *Freddy*, which occurred in February and March, was one of the longest-lasting tropical cyclones on record. It formed off the west coast of Australia on February 6 and made its final landfall in Mozambique on March 11, then moved inland as a remnant low. Affected by *Freddy*, Mozambique and Malawi experienced exceptional precipitation (with Mozambique receiving up to 672 mm), leading to floods, landslides, and mudslides in Malawi, Mozambique, and Madagascar. This resulted in at least 679 deaths in Malawi, with over 650,000 people displaced within the country; 165 deaths in Mozambique; and casualties also reported in Madagascar and Zimbabwe. *Freddy* crossed the South Indian Ocean, disrupting major shipping routes and affecting East Asia-South America and East Asia-South Africa trade. In May, Tropical Cyclone *Mucha*, one of the strongest cyclones observed in the Bay of Bengal, reached a sustained wind speed of 115 knots; it displaced 1.7 million people across Sri Lanka, Myanmar, India, and Bangladesh, and caused 21 deaths in Myanmar.

In the North Pacific. In May, Typhoon *Mawar* passed north of Guam, USA, bringing gales and rainstorms, leading to widespread power outage. It also caused intense precipitation, floods, and landslides in Japan, resulting in 3 deaths, nearly a thousand homes inundated, and multiple areas suffering from power and water outage. In late July, Typhoon *Doksuri* made landfall in Cagayan Province in northern Philippines, causing 25 deaths, 52 injuries, and affecting 239 people. In late August, Typhoon *Khanun* caused disasters in various regions of Russia and South Korea, prompting tens of thousands to evacuate for safety. Also in August, Typhoon *Saola* affected 418,000 people in the Philippines, resulting in 2 deaths, 1 injury, and 1 missing person, with 25,000 people relocated to temporary shelters.

5.5 Severe Convective Weather

From March 24 to 31, the southern US states of Mississippi and Alabama experienced a tornado that resulted in 58 deaths. On April 7, eastern Canada was struck by a hailstorm, with freezing rain and strong winds causing trees to fall and power lines to be severed, leading to three weather-related deaths and power outage for hundreds of thousands of households. In April, the central US and Missouri were hit by tornadoes, causing at least 7 deaths and leaving tens of thousands of homes without power. On May 11, lightning strikes in Magura and Rajbari districts in Bangladesh led to 5 deaths and 1 injury. On June 17, a winter storm in Rio Grande do Sul, southern Brazil, brought heavy precipitation resulting in 15 deaths and 20 people missing, affecting as many as 41 cities. In June, various regions in China such as Liaoning and Jiangsu Provinces, along with several areas in the US, were struck by tornadoes and severe weather, resulting in at least 9 deaths, hundreds injured, and significant damage to dozens of houses.

强对流
4月美国中部及密苏里州遭遇龙卷风袭击造成至少7人死亡，数万家庭处于断电状态。

暴雨洪涝
7月29日至8月1日，受超强台风"杜苏芮"和"卡努"双台风影响，京津冀出现暴雨，引发山洪、城市内涝等次生灾害，受灾严重。

山火
4月11日，韩国东北部江原道江陵地区发生山火，山火造成17人死亡。

热带气旋
7月下旬，台风"杜苏芮"登陆菲律宾北部加延省，造成25人死亡，52人受伤，239人受灾。

高温
6月，中国华北黄淮地区出现3次高温过程，高温天气造成多起高温中暑、热射病等病例发生，同时给当地电力部门造成供电压力。

高温
7月下旬，高温热浪席卷了欧洲东南部，出现了严重且异常持续的高温。7月24日，意大利撒丁岛洛伊和耶罗气温达到48.2℃，仅比2021年西西里岛欧洲最高气温纪录低0.6℃。7月25日，阿尔巴尼亚地拉那气温达到43.0℃，创当地高温纪录。

山火
6月，美国夏威夷成夷野火造成至少115人死亡，850人失踪，是今年最致命的一场野火，也是美国野火史上死亡人数最多的一次野火。

干旱
8月，南美洲亚热带地区是今年干旱最为严重的区域之一，阿根廷北部和中部大部分地区8月份的气温比常年值低20%至50%各地区降雨量连续第四年显著低于正常年值。

干旱
5月，中国西南地区气象干旱阶段性发展。其中，云南发生严重冬春连旱，影响春播作物生长，造成发电量下降。

冬季风暴
11月底，乌克兰遭遇冬季风暴，造成5人死亡，1人失踪。

暴雨洪涝
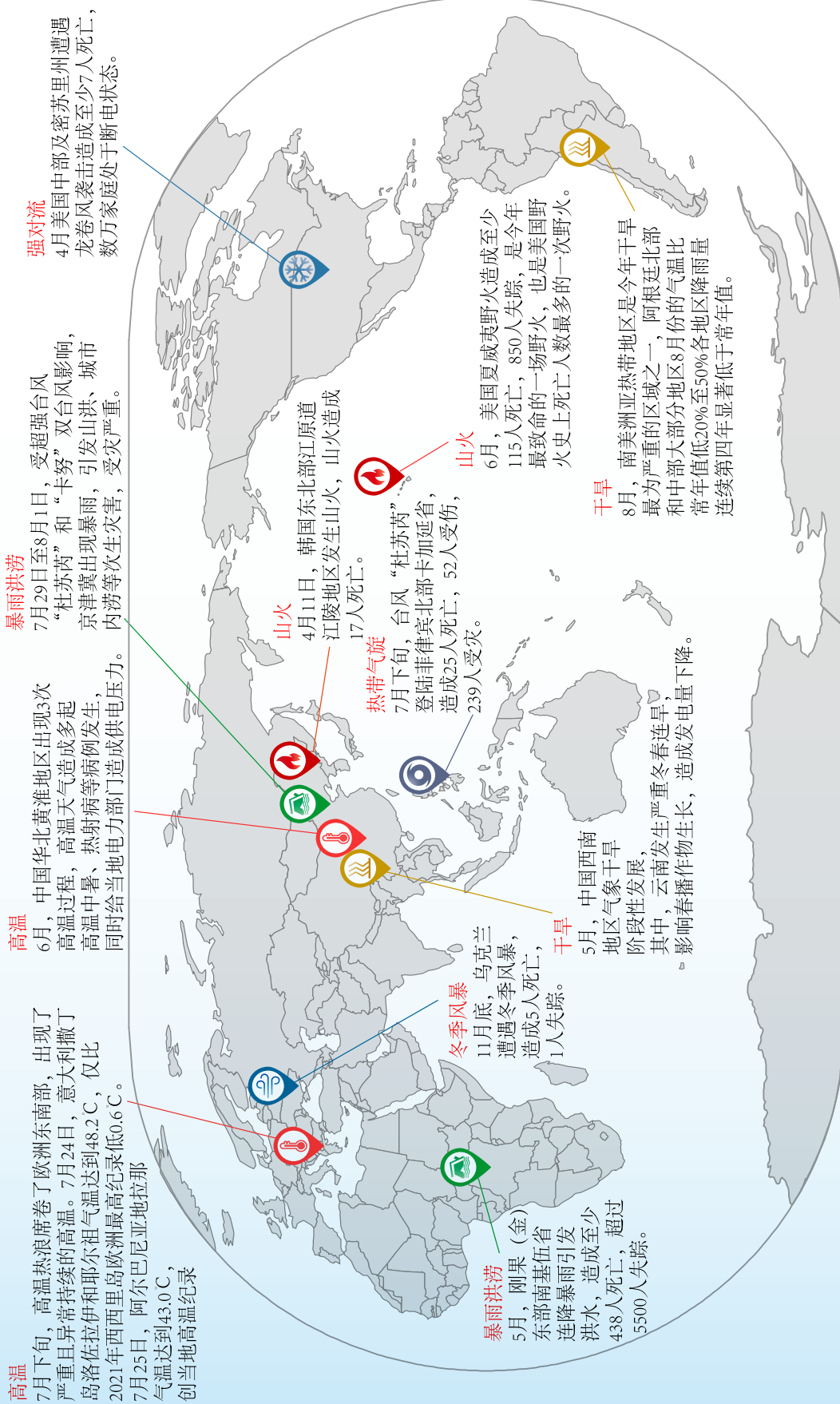5月，刚果（金）东部南基伍省连降暴雨引发洪水，造成至少438人死亡，超过5500人失踪。

Figure 5.1 Major disastrous weather and climate events around the world in 2023

Appendix I: Information Notes

1. For 2023, the annual average refers to the average for the entire year, from January to December 2023. The winter season is defined as December 2022 through February 2023, spring is from March to May 2023, summer is from June to August 2023, and autumn is from September to November 2023. The climatological state is based on the average from 1991 to 2020.

2. Global average temperature data is sourced from the "Global Monthly Gridded Dataset for Land Surface Temperature Reconstruction (V1.0) (CMA-GLST)," with a monthly temporal resolution, spanning 1850-2023, and a spatial resolution of $1° \times 1°$, provided by the National Meteorological Information Centre.

3. Global precipitation data is sourced from the "China First Generation Land Surface Reanalysis (CMA-RA/LAND)," with a monthly temporal resolution since 1979, and a spatial resolution of $0.25° \times 0.25°$, provided by the National Meteorological Information Centre.

4. Global surface climatic values are derived from the "Global Dataset of Climatic Values for Land Surface Temperature and Precipitation (1991-2020)," provided by the National Meteorological Information Centre.

5. Atmospheric circulation data is sourced from the "China First-Generation Atmospheric Reanalysis (CMA-RA)", with a monthly temporal resolution since 1979, and a spatial resolution of $1° \times 1°$, provided by the National Meteorological Information Centre.

6. Sea surface temperature data is sourced from the "Global Sea Surface Temperature Gridded Reconstruction Dataset (V1.0)," with a monthly temporal resolution spanning 1850-2023, and a spatial resolution of $2° \times 2°$, and also from the "Global Sea Surface Temperature Real-time Fusion and Analysis Product (V1.0)," with a daily temporal resolution since 1981, and a spatial resolution of $0.25° \times 0.25°$, both provided by the National Meteorological Information Centre.

7. Snow cover extent data is sourced from Rutgers University's Global Snow Lab, available at https://climate.rutgers.edu/snowcover/.

8. Sea ice extent data (NSIDC v3 Sea Ice Index) is sourced from the National Snow and Ice Data Center at https://nsidc.org/, while sea ice concentration data is obtained from the NOAA Physical Sciences Laboratory at https://psl.noaa.gov/, with a monthly temporal resolution since December 1981, and a spatial resolution of $1° \times 1°$.

9. FengYun satellite sea surface temperature, snow cover, and sea ice products are sourced from the National Satellite Meteorological Centre at http://data.nsmc.org.cn.

Appendix II: Definitions of SST and Southern Oscillation Indices

1. 1. Niño 3.4 SST index: The average sea SST anomaly in the area (170° - 120°W, 5°S - 5°N). An El Niño/La Niña event is identified when the absolute value of the three-month running mean of the Niño 3.4 index (rounded to one decimal place, the same below) reaches or exceeds 0.5 ℃ and persists for at least five months (Niño 3.4 index ≥ 0.5 ℃ indicates an El Niño event; Niño3.4 index ≤ -0.5 ℃ indicates a La Niña event).

2. Eastern El Niño/La Niña Index (EP Index):

$$I_{EP} = I_{NINO3} - \alpha \times I_{NINO4} \cdots\cdots\cdots\cdots\cdots (1)$$

Where：I_{EP}——Eastern El Niño/La Niña index is measured in degrees Celsius (℃);

I_{NINO3}——NINO3 Index is measured in degrees Celsius (℃);

I_{NINO4}——NINO4 Index is measured in degrees Celsius (℃);

α——When $I_{NINO3} \times I_{NINO4} > 0$, $\alpha = 0.4$; When $I_{NINO3} \times I_{NINO4} \leqslant 0$, $\alpha = 0$.

3. Central El Niño/La Niña index (CP El Niño/La Niña index):

$$I_{CP} = I_{NINO4} - \alpha \times I_{NINO3} \cdots\cdots\cdots\cdots\cdots （2）$$

Where：I_{CP}——Central El Niño/La Niña index is measured in degrees Celsius (℃).

4. Eastern/Central Pacific Events: An event is classified as an Eastern-type event if the absolute value of *IEP* reaches or exceeds 0.5 ℃ and persists for at least three months; it is classified as a Central-type event if the absolute value of *IEP* reaches or exceeds 0.5 ℃ and persists for at least three months. If an event includes conditions or transitions between the two types, the type associated with the peak value of the event is defined as the primary type, and the other as the secondary type. The overall classification of the event is based on the primary type.

5. Southern Oscillation Index (SOI): The normalized value of the SLP difference between Tahiti and Darwin stations. The calculation formula is as follows:

$$SOI = \frac{P_{diff} - P_{diffave}}{SD\left(P_{diff}\right)}$$

Where Pdiff is the monthly difference in SLP between Tahiti and Darwin stations (Tahiti minus Darwin), Pdiffave is the climatological average of this pressure difference per month (based on 1991-2020), and SD (Pdiff) is the standard deviation of this monthly pressure difference.

6. Pacific Decadal Oscillation (PDO) index: The SST anomaly within the region (110°E - 100°W) is projected onto the first mode of Empirical Orthogonal Function (EOF) of that area, after removing the global SST anomaly trend. The resulting projected index, after normalization, is defined as the PDO index. The reference period for EOF and index normalization is 1901-2010. Annual scale data is obtained by averaging the monthly indices.

7. Indian Ocean Basin-Wide (IOBW) mode index: The regional average SST anomaly in the tropical Indian Ocean (20°S - 20°N, 40° - 110°E).

8. Tropical Indian Ocean Dipole (TIOD) index: The difference in regional average SST anomalies between the tropical western Indian Ocean (10°S - 10°N, 50° - 70°E) and the tropical southeastern Indian

Ocean (10°S - 0°, 90° - 110°E).

　　9. South Indian Ocean Dipole (SIOD) index: The difference in regional average SST anomalies between the southwestern Indian Ocean (45° - 30°S, 45° - 75°E) and the southeastern Indian Ocean (25° - 15°S, 80° - 100°E).

　　10. North Atlantic Tri-pole (NAT) SST index: The projection of the SST anomaly field in the North Atlantic (0° - 60°N, 80°W - 0°) from January 1981 to December 2010 (after removing the linear trend) onto the first mode of EOF, with the projection index normalized based on the mean and standard deviation from 1981-2010, resulting in the normalized North Atlantic Tri-Pole SST index.

　　11. Tropical North Atlantic SST index: The regional average SST anomaly in the region (5° - 20°N, 60° - 30°W).

　　12. Equatorial Atlantic SST index: The regional average SST anomaly in the region (2.5°S - 2.5°N, 20°W - 0°).

　　13. North Atlantic Multi-decadal Oscillation (AMO) index: The regional average SST anomaly in the North Atlantic (0° - 60°N, 80°W - 0°) (removing the global anomaly's linear trend).

Appendix III: Definitions of Atmospheric Circulation Indices

1. Arctic Oscillation (AO) index: Normalized series of the first mode time coefficient from Empirical Orthogonal Function (EOF) decomposition of the 1000 hPa height anomaly field in the region (20° - 90°N, 0° - 360°E).

2. North Atlantic Oscillation (NAO) index: Normalized projection coefficient on the first mode from EOF decomposition of the normalized 500 hPa height field from January 1950 to December 2000 (20° - 90°N, 0° - 360°E). The projection method used is as follows: $I_{NAO} = \mathrm{avg}\left(\dfrac{\mathrm{sum}(\mathrm{hgt}^*\mathrm{pat})}{\mathrm{sqrt}(\mathrm{avg}(pat^2))}\right)$, where hgt is the normalized anomaly, and pat is the modal data.

3. Antarctic Oscillation (AAO) Index: (1) Calculate the area of each grid point: $\mathrm{area} = \mathrm{R}^*(1 - \sin(\varphi))^*\lambda$, where λ is the grid interval, φ is the latitude, R is the Earth's radius (6378 km); (2) Calculate the anomaly area of each grid point: $\mathrm{hgt} = hgt_{anom} * area$, where hgt_{anom} is the height field anomaly; (3) Project the anomaly area onto the AAO mode: $I_{AAO} = \mathrm{sum}(\mathrm{hgt}^*\mathrm{pat}) / \mathrm{sum}(area^2) / \mathrm{sqrt}(\mathrm{avg}(pat^2))$, where pat is the modal data.

4. Eurasian Blocking High index: Calculated based on 500 hPa geopotential height grid data: $\mathrm{GHGS} = \dfrac{Z(\varphi_0) - Z(\varphi_s)}{\varphi_0 - \varphi_s}$ and $\mathrm{GHGN} = \dfrac{Z(\varphi_n) - Z(\varphi_s)}{\varphi_n - \varphi_s}$, where Z is the 500 hPa geopotential height, φ is the latitude, $\varphi_n = 80 + \delta$, $\varphi_0 = 60 + \delta$, $\varphi_s = 40 + \delta$, $\delta = -5, 0, 5$. A longitude is considered to have a blocking high if for at least on δ value, the condition $\mathrm{GHGS} > 0$ and $\mathrm{GHGS} < -10$ are met simultaneously.

5. Pacific-North American (PNA) Pattern index: Normalized projection coefficient on the second mode of the EOF decomposition of the 500 hPa height field over the region 20° - 90°N, from January 1950 to December 2000.

6. East Asia-Pacific (EAP) teleconnection pattern index $I_{EAP} = \mathrm{NOR}\left(-0.25 Z'_s (20°N, 125°E) + 0.5 Z'_s (40°N, 125°E) - 0.25 Z'_s (60°N, 125°E)\right)$, wher $Z' = Z - \overline{Z}$ (Z is the 500 hPa geopotential height at a certain point during the summer of a given year $\overline{Z}$ is the climatological mean state) $Z'_s = Z' \sin 45° / \sin \varphi$, Φ is the latitude, an $\mathrm{NOR}(\mathrm{X})$ refers to the normalization process.

7. North American Monsoon index defined at the 700 hPa level (17.5° - 35°N, 100° - 120°W); West African Monsoon Index defined at the 850 hPa level (5° - 17.5°N, 20°W - 40°E); South Asian Monsoon Index defined at the 850 hPa level (5° - 22.5°N, 35° - 97.5°E).

8. South China Sea Summer Monsoon Intensity index: (1) Monitoring region for the South China Sea monsoon: 10° - 20°N, 110° - 120°E; (2) The monsoon onset time is marked by the average zonal wind shifting from easterly to westerly and pseudo-equivalent potential temperature stably exceeding 340K; the monsoon end time is marked by zonal wind shifting back from westerly to easterly and pseudo-equivalent potential temperature stably below 340K; (3) The normalized anomaly of the cumulative intensity of zonal wind during the monsoon period is the South China Sea Summer Monsoon Intensity Index (Zhu Yanfeng, 2005).

9. East Asian Summer Monsoon Intensity index: Difference between the average 850 hPa zonal wind in the regions (5° - 15°N, 90° - 130°E) and (22.5° - 32.5°N, 110° - 140°E), normalized.

10. Area-weighted average difference of 500 hPa zonal wind between the regions (25° - 35°N，80° - 120°E) and (50° - 60°N，80° - 120°E), normalized.

11. Siberian High index: Regional average sea level pressure over the region (80° - 120°E, 40° - 60°N).

Appendix IV: Top Ten International Weather and Climate Events of 2023

1. Rare Mediterranean Hurricane Daniel triggers a massive disaster in Libya.
2. Persistent drought in Brazil, with Amazon River tributaries reaching historic low levels.
3. The era of "Global Boiling" arrives as Earth's average temperature reaches a new high.
4. Northwestern Australia experiences "once-in-a-century" floods.
5. A super cold wave hits the US, with nighttime wind chill temperatures as low as -78 ℃.
6. Summer-like winter in South America, with temperatures exceeding 37 ℃.
7. Southern Hemisphere Tropical Cyclone Freddy sets a record for the longest lifespan.
8. Wildfires on Hawaii's Maui Island in the US cause severe casualties.
9. El Niño stirs global climate, amplifying extreme weather events.
10. Frequent solar storms produce strong auroras across the Northern Hemisphere.

For more information, please check the National Climate Centre's WeChat public account.